Chapter 2

Physics

2.1 Physics Overview

2.1.1 The Standard Model and its Missing Links

The goal of elementary particle physics is to identify the fundamental constituents of the physical world and the interactions among them, and find their simple description. Over these decades, it has become more and more certain that all but one of the four known interactions—electromagnetic, weak, and strong—can be described by the "Standard Model" [1], which is based on quantum field theory and gauge principle.

At the center of the Standard Model lies the concept of the spontaneous symmetry breaking [2], which generates the masses of the W- and Z-bosons. The discovery of these intermediate vector bosons at the predicted masses [3] is a great triumph of this concept. The masses of fermions are also generated by the spontaneous symmetry breaking, due to the Yukawa couplings of fermions to the Higgs boson.

The gauge principle has been tested with a very high precision. In particular, the quark-lepton universality, which motivated the introduction of gauge principle to the weak interaction physics [4], has been verified to 0.1% [5]

$$|V_{ud}|^2 + |V_{us}|^2 + |V_{ub}|^2 = 0.9991 \pm 0.0016, \tag{2.1}$$

where V_{ij}'s are the Kobayashi-Maskawa matrix elements [6]. The $SU(2)_L \times U(1)_Y$ quantum numbers of quarks and leptons have all been determined precisely at e^+e^- colliders [7, 8]. The agreement in the measured values of the Weinberg angle obtained in a variety of ways (Fig. 2.1) demonstrates the validity of the gauge principle.

Although the Standard Model has been very successful, the observed particle spectrum is obviously incomplete. The axial vector coupling of the bottom quark to the Z-boson is measured to be one half [10]. The bottom quark thus belongs to an $SU(2)_L$ multiplet with a half-integral isospin, and must have (at least) one $SU(2)_L$ partner which has not been found yet. To establish the idea of the quantum field theory and the gauge principle, it is definitely necessary to discover this missing particle: the top quark.

Fortunately, we have an upper bound on the mass of the top quark, $m_t < 200$ GeV at more than 95% confidence level from analyses of the electroweak radiative corrections [11]. The measurements of particle masses, various cross sections and asymmetries we have accumulated at high-energy experiments are now so precise that we are already sensitive to the quantum effects of undiscovered particles. Thus discovery of the top quark within the predicted mass

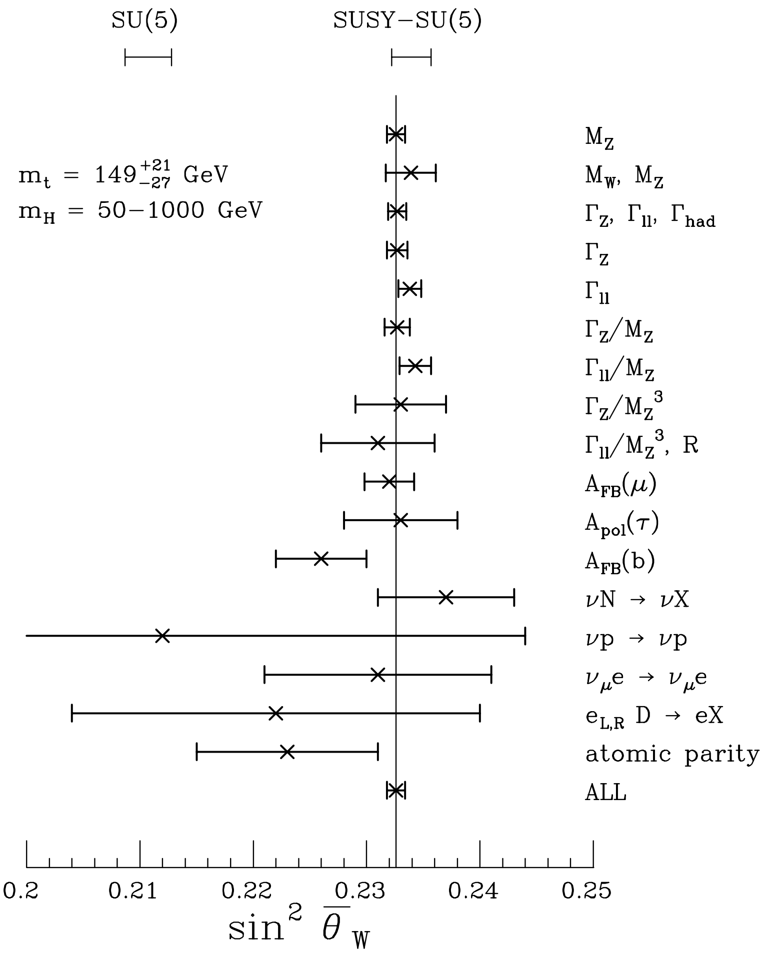

Figure 2.1: The $\overline{MS}$ Weinberg angle $\sin^2 \bar{\theta}_W$ determined in a variety of ways, using the best-fit value $m_t = 149^{+21}_{-27}$ GeV and $m_H = 50$–1000 GeV. The data are taken from Ref. [9].

range, as well as the study of its properties, is an essential step to establish the Standard Model. An e^+e^- collider at $\sqrt{s} = 500$ GeV cannot miss the top quark and provides an ideal place for this purpose.

The study of the top quark is an important subject by itself (Sect. 2.6). First of all, a precise measurement of its mass, $\Delta m_t < 500$ MeV, is possible at the $t\bar{t}$ threshold. The large width of the top quark acts as an infrared cutoff to the QCD interaction, allowing us to make definite theoretical predictions using perturbative QCD [12]. This remarkable feature provides a clean test of perturbative QCD as well as a precise measurement of the strong coupling constant α_s. The width itself is also an important quantity, directly related to the unknown Kobayashi-Maskawa matrix element V_{tb}. If less than unity, it signals the existence of a fourth generation. On the other hand, the top quark may have a larger width than expected due to exotic decay modes like $t \to bH^+$ (charged Higgs boson) or bP^+ (pseudo-Goldstone boson). Furthermore, we may be able to probe the physics beyond the Standard Model from the analysis of the radiative corrections, once we know the mass of the top quark precisely; for example, the radiative corrections from the stop-sbottom sector in the Minimal Supersymmetric Standard Model may be extracted [13].

Another missing constituent of the Standard Model is the Higgs boson. Though this particle plays a key role in the Standard Model to give masses to both the gauge bosons and the

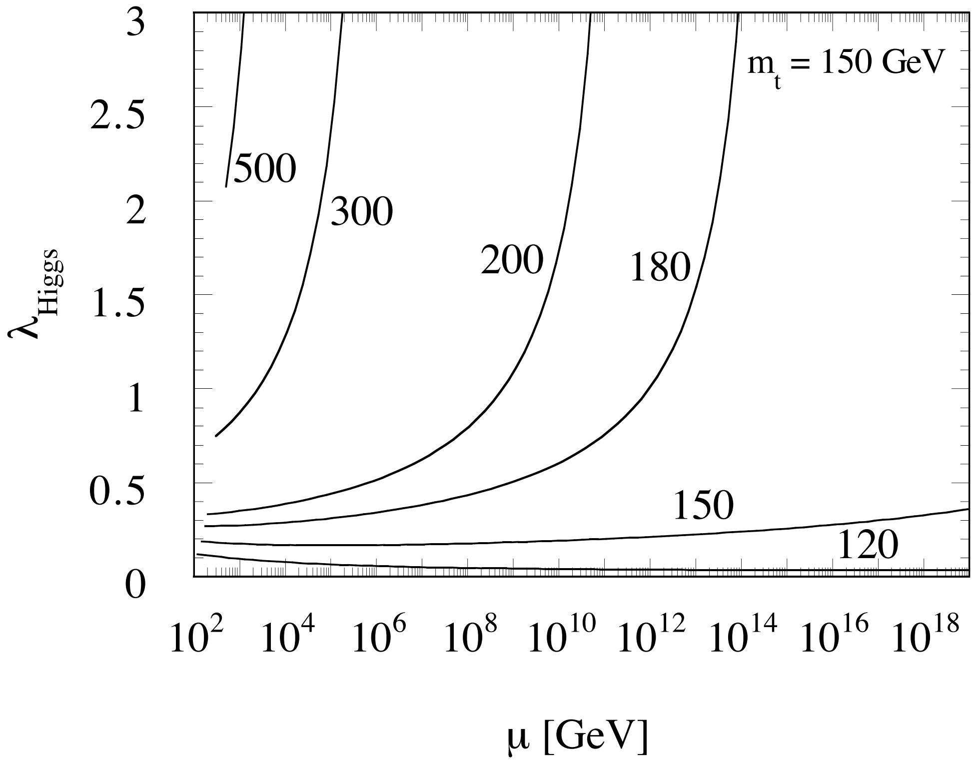

Figure 2.2: The renormalization group flow of the Higgs boson self-coupling constant λ_{Higgs} in the minimal Standard Model. The quoted values are the Higgs boson masses. The top quark mass is assumed to be $m_t = 150$ GeV.

quarks/leptons, little is known about its mass. Recall that the mass of the Higgs boson is related to its four-point self-coupling, which becomes stronger at higher energies. The running of the self-coupling constant is illustrated in Fig. 2.2. If the Higgs boson is relatively heavy, then the self-coupling blows up just above TeV scale. This singular behavior signals the breakdown of the Standard Model above that scale. On the contrary, the Higgs boson lighter than 180 GeV has a self-coupling which remains perturbative up to the Planck scale. Then the standard $SU(3)_C \times SU(2)_L \times U(1)_Y$ gauge theory may be valid up to a very high energy scale. Such a light Higgs boson lies well within the reach of JLC-I.

If the Higgs boson is lighter than ~ 150 GeV, we should be able to test the mechanism of the fermion mass generation. The top quark threshold region is sensitive to the Yukawa potential due to the Higgs boson exchange (Sect. 2.6). The study of the Higgs boson branching ratios can tell us if the Yukawa coupling constants are proportional to the fermion masses (Sect. 2.2). Such tests can be performed only at e^+e^- colliders with a clean environment. In this way, JLC-I is able to thoroughly establish the Standard Model.

2.1.2 Problems in the Standard Model

Once the detailed studies of the top quark to be performed at JLC-I establish the $SU(3)_C \times SU(2)_L \times U(1)_Y$ gauge structure, we may start seriously asking many unresolved questions within the Standard Model. Why do the electric charges of electron and proton exactly balance? Why are the strengths of the gauge interactions so different? Why is the number of generations three? Why do the seemingly independent anomalies from the quark sector and lepton sector cancel? Where do the fermion masses come from? Why is the CP invariance broken? And many others. Among them, the most important question is: Why is the electroweak symmetry broken, and why at the scale $\langle H \rangle = 246$ GeV?

The Standard Model cannot answer these questions. A general belief is that there lies a more fundamental physics at a higher energy scale which leads to the unanswered characteristics of the Standard Model. Then all the parameters and quantum numbers in the Standard Model can be *derived* from the more fundamental description of nature, leading to the Standard Model as an effective low-energy theory. In particular, the weak scale itself $\langle H \rangle = 246$ GeV should be a *prediction* of the deeper theory. The scale of the fundamental physics can be regarded as a cutoff to the Standard Model. Above this cutoff scale, the Standard Model ceases to be valid and the new physics takes over.

In the Standard Model, an elementary Higgs field is introduced to break the $SU(2)_L \times U(1)_Y$ symmetry. The mass term of the Higgs field is of the order of the weak scale. The natural scale one expects for the mass term is, however, the cutoff scale of the theory, since the quantum correction to the mass term is proportional to the cutoff scale squared because of the quadratic divergence. This problem, so-called the naturalness problem, is one of the main obstacles we encounter, when we wish to construct realistic models of the "fundamental physics" beyond the Standard Model. If the cutoff scale of the standard model is near the Planck scale, one needs to fine-tune the bare mass term of the Higgs potential to many orders of magnitude to keep the weak scale very tiny compared to the Planck scale. There are only two known possibilities to solve this problem. One is to assume that the cutoff scale of the Standard Model lies just above the weak scale, regarding the Higgs boson as a composite object. The technicolor scenario discussed in the next section belongs to this class. The other is the introduction of a new symmetry to eliminate the quadratic divergence: supersymmetry.

2.1.3 Technicolor Scenario

Technicolor scenario belongs to the first class discussed above, solving the naturalness problem by setting the cutoff just above the TeV scale. The elementary Higgs field is replaced by the Nambu-Goldstone bosons associated with a dynamical chiral symmetry breaking in the techni-fermion sector [14].

We can approach this scenario by precision experiments. Though these models preserve gauge invariance, there may be higher-dimensional operators induced by the strong dynamics at the TeV scale. Then, these operators appear as anomalous couplings among the gauge bosons, which can be measured with a precision better than 2–3% already at JLC-I, using the processes $e^+e^- \to W^+W^-$, $e^\pm \overset{(-)}{\nu}_e W^\mp$, and $\nu_e\bar{\nu}_e Z$ (Sect. 2.7). The high-luminosity Z-factory is also a good option for the precision measurements (Sect. 2.8), with high sensitivity to the symmetry breaking sector [15].

Although the idea of the dynamical symmetry breaking works beautifully in the gauge sector, it is not easy to generate fermion masses without conflicting the experimental constraints on flavor changing neutral currents. Walking technicolor [16] was proposed as a candidate mechanism to suppress the flavor-changing neutral currents while giving relatively large masses to the fermions. Then, the pseudo-Nambu-Goldstone bosons (techni-pions) are expected to appear below $O(100)$ GeV. Their properties are similar to those of the charged Higgs bosons in the multi-doublet models, whose detection is easy at JLC-I (Sect. 2.6).

Nevertheless, the large mass of the top quark [17] is very difficult to incorporate into this scenario. It is generally accepted that there is yet no well-defined model along this idea, and it is extremely difficult to judge pros and cons experimentally in the absence of concrete prediction. On the contrary, the other scenario to solve the naturalness problem, supersymmetry, provides some definite predictions which can be clearly tested at JLC-I.

2.1.4 Supersymmetry

Supersymmetry (SUSY) [18] is a symmetry between bosons and fermions, and is the only known symmetry which eliminates the quadratic divergence of scalar mass parameters. Since the principal origin of the naturalness problem in the Standard Model is the quadratic divergence of the Higgs mass parameter, its absence in the supersymmetric models allows us to push the cutoff up to the Planck scale [19]. This possibility, that the cutoff scale may be very high, provides us an exciting scenario, that all the weak scale parameters are determined directly from those near the Planck scale, where the supersymmetry is naturally understood in the context of supergravity. Stated conversely, we can probe the physics near the Planck scale from the experiments at the weak scale. Wiping out the "TeV clouds," we may be able to see the physics near the Planck scale [20]. The large hierarchy between the Planck scale and the weak scale is stabilized thanks to the supersymmetry.

The idea that the weak scale parameters are directly determined from a very high energy scale naturally leads to the more interesting concept of the grand unified theory (GUT). GUT assumes that all the three gauge couplings in the standard model are derived from a single gauge coupling constant at a very high energy [21]. The most important prediction of the GUT is that of the Weinberg angle. Historically, the renormalization group analysis [22] showed that the Weinberg angle should be close to 0.2 in the simplest GUT model, in rough agreement with the measured value. Note that the qualitative success of this concept is that the strong coupling is always the strongest, the weak coupling the next, and the electromagnetic one the weakest, due to the simple inequality $3 > 2 > 1$. The successful prediction of the Weinberg angle $\sin^2\theta_W \sim 0.2$ is a concrete manifestation of this qualitative success. Furthermore, the baroque structure of the fermion quantum numbers in the Standard Model was naturally embedded into the $SU(5)$ gauge group, leading to the exact quantization of the electric charge and the precise cancellation of the anomalies. It was also pointed out that the simple GUT models predict equal bottom quark and tau lepton masses at the GUT scale, leading to the correct mass ratio after renormalization down to the GeV scale [23].

Since there are many GUT models, with or without supersymmetry, based on various gauge groups, it is important to be able to distinguish among them by comparing their predictions on the Weinberg angle with its experimental value. The Weinberg angle measured precisely at LEP experiments [11] agrees remarkably well with the prediction of the simplest supersymmetric GUT model [24]. The history of the measurement of $\sin^2\theta_W$ is illustrated in Fig. 2.3. Also shown is the unification of the coupling constants in supersymmetric GUT in Fig. 2.4. Here the supersymmetry successfully combined with the the concept of GUT, in a consistent manner with the assumption of a large cutoff scale.

It is worth mentioning that a heavy top quark has been suggested within the supersymmetric models, before the PEP/PETRA/TRISTAN experiments set a surprisingly high lower bound on its mass. The so-called radiative breaking scenario assumes that the electroweak symmetry breaking is triggered by the top quark Yukawa coupling, whose quantum effect drives the Higgs boson mass squared to negative at lower energies. Indeed, the preferred top quark mass is between 100 and 200 GeV within the scenario [27]. This range is just the one predicted from the precision measurements of the Standard Model.

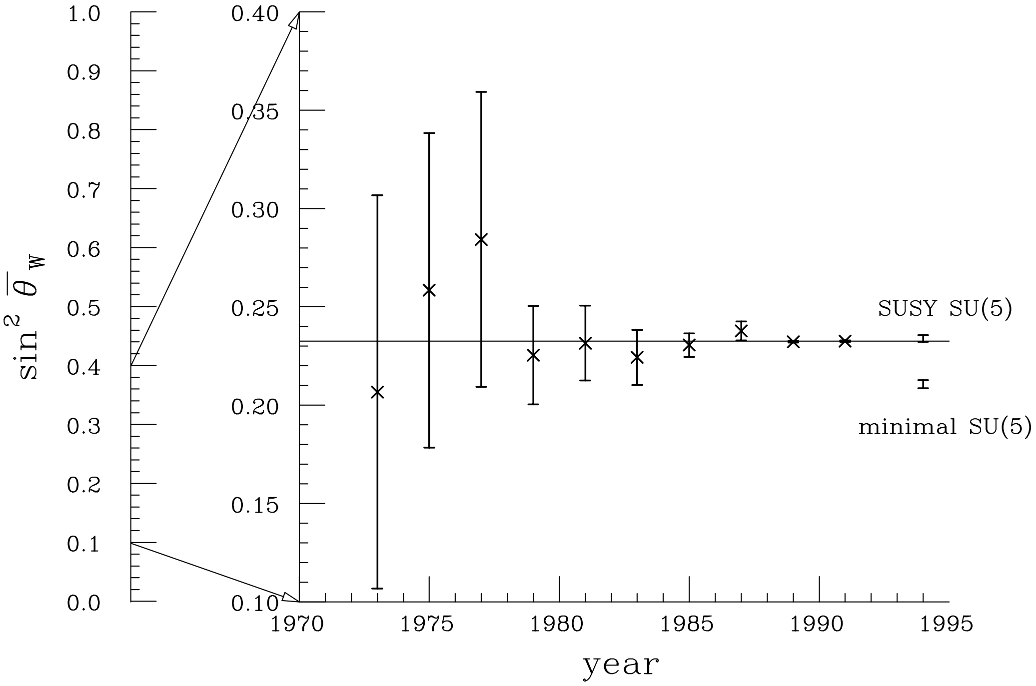

Figure 2.3: The history of the measurements of the Weinberg angle. Also shown are the predictions of the minimal (non-SUSY) $SU(5)$-GUT and minimal SUSY $SU(5)$-GUT.

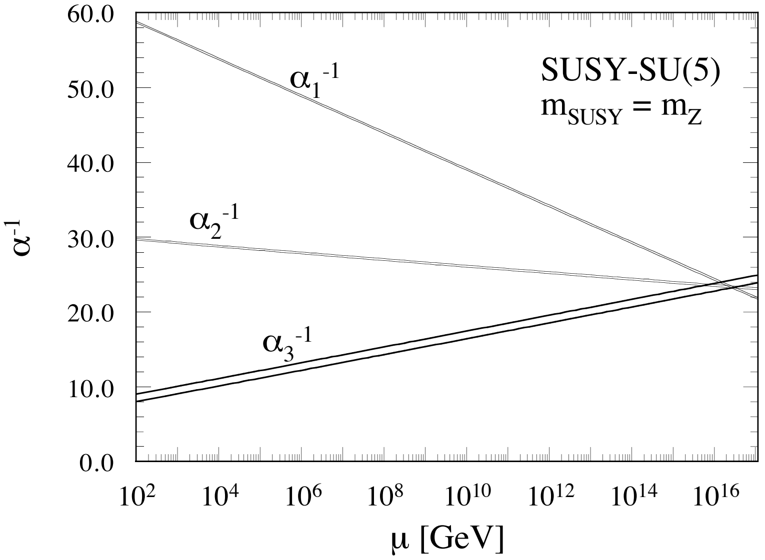

Figure 2.4: The renormalization group flow of the gauge coupling constants in the minimal SUSY Standard Model. The SUSY-breaking scale is set at m_Z.

2.1.5 Light Higgs: Messenger from the Grand Desert

An immediate consequence of SUSY is the existence of a light Higgs boson. It has been known that the lightest Higgs should be lighter than m_Z at the tree-level [28], and it was regarded as one of the main targets at LEP-II. Recently, it was shown that the upper bound on the lightest Higgs boson is raised by the radiative correction due to the top quark Yukawa coupling [25], and the parameter space cannot be exhausted at LEP-II. However, one still has a stringent upper bound on the lightest Higgs boson mass, which is 170 GeV within the minimal SUSY Standard Model. Even the addition of singlets and extra families can push the upper bound only up to 200 GeV [26]. Thus JLC-I is an ideal place to discover SUSY Higgs or otherwise to exclude SUSY completely. On the other hand, it is hard to detect such a light Higgs boson at hadron supercolliders, leaving possibilities to miss it even if supersymmetry does exist.

Once a light Higgs boson is discovered, then we will be able to perform a detailed study on its properties, such as its mass, production cross sections, and decay branching ratios (Sect. 2.2). Such a detailed study is only possible at an e^+e^- collider. Then we may be able to distinguish between the minimal Higgs boson in the Standard Model and non-minimal Higgs bosons like those in its supersymmetric extension. It is also possible that the other components of the Higgs multiplets will be discovered as well. Then careful studies may show whether their properties are those of the general two-doublet models, or those of the supersymmetric model which is more restrictive.

The existence of such a light Higgs is required even without supersymmetry, as long as there exists a "Grand Desert" between the weak scale and a high-energy scale like the Planck-scale, the GUT-scale, or an intermediate scale ($\gtrsim 10^{10}$ GeV) [29]. Since the Higgs self-coupling constant should remain perturbative up to the new physics scale, its mass should be smaller than $\lesssim 200$ GeV in any models (See Fig. 2.2).

Thus, an e^+e^- collider with $\sqrt{s} \lesssim 300$ GeV allows us to perform a definitive test on the "Grand Desert" hypothesis. If a light Higgs boson is discovered at JLC-I, it strongly supports the idea of grand unification. If *not*, there *must* be a low-lying new physics scale, and all the conventional GUT models will have to be abandoned.

2.1.6 Roads to the Planck Scale

If a light Higgs boson is indeed found, then we should go to the next step, to search for superparticles directly. For SUSY being relevant to solve the naturalness problem, the masses of superparticles should be lighter than $O(1)$ TeV. Among them, the color-singlet superparticles like sleptons, charginos, and neutralinos are expected to be lighter than the colored superparticles. We have a good chance to discover one of the color-singlet superparticles in the energy range $\sqrt{s} = 300$ to 500 GeV. On the other hand, colored superparticles like gluino and squarks, main targets at hadron supercolliders, are in general relatively heavy and require much higher energies to discover. The discovery potential of proposed hadron supercolliders is comparable with that of JLC-I.

Since the supersymmetry allows us to push the cutoff scale up to the Planck scale, the study of its low-energy consequences will enable us to probe the physics at the Planck scale. It is generally believed that the origin of the SUSY breaking should be attributed to the supergravity interactions. In other words, the superparticle masses are the reminiscent of the dynamics at the Planck scale. To measure the SUSY breaking parameters at the weak-scale is the most important task to explore physics at the Planck scale. Then we may obtain clues to the truly unified theory including gravity, like superstring theory. For example, the discovery of the sleptons alone will give us a good opportunity to measure the SUSY-breaking parameters at the Planck scale. We can predict the masses of squarks and gluinos from the study of the sleptons, within the minimal supergravity model. The large beam polarization at JLC-I will allow clear separation of left-handed and right-handed sleptons and the study of energy distributions of the decay products will provide the mass of the lightest supersymmetric particle. The study of interference between s-channel and t-channel amplitudes will resolve the neutralino mass spectrum. If lucky, we can measure all but one parameters within the minimal supergravity model. This amusing possibility is discussed in detail in Sect. 2.4.

The clean environment, high luminosity, and the large beam polarization at JLC-I may lead us to make an entirely new step towards the deeper understanding of nature.

2.2 The Light Higgs(h^0)

2.2.1 Introduction

One of the most important physics targets of JLC-I is the Higgs particle. Since the mass of the Higgs particle is a parameter of the Standard Model, its prediction is only possible when we go beyond the Standard Model. As described in the previous section, the low mass Higgs particle ($\lesssim$ 200 GeV) is a general conclusion of models based on the GUT and Grand Desert scenario, while composite Higgs models such as technicolor models allow a high mass Higgs particle. In the case of the former scenario, many SUSY particles may exist below 1 TeV according to the natualness argument. While in the latter case, the exploration of multi-TeV energy region will be required to fully understand the underlying dynamics. Therefore, the search for the low mass Higgs particle will be the branch point to decide the future direction of collider physics.

The current lower limit on the mass of the Standard Model Higgs particle is 58 GeV at the 95 % confidence level [31]. The LEP II will cover the mass region up to 80 $\sim$ 90 GeV [32]. Future hadron colliders (LHC and SSC) will be sensitive to the Standard Model Higgs particle of a mass from 80 GeV to about 1 TeV[66]. At hadron colliders, the search for the Standard Model Higgs particles with a mass larger than $2 \times m_Z$ is relatively easy by using the $H^0 \to Z^0 Z^0 \to 4l$ mode. However, the search for an intermediate mass Higgs ($m_Z < m_H < 2 \times m_Z$) is not easy at hadron colliders. Especially if $m_H \lesssim 130$ GeV, one can use only one decay mode $H_{SM} \to \gamma\gamma$, with a small branching ratio of about 10^{-3}, therefore one needs high luminosity and ultimate detector performance. The situation becomes much worse in the case of the SUSY Higgs, as the branching ratio for $h^0 \to \gamma\gamma$ is suppressed to be $\sim 10^{-4}$ or much smaller in a large domain of the parameter space, due to the increase of the dominant decay width $\Gamma(h^0 \to b\bar{b})$. It was reported that hadron colliders can not discover any of the MSSM Higgs particles, if model parameters are in some unlucky region[33].

As described in the previous section, the recent precision measurements strongly favours the scenario with GUT, Grand Desert and low energy SUSY particles, while non-GUT scenarios, such as Technicolor Model now facing a tough experimental challenge. Therefore the search for low mass Higgs particles becomes more important than ever. As will be discussed in the following subsections, at e^+e^- colliders, the Higgs particle can be searched for, using the main decay mode. Therefore, the search at JLC-I will never miss the Higgs in the intermediate mass region. In this sense, the search at JLC-I is complementary to that at Hadron colliders.

In the minimal supersymmetric standard model (MSSM), the Higgs sector consists of two doublets, resulting in five physical Higgs particles: two CP-even scalars, i.e. a light one (h^0) and a heavy one (H^0), one CP-odd scalar (A^0), and a pair of charged Higgs ($H^{\pm}$). There are

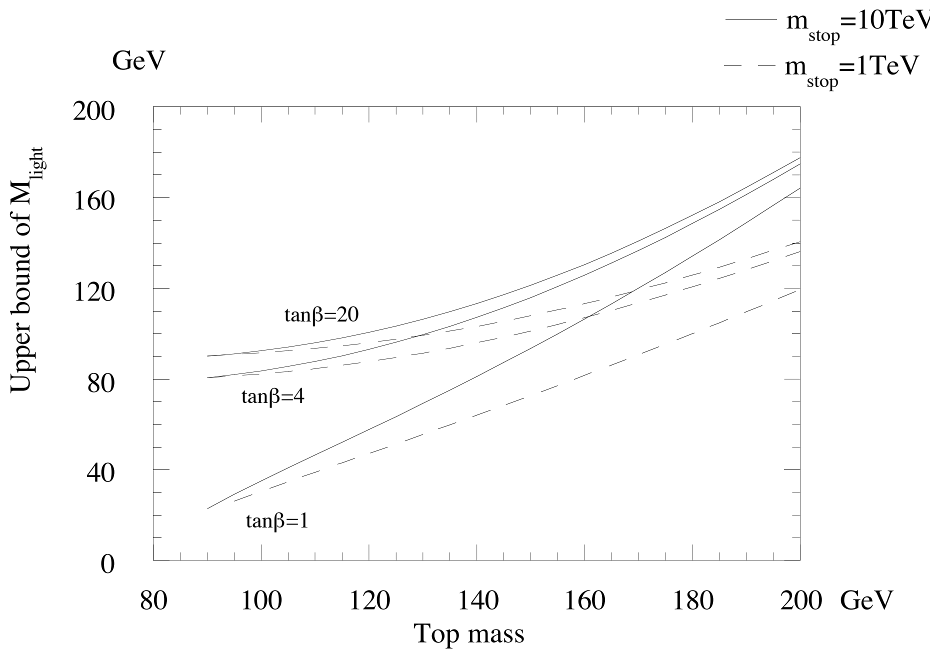

Figure 2.5: The Higgs mass as a function of the top quark mass for various $\tan\beta$ values and two extreme SUSY scale cases. Solid line correspond to $m_{\tilde{t}} = 10$ TeV and trilinear soft breaking parameter (A term) equal to $\sqrt{6}$, dashed line $m_{\tilde{t}} = 1$ TeV and A=0. These masses are calculated with a formula improved by renormalization group equations[67].

relations among the masses of these particles. m_{h^0}, m_{H^0}, and $m_{H^\pm}$ can be given in terms of m_{A^0} and $\tan\beta$, where $\tan\beta$ is the ratio of the two vacuum expectation values of two Higgs doublets. Especially, the lightest Higgs boson mass is less than the mass of Z^0 at the tree level. But, when the radiative correction is taken into account, the upper bound can exceed m_{Z^0} due to the top and stop loops. The correction to the upper bound of the lightest Higgs mass squared is proportional to $m_t^4 \ln \frac{m_{\tilde{t}}}{m_t}$, where $m_{\tilde{t}}$ is the scalar top mass. The upper bound on m_{h^0} for various $\tan\beta$ values and two extreme SUSY scales is shown in Fig. 2.5 as a function of the top quark mass. Experimentally, the top quark mass is bounded between 89 GeV and 200 GeV[30, 11]. If the low energy supersymmetry is the solution to the naturalness problem, the SUSY scale should not exceed O(10) TeV. Taking these bounds into account, m_h should be less than 180 GeV.

Even if one extends the MSSM by introducing a gauge singlet Higgs or adding extra matter super multiplets, one can still obtain a tight upper bound on the lightest Higgs boson mass as long as one assumes GUT. In these models, the lightest Higgs boson mass does not exceed 200 GeV, if the SUSY breaking scale is 1 TeV.

The tree level total cross sections of the processes $e^+e^- \to H^0_{SM}Z^0$ (for various m_H values), $e^+e^- \to Z^0Z^0$, and $e^+e^- \to W^+W^-$ are shown in Fig. 2.6, as functions of the center of mass energy. At $\sqrt{s} = 300$ GeV, the total cross section of $e^+e^- \to H^0_{SM}Z^0$ with $|\cos\theta_H| < 0.7$ is $\sim$30fb. Therefore, an integrated luminosity of 5 fb^{-1} will be sufficient for the discovery of the Standard Model Higgs particle with a mass up to 200 GeV.

In the case of the SUSY Higgs (MSSM), the cross sections are related to that of the Standard Model Higgs particle as follows:

$$\sigma(e^+e^- \to h^0 Z^0) = \sin^2(\beta - \alpha)\sigma(e^+e^- \to H_{SM} Z^0)$$

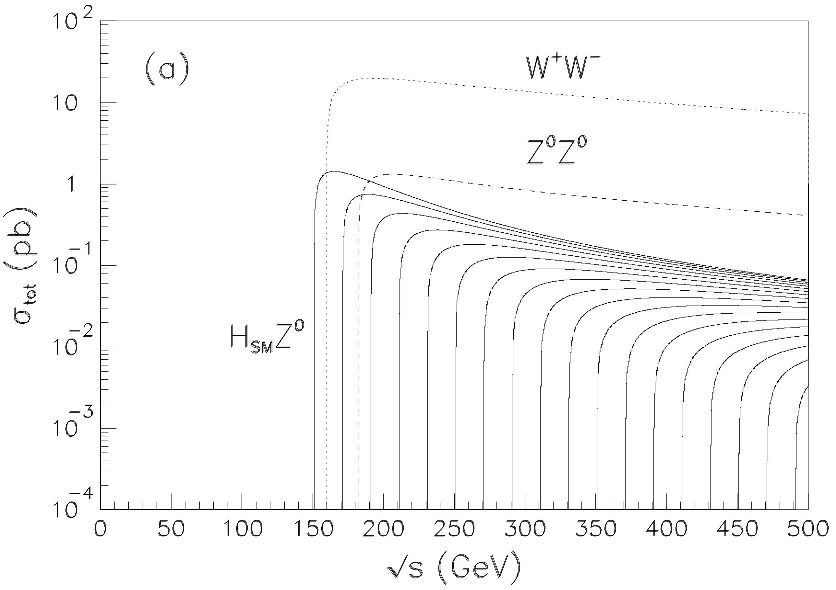

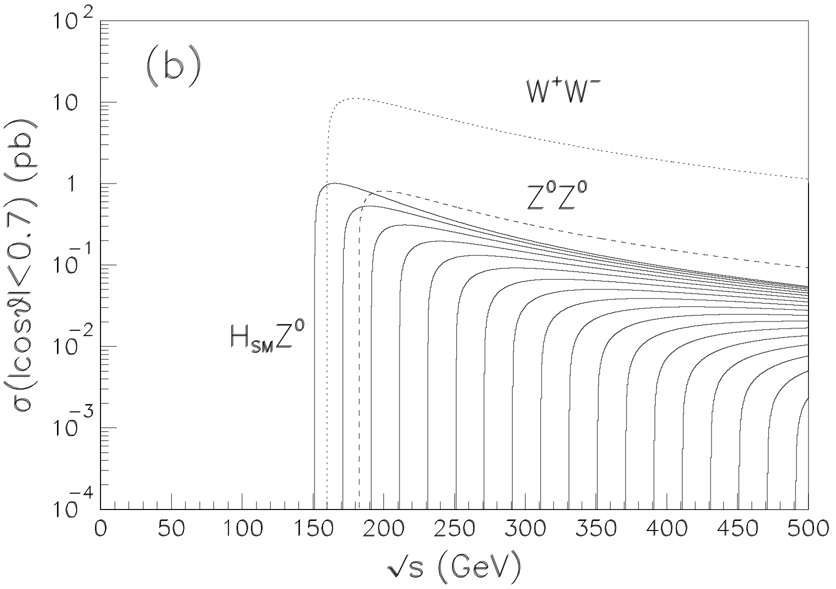

Figure 2.6: (a) The total cross sections for the reactions $e^+e^- \rightarrow W^+W^-$ (dotted curve), $e^+e^- \rightarrow Z^0Z^0$ (dashed curve) and $e^+e^-\!\rightarrow H^0_{SM}Z^0$ (solid curves:$m_{H_{SM}}$ from 60 GeV to 400 GeV in 20 GeV steps) as functions of the center of mass energy. (b) A similar figure with an angular cut: $|\cos\theta| < 0.7$.

$$\sigma(e^+e^- \to H^0Z^0) = \cos^2(\beta-\alpha)\sigma(e^+e^- \to H_{SM}Z^0)$$

where α is the mixing angle of the CP-even Higgs particles. The value $\sin^2(\beta-\alpha)$ is a function of $(\tan\beta, m_A)$ in the MSSM, and is close to 1 if m_A is large ($m_A \gtrsim 150$ GeV) while it is close to 0 if m_A is small. When m_A is large, the masses of H^0 and $H^\pm$ are close to m_A and the mass of h^0 is close to the maximum depending on m_t, $m_{\tilde{t}}$, and $\tan\beta$. When m_A is small ($m_A \lesssim 150$ GeV), the masses of H^0 and $H^\pm$ are also small, therefore, all Higgs particles are kinematically accessible at JLC-I.

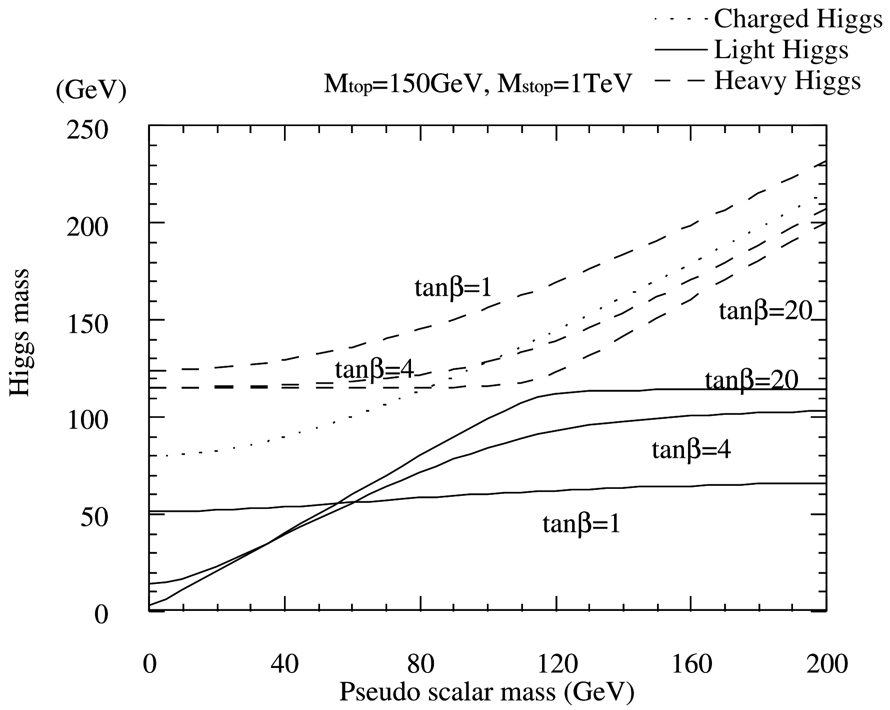

Figure 2.7: The mass of h^0, H^0, and $H^\pm$ in MSSM as a function of the mass of A^0 for various $\tan\beta$ values.

Thus the MSSM Higgs phenomenology at JLC-I can be summarized as either the production of only the light Higgs particle with a cross section similar to that of the Standard Model Higgs particle or the simultaneous productions of h^0, H^0, A^0, and $H^\pm$. In any case, the sum of the cross section $e^+e^- \to h^0Z^0$ and $e^+e^- \to H^0Z^0$ is more than 60fb at $\sqrt{s} = 300$ GeV, even if the top quark mass and the SUSY scale are close to their maximum values. This feature guarantees the discovery of at least one Higgs particle at JLC-I if nature is really SUSY-GUT.

In the following subsections, we will describe the search strategy for the Standard Model Higgs particle and a possible strategy for the study of the Higgs particle after the discovery. The analysis will also applicable to the search of h^0 in the MSSM when m_A is large. The searches for A^0, H^0, and $H^\pm$ will be described in the next section.

2.2.2 Discovery Strategy of Higgs Boson

At JLC-I, the detection of the Standard Model Higgs particle in the intermediate mass region is easy[37, 36], using the process $e^+e^- \to H^0_{SM}Z$. Depending on the decay modes of Z^0, event topologies of the process $e^+e^- \to H^0_{SM}Z^0$ are classified into (1) $\nu\bar{\nu}b\bar{b}$, (2) $l\bar{l}b\bar{b}$, and (3) $q\bar{q}b\bar{b}$. A typical event of each topology is shown in Fig. 2.8. The Higgs will be observed as a peak in the invariant mass distribution of two-jet system, requiring the rest of the system (two jets, two leptons, or nothing, depending on the topologies) to be consistent with Z^0.

The main background comes from the processes $e^+e^- \to Z^0Z^0$ and $e^+e^- \to W^+W^-$, whose differential cross sections peak in the forward direction. Therefore, the key points in the Higgs reconstruction are (1) to select events produced in the central region (for example, require reconstructed Higgs and Z directions to satisfy an angular cut such as $|\cos\theta| < 0.7$), (2) to tag the b-jets efficiently, and (3) to achieve a high resolution for the invariant mass of the Higgs. For the second point, we will use a CCD-type vertex detector as described in the following chapter. It will enable us to tag $b\bar{b}$ jets from the Higgs decays with an efficiency higher than 61 % (double tag). The third point is crucial for Higgs studies, especially when its mass is close to that of W or Z. The required resolution can be realized by high resolution calorimetry and tracking systems, which can identify electrons and muons in jets and can link each track to its corresponding calorimeter cluster. A possible detector design will be described in the following chapter.

By the first e^+e^- collision at JLC-I, the mass of the top quark will be fixed by the collider experiments at Fermi Laboratory if the mass is low enough for discovery, or the precision measurement at LEP-II will constrain the top quark mass with a good precision ($\Delta m_t = 5 \sim 10$ GeV). The initial beam energy of JLC-I will be set at $2 \times m_{top}$ so as to guarantee the physics output from the study of the top quark. This run will also serve as the "Discovery Run" of the Higgs particle, because the threshold of the Higgs particle production by the process $e^+e^- \to h^0Z^0$ is lower than $2 \times m_{top}$ as long as $m_{top} > 90$ GeV (see Fig. 2.5).

Let's assume that the top quark mass is 150 GeV. We start the "Discovery Run" at $\sqrt{s} =$ 300 GeV with a relatively wide beam energy spread of 2% full width. Under this condition, JLC-I will provide a luminosity of $3 \times 10^{33}\mathrm{cm}^{-2}\mathrm{s}^{-1}$ corresponding to an integrated luminosity of $\int Ldt = 30\mathrm{fb}^{-1}$ a year ($\sim$ 100 running days). Fig. 2.9 shows the reconstructed m_h distributions at the stage of $\int Ldt$=4fb^{-1}, for the signal process: $e^+e^- \to H^0_{SM}Z^0$ with $m_{H^0_{SM}}$= 80, 100, 120, 140, 160, and 180 GeV, and the background process: $e^+e^- \to Z^0Z^0$. For the $Z^0 \to l^+l^-$ channel, we apply a kinematical fit to suppress the effect of the beam energy spread and initial state radiation. A clean peak, well separated from that of the $e^+e^- \to Z^0Z^0$ background, can be observed in the $\nu\bar{\nu}b\bar{b}$ and $q\bar{q}b\bar{b}$ modes already at 4fb^{-1}, if $m_{H^0_{SM}}$ is less than 160 GeV. If $m_{H^0_{SM}}$ is greater than 160 GeV, the other decay mode such as $H^0_{SM} \to W^+W^-$ will be useful for the Higgs discovery at the stages of low integrated luminosity. When we accumulate 30 fb^{-1}, a clean Higgs signal well separated from the Z^0 peak can be observed in each of the three decay channels as seen in Fig. 2.10, if the difference between $m_{H^0_{SM}}$ and m_Z is greater than $\sim$10 GeV. The measurements in the three decay channels are independent of one another. Even if $m_{H^0_{SM}}$ is close to m_Z and the signal peaks are overlapped with the background $e^+e^- \to Z^0Z^0$ peaks, the total numbers of events in the overlapped peaks will hint the existence of h^0[38]. In addition, the difference between the decay angular distribution of Z^0 and H^0_{SM} will help us project out the Higgs signal[39].

In the Discovery Run, the distribution of the recoil mass m_H^{rec} in the decay channel $H^0_{SM} \to b\bar{b}$ and $Z^0 \to \ell^+\ell^-$ is strongly affected by the relatively large beam energy spread as shown in Fig. 2.11a. An idea to reduce this effect is to collide the higher energy positrons with the lower energy electrons and vice versa such that the center of mass energy is kept constant. With this technique we can control the center of mass energy to $\Delta\sqrt{s}/\sqrt{s} = 0.2\%$ full width, although the system may be boosted along the beam axis. Fig. 2.11b shows the m_H^{rec} distribution fairly improved by this technique.

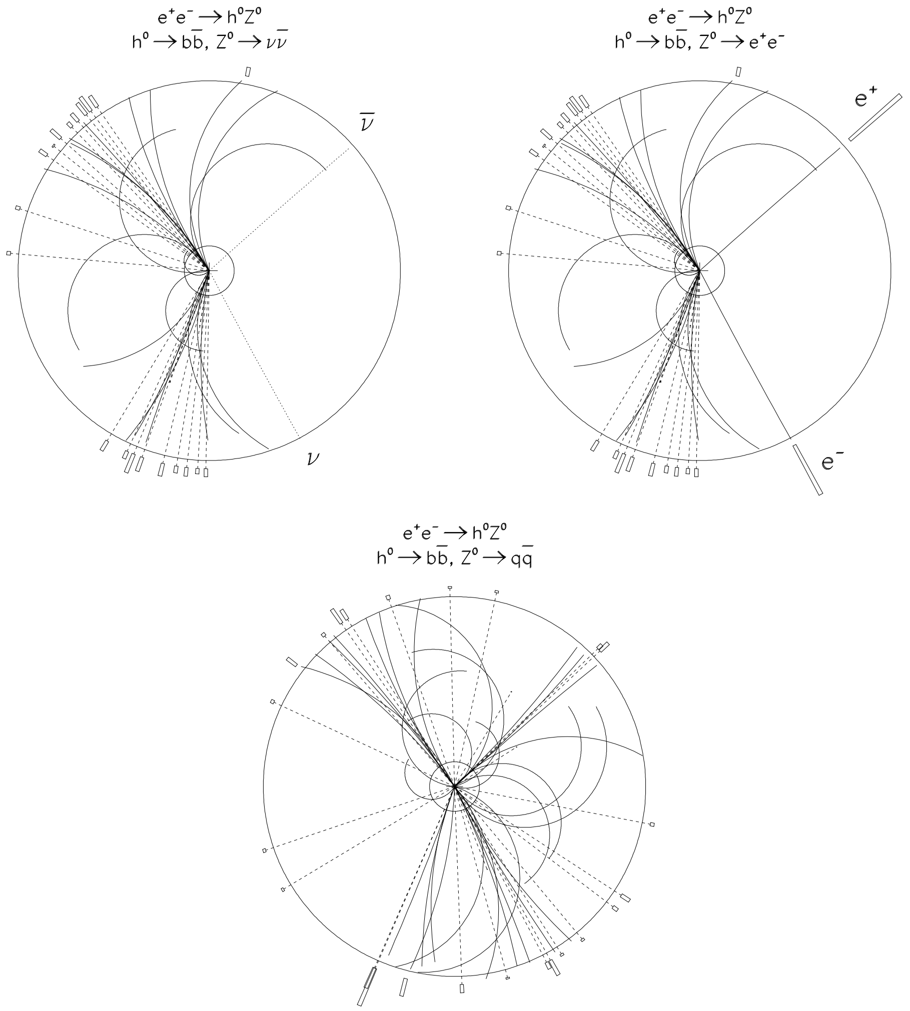

Figure 2.8: Typical $e^+e^{\to}H^0_{SM}Z^0$ events with $m_{H_{SM}} = 120$ GeV at $\sqrt{s} = 300$ GeV: (a) $H^0_{SM} \to b\bar{b}$ and $Z^0 \to \nu\bar{\nu}$, (b) $H^0_{SM} \to b\bar{b}$ and $Z^0 \to e^+e^-$, (c) $H^0_{SM} \to b\bar{b}$ and $Z^0 \to q\bar{q}$. In pictures (a) to (c), the solid curves represent tracks of the charged particles in the central tracking chamber with a magnetic field of 2.0 Tesla and active radius of 0.3 to 2.3 m, while the dotted lines show photon emissions. The surrounding boxes are electromagnetic clusters, and the lengths of the boxes correspond to their energies.

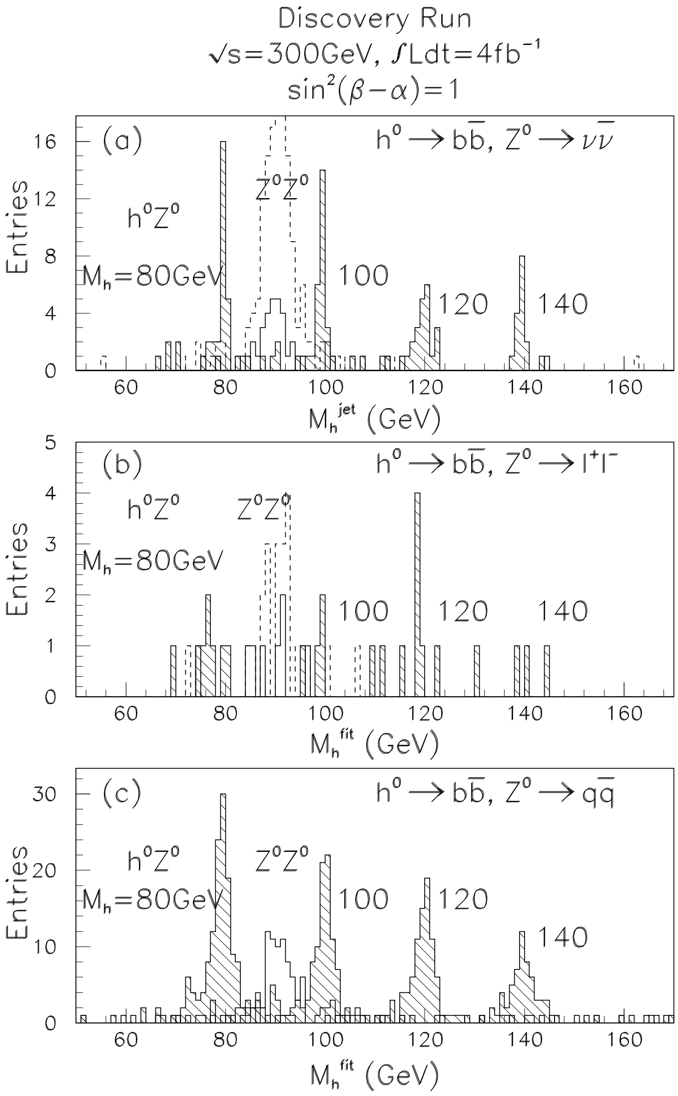

Figure 2.9: The reconstructed mass distributions for the three decay channels after the Discovery Run of $\int Ldt = 4\text{fb}^{-1}$. (a) The m_h^{jet} distribution for the decay channel $H^0_{SM} \to b\bar{b}$ and $Z^0 \to \nu\bar{\nu}$. (b) The m_h^{fit} distribution for the decay channel $H^0_{SM} \to b\bar{b}$ and $Z^0 \to \ell^+\ell^-$. (c) the m_h^{fit} distribution of the decay channel $M^0_{SM} \to b\bar{b}$ and $Z^0 \to q\bar{q}$. In the figures, the hatched histograms are for the signal process $e^+e^- \to H^0_{SM}Z^0$ with $m_{H^0_{SM}}$=80, 100, 120, 140, 160, and 180 GeV. The blank histograms are for the background process $e^+e^- \to Z^0Z^0$. The dashed histograms in figures (a) and (b) are for the background process $e^+e^- \to Z^0Z^0$ without b-tagging.

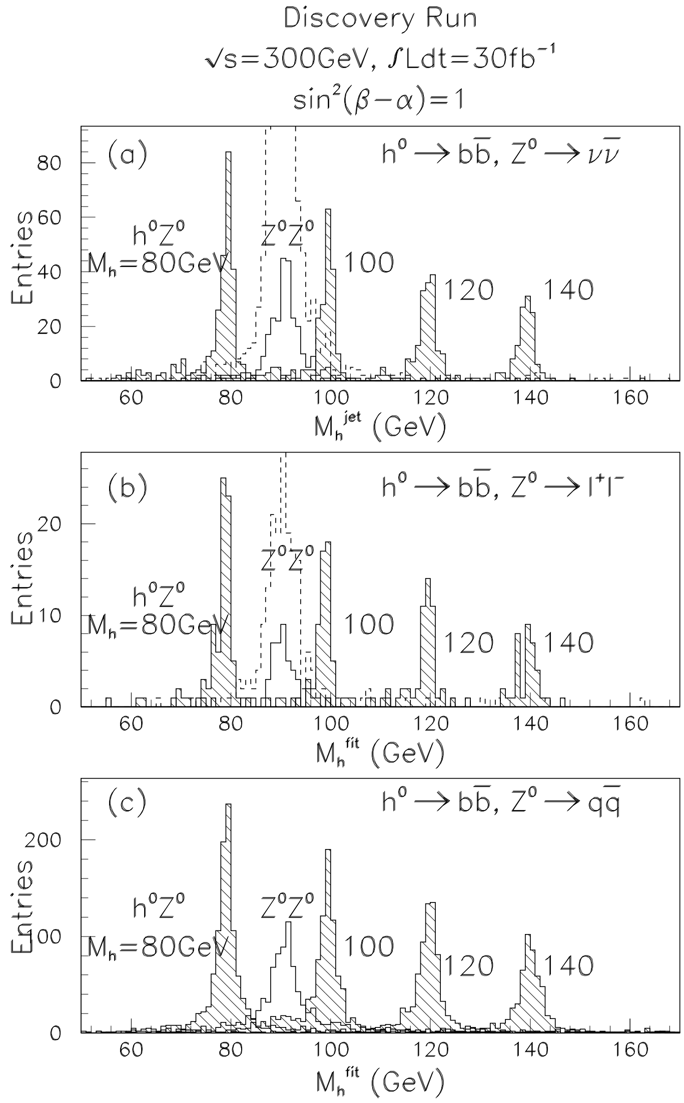

Figure 2.10: Same as Fig. 2.9, but with an integrated luminosity of 30fb^{-1}

If the Discovery Run tells us that m_{H^0} is close to m_Z, we move to the "Precision Mode" with a small beam energy spread of 0.4% full width and $\sqrt{s} = 200$ GeV. We assume that the luminosity is $1 \times 10^{33}\mathrm{cm}^{-2}\mathrm{s}^{-1}$ under this condition. We utilize here the recoil mass m_h^{rec} in the decay channel of $h^0 \to b\bar{b}$ and $Z^0 \to \ell^+\ell^-$. Fig. 2.12 shows the recoil mass distribution for an integrated luminosity of 10 fb^{-1} ($\sim$100 days). Because of the small beam energy spread (and the good momentum resolution), the mass resolution is much better than the total decay width of Z^0. We can thus find a clean signal peak even if it is right on the top of the background peak from $e^+e^- \to Z^0Z^0$.

2.2.3 Detailed Study of Higgs Properties

Once a Higgs particle is discovered, a detailed study should come next. We will set the beam energy at the maximum of the Higgs production cross section and JLC-I is turned into a Higgs factory. The question to be answered here is whether the Higgs sector is minimal or

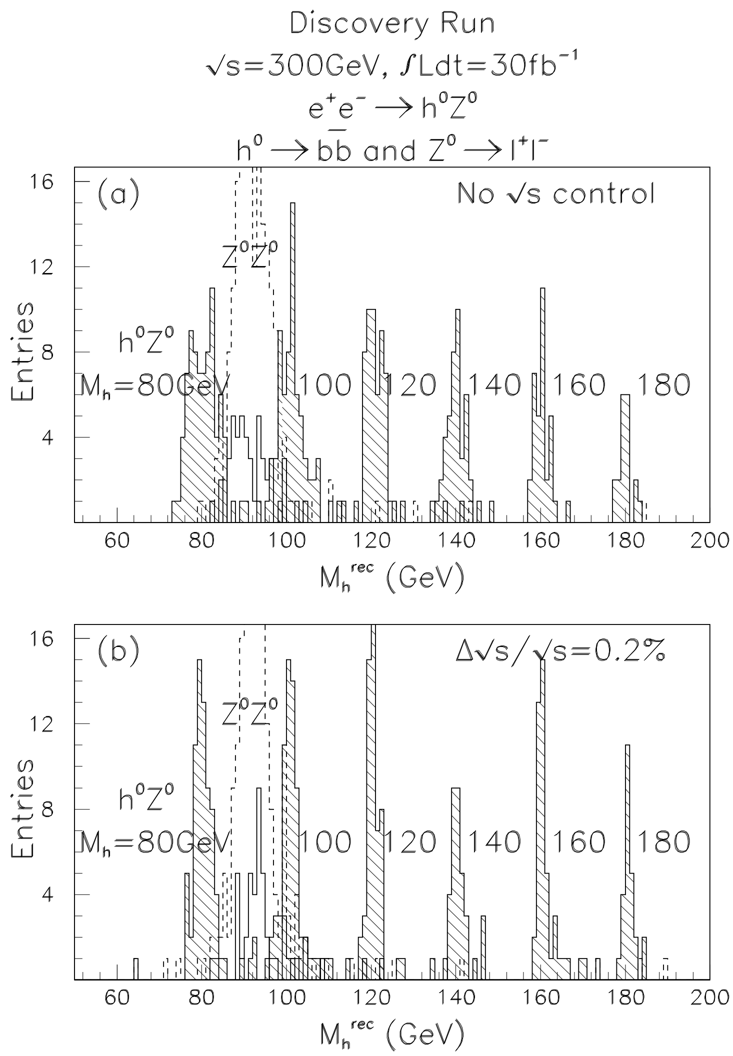

Figure 2.11: Comparison of the recoil mass distributions for the decay channel of $H^0_{SM} \to b\bar{b}$ and $Z^0 \to \ell^+\ell^-$, with the Discovery Run of $\int Ldt = 30\text{fb}^{-1}$: (a) without and (b) with the control of $\sqrt{s}$ (see text). The hatched histograms are for the signal process $e^+e^- \to H^0_{SM}Z^0$ with $m_{H_{SM}}$=80, 100, 120, and 140 GeV. The blank and dotted histograms are for the background process $e^+e^- \to Z^0Z^0$, with and without b-tagging, respectively.

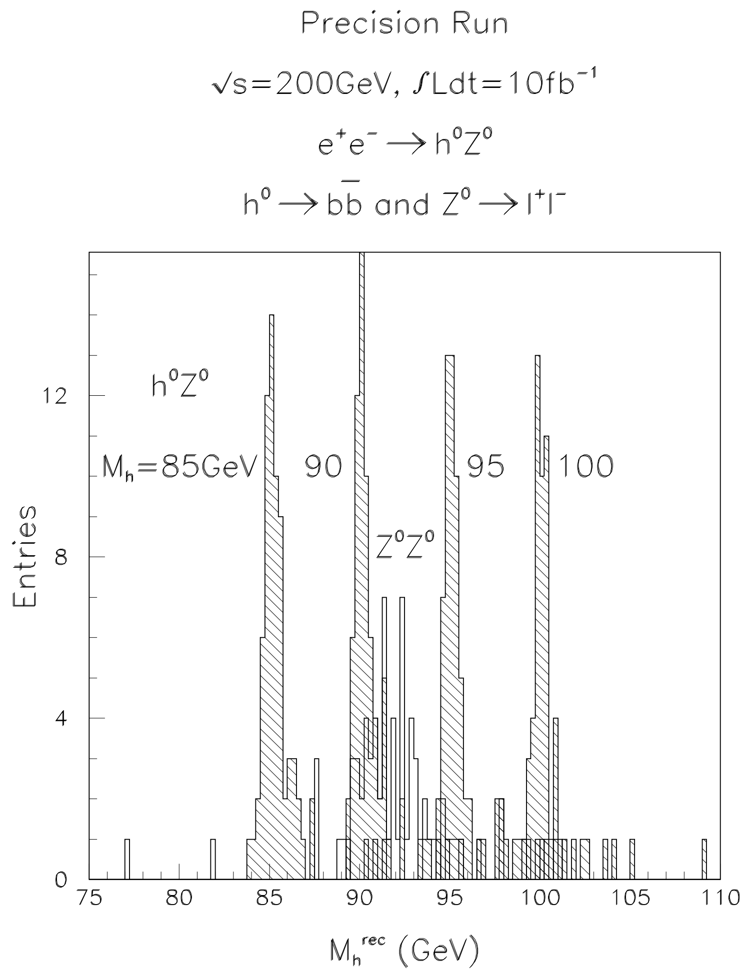

Figure 2.12: The recoil mass distributions of the decay channel of $H^0_{SM} \to b\bar{b}$ and $Z^0 \to \ell^+\ell^-$, with the Precision Run of $\int Ldt = 10\text{fb}^{-1}$. The hatched histograms are for the signal process $e^+e^- \to H^0_{SM}Z^0$ with $m_{H_{SM}}$=85, 90, 95, and 100 GeV. The blank histogram is for the background process $e^+e^- \to Z^0Z^0$, with b-tagging.

non-minimal. Precise measurements of the production cross section and the decay width will answer this question.

Fig. 2.13 shows the contours of the total width of the MSSM Higgs in the m_A and $\tan\beta$ plane. When m_A is small and $\tan\beta$ is large, the total width of the MSSM Higgs becomes very large due to the large coupling to $b\bar{b}$, compared to the total width of the standard model Higgs in this mass range which is about 5 MeV. Since we can measure the total width down to 200 MeV, we can establish the non-minimality of the Higgs boson, when m_A is smaller than 120 GeV and $\tan\beta$ is greater than 8.

Another way to establish the non-minimality of the Higgs boson is to measure the total cross section of $e^+e^- \to h^0Z^0(\sigma_{Zh})$ multiplied by Br$(h \to b\bar{b})$ and to compare it with the standard model prediction. The number of events observed in $\nu\bar{\nu}h$ and $q\bar{q}h$ mode with b-tagging is proportional to $\sigma_{Zh} \times Br(h \to b\bar{b})$. A detailed Monte Carlo simulation showed that, if m_h = 110 GeV, we can accumulate 2000 $\nu\bar{\nu}h$ and $q\bar{q}h$ events total, when we accumulate about 80 fb^{-1} of data. Therefore we can measure $\sigma_{Zh} \times Br(h \to b\bar{b})$ with an error of 2%

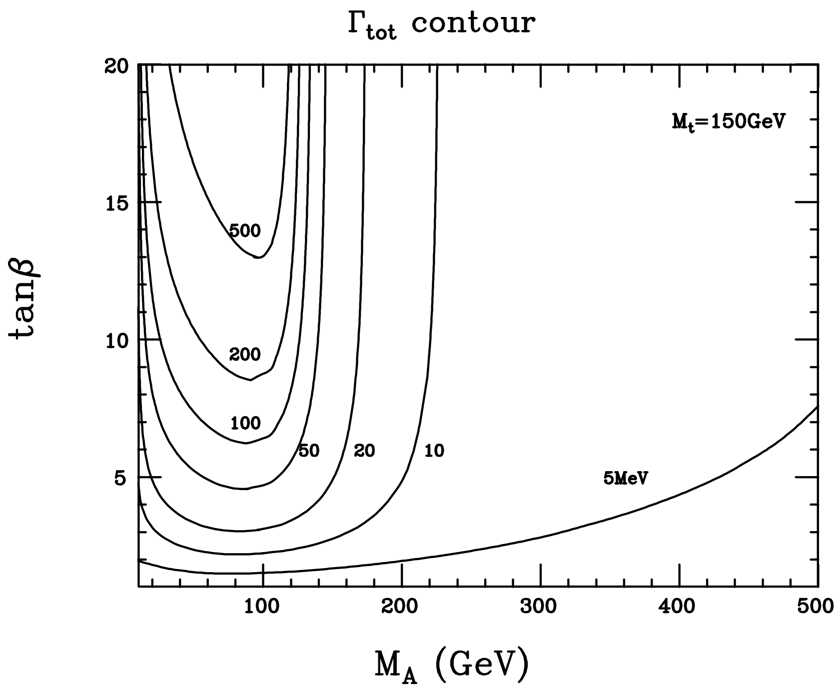

Figure 2.13: The contour of the total width of h^0. In this calculation, $m_t = 150$ GeV, $m_{SUSY} = 1$ TeV, therefore, $m_h < 120$ GeV. The total width of the Standard Model Higgs (m_H) for this mass region is a few MeV at maximum.

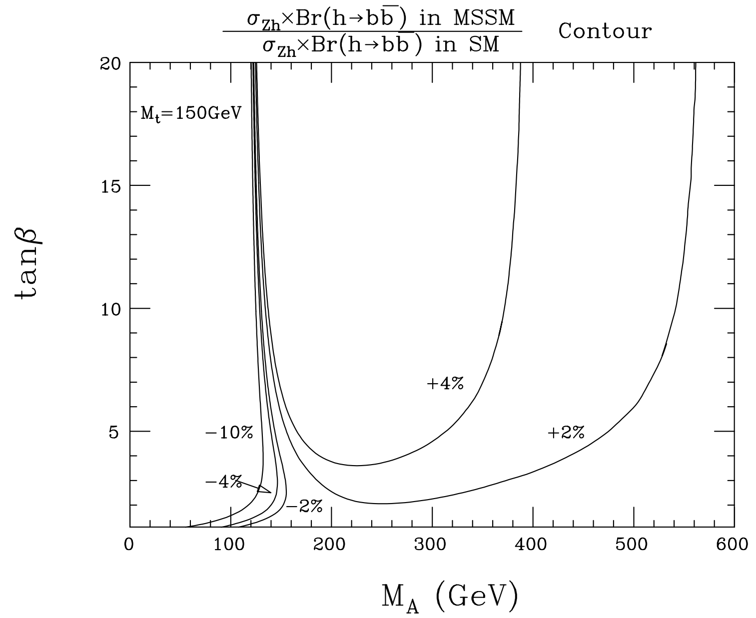

Figure 2.14: $\sigma \times Br(h^0 \to b\bar{b})$ in the MSSM compared with that of the Standard Model.

(1σ). The difference of the $\sigma_{Zh} \times Br(h \to b\bar{b})$ in the MSSM from the standard model($\Delta\sigma_{Zh}$) is shown in Fig. 2.14 as contours in the m_A and $\tan\beta$ plane. In the small m_A region, $\Delta\sigma_{Zh}$ is negative because σ_{Zh} is smaller than the standard model value due to the $\sin(\beta - \alpha)$ factor in the ZZh vertex. Although σ_{Zh} is quite close to the standard model value in the large m_A region, $Br(h \to b\bar{b})$ is still significantly larger than the standard model value, thereby extending the sensitivity to the large m_A region.

The decay branching ratios of h^0 also provide important information about the Higgs properties. The most interesting decay channel is $h^0 \to \gamma\gamma$. The branching ratio is $\sim 10^{-3}$ for the Standard Model Higgs, but can be $\sim 10^{-4}$ or much smaller for large $\tan\beta$ and relatively small m_A in the MSSM. Since the signature of this mode is very clean, the measurement of this mode will provide an important constraint to the Higgs sector, when we accumulate enough statistics to study such a rare decay mode ($\gtrsim$ 100 fb^{-1}). The Br($h \to c\bar{c}$) is equivalently important. It is several percent in the standard model, but can be much smaller in the MSSM. Though the identification of charm quarks in a large b-jet background is experimentally challenging, the non-observation of $c\bar{c}$ mode in the Higgs decay will confirm the non-minimality.

The above measurements will set strong constraints on the parameter space ($\tan\beta$,m_A) and will possibly distinguish the MSSM Higgs from the Standard Model Higgs. The estimation of m_A will be invaluable in setting the energy range of JLC-II.

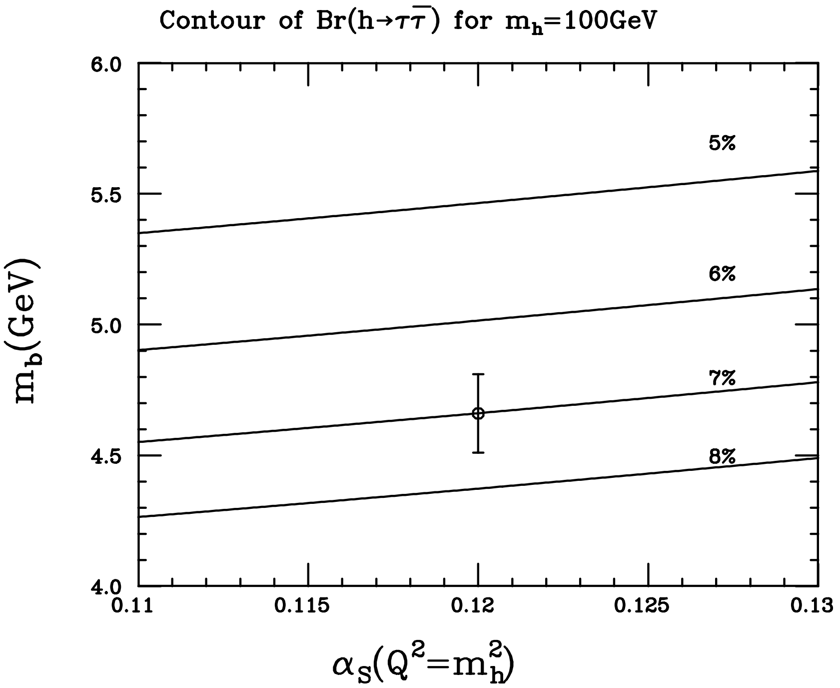

Figure 2.15: The contour of $Br(h^0 \to \tau\bar{\tau})$ in the α_s and m_b plane. The parameters of the Higgs boson are adjusted to obtain m_h=100 GeV.

2.2.4 Br($h^0 \to \tau\bar{\tau}$) Measurement.

The Higgs studies also provide us with a possibility to probe higher-energy-scale physics through the mass ratio of the bottom quark to the tau lepton, which has been successfully predicted by the SUSY-GUT. At present, large theoretical error on m_b from the $b\bar{b}$ potential prevents us from making a precise test of GUT predictions. However, if the mass of the Higgs boson is in the region where the main decay mode is $b\bar{b}$, we can make a precise measurement of the b-quark mass by measuring the branching ratio for $h^0 \to \tau\bar{\tau}$. In any models which generate the b-quark and τ lepton masses from the same Higgs doublet, the ratio of the branching fraction for $h^0 \to b\bar{b}$ and $h^0 \to \tau\bar{\tau}$ is completely fixed up to the ambiguities in m_b and α_s. Fig. 2.15 shows contours of the branching ratio for $h^0 \to \tau\bar{\tau}$ in the plane of α_s and m_b. For 100 fb^{-1} of data, we will have about 200 events of $e^+e^- \to Zh$ with $Z \to l\bar{l}$ or $q\bar{q}$ and $h \to \tau\bar{\tau}$, if we assume $\sigma \sim 360$ fb (the cross section at $\sqrt{s} = 220$ GeV for m_h=110 GeV) , $\eta \sim 0.1$, and Br($h^0 \to \tau\bar{\tau}$) $\sim 7\%$. Therefore we can measure Br($h^0 \to \tau\bar{\tau}$) with a precision of 0.5%, which corresponds to an error of about 150 MeV (1σ) in the b-quark mass, which is largely free from theoretical ambiguities from the $b\bar{b}$ potential and the evaluation of the renormalization group equation in the low Q^2 region.

2.3 H^0, A^0, and $H^\pm$

2.3.1 Search Strategy

The direct evidence of the non-minimality of the Higgs sector expected in the SUSY models is the detection of one or more extra-Higgs bosons : H^0, A^0, and $H^\pm$. Their masses are functions of m_A and $\tan\beta$ as shown in Fig. 2.16. In the large m_A region, m_h approaches a constant value depending on $\tan\beta$, and the masses of H^0, A^0, and $H^\pm$ become degenerate. In the small m_A region, the masses of H^0 and $H^\pm$ are close to their minimums (in the tree level calculation, $m_{H^0} \to m_Z$ and $m_{H^\pm} \to m_W$) with little dependence on m_A.

These particles are produced in the processes: (1) $e^+e^- \to H^0Z^0$, (2) $e^+e^- \to H^0A^0$, (3) $e^+e^- \to h^0A^0$, and (4) $e^+e^- \to H^+H^-$. The cross sections of processes (1) and (3) are proportional to $\cos^2(\alpha-\beta)$ and that of (2) is proportional to $\sin^2(\alpha-\beta)$, where $\cos^2(\alpha-\beta)$ is large in the small m_A region while it is small in the large m_A region. The total cross section of process (4) does not depend on m_A nor $\tan\beta$ except for the phase space factor. Therefore, the non-minimal Higgs particles can be searched for using processes (1), (3), and (4) in the small m_A region and (2) and (4) in the large m_A region. The feasibility of searching for a charged Higgs with a relatively low mass ($m_{H^\pm} < 200$ GeV) is studied in ref.[40] and [41]. In the following subsections, studies of processes (1) and (2) are described.

2.3.2 $e^+e^- \to H^0Z^0$

The cross section of this process is large when m_A is small. In this parameter region, the decay mode of H^0 is mainly $b\bar{b}$ unless $H^0 \to h^0h^0$ is kinematically allowed in the small $\tan\beta$ region [34]. Therefore the search method discussed for the h^0 detection in the previous section can be applied.

It should be noted that in some parameter region with an intermediate $\sin^2(\alpha-\beta)$ value, we have a chance to discover simultaneously h^0 and H^0 at $\sqrt{s} = 300$ GeV. Such an example is shown in Fig.2.17 for m_h=100 GeV, $m_H = 120$ GeV, and $\sin^2(\beta-\alpha) = 0.33$.

At $\sqrt{s} = 300$ GeV we can thus discover "either h^0 or H^0" or "both h^0 and H^0", depending on the SUSY parameters.

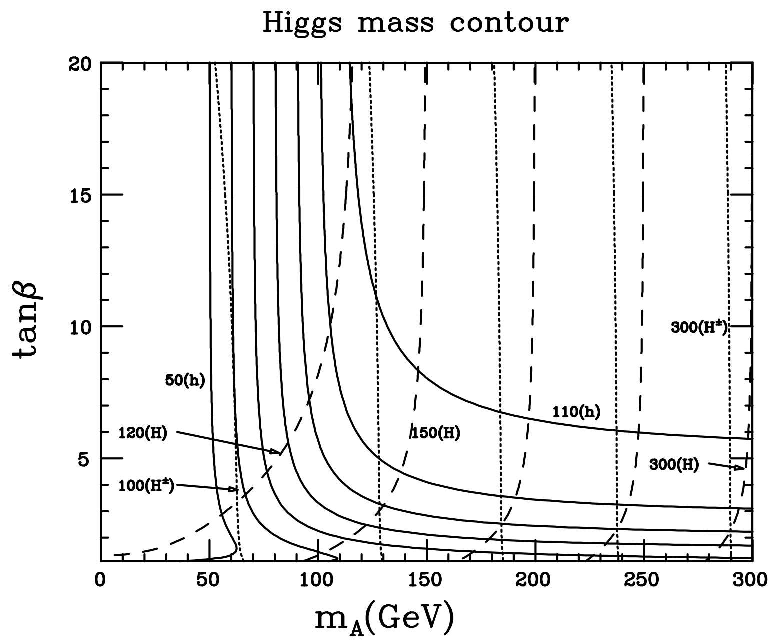

Figure 2.16: Higgs mass contours of h^0(solid), H^0(dashed), and $H^{\pm}$(dotted) in the m_A and $\tan\beta$ plane. The masses are 50, 60, 70, 80, 90, 100, and 110 GeV for h^0, 120, 150, 200, 250, and 300 GeV for H^0, and 100, 150, 200, 250, and 300 GeV for $H^{\pm}$. The used parameters are m_t = 150 GeV, $m_{\tilde{q}}$ = 1 TeV, and $A_t = A_b = \mu = 0$. For this parameter set, the maximum of m_h is 114.4 GeV and the maximums of m_H and $m_{H^{\pm}}$ are 144.5 and 83.7 GeV, respectively.

2.3.3 $e^+e^- \to H^0A^0$

In the large m_A region, the usable search modes for the non-minimal Higgs particles are $e^+e^- \to H^0A^0$ and $e^+e^- \to H^+H^-$ and the search region is limited by the collider energy. The total cross sections of $e^+e^- \to H^0A^0$ and $e^+e^- \to H^+H^-$ are shown in Fig. 2.18, for $m_A = 100, 150$, and 200 GeV, where m_H, $m_{H^{\pm}}$, and $\sin^2(\beta-\alpha)$ are calculated assuming $\tan\beta = 10$, $m_t = 150$ GeV, and $m_{\tilde{t}} = 1$ TeV. The cross sections are typically O(10) fb in the energy range $\sqrt{s} = 300 \sim 500$ GeV.

Here we present the result of a simulation performed for the H^0A^0 process at $\sqrt{s} = 500$ GeV with $\int Ldt = 100$ fb^{-1}, assuming $m_t = 150$ GeV, $\tan\beta = 10$, and $m_A = 200$ GeV. These parameters lead to $m_H = 201$ GeV and the coupling $\sin^2(\beta-\alpha) \sim 1$.

The dominant decay modes of H^0 and A^0 for this parameter set are $b\bar{b}$. We used the values $Br(H^0, A^0 \to b\bar{b}) = 0.92$ and $Br(H^0, A^0 \to \tau^+\tau^-) = 0.08$ in the simulation. With these decay branching ratios, the process $e^+e^- \to H^0A^0$ leads to the following three types of final states: (1) $e^+e^- \to$ 4jets ($\sim$ 84.6 %), (2) $e^+e^- \to \tau^+\tau^-$jet jet ($\sim$ 14.7 %), and (3) $e^+e^- \to \tau^+\tau^-\tau^+\tau^-$ ($\sim$ 0.6 %).

Here we concentrate on the first type. Although this is the dominant one, its signal must be extracted from the large background of $e^+e^- \to t\bar{t}$ due to the heavy top mass. The background from other processes is negligible. The second type, which is more distinctive against the background, may be used if the production rate is sufficient for discovery. A simulation study of the search for the second type of final state can be found elsewhere [42]. The third type is the cleanest, but the production rate is too small.

To select 4-jet events, cuts are first made on visible energy (> 75 % of $\sqrt{s}$), momentum

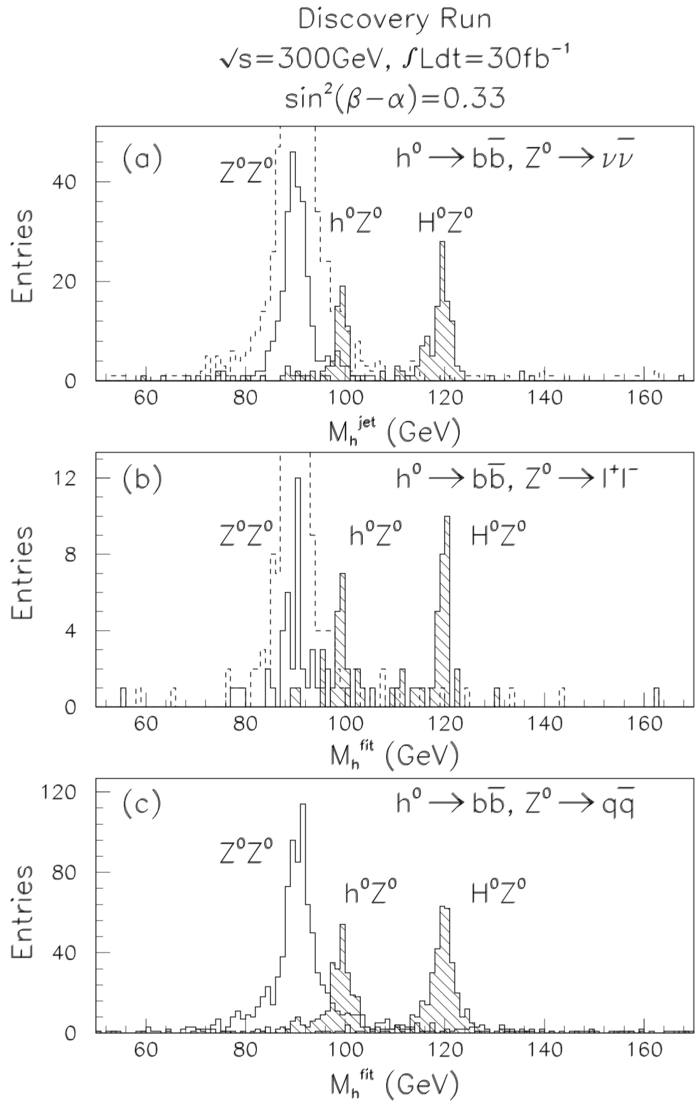

Figure 2.17: The reconstructed mass distributions for the three decay modes after the Discovery Run of $\int Ldt$=30 fb^{-1}. (a) The m_h^{jet} distribution for $h^0/H^0 \to b\bar{b}$ and $Z^0 \to \nu\bar{\nu}$. (b) The m_h^{fit} distribution for $h^0/H^0 \to b\bar{b}$ and $Z^0 \to \ell^+\ell^-$. (c) The m_h^{fit} distribution for $h^0/H^0 \to b\bar{b}$ and $Z^0 \to q\bar{q}$. In the figures, the hatched histograms are for the signal processes $e^+e^- \to h^0Z^0$ and $e^+e^- \to H^0Z^0$ with $m_h = 100$ GeV, $m_H = 120$ GeV, and $\sin^2(\beta - \alpha) = 0.33$. The blank histograms are for the background process $e^+e^- \to Z^0Z^0$. The dashed histograms in figures (a) and (b) are for the background process $e^+e^- \to Z^0Z^0$ without b-tagging.

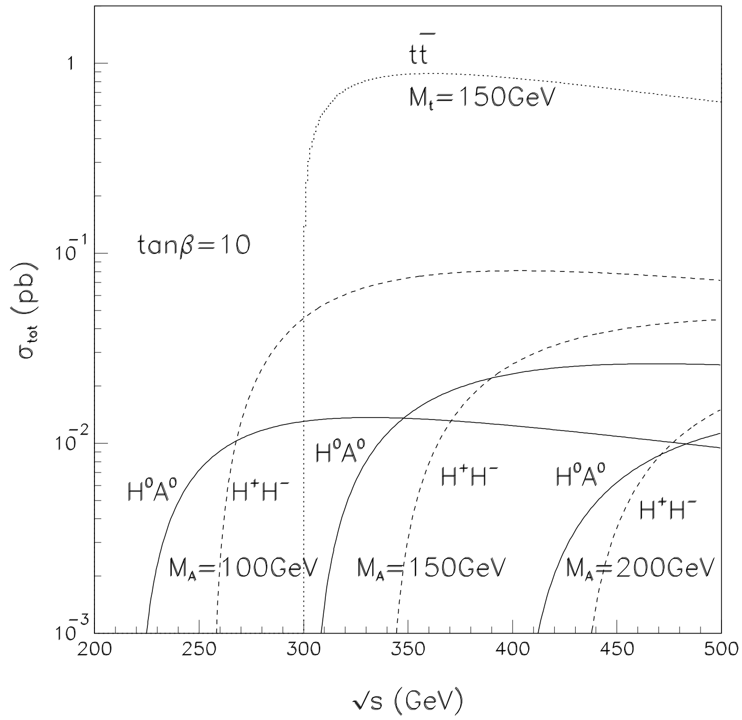

Figure 2.18: The total cross sections for the reactions $e^+e^- \to H^0A^0$ (solid curves) and $e^+e^- \to H^+H^-$ (dashed curves) for m_A = 100, 150, and 200 GeV, assuming $\tan\beta = 10$, $m_t = 150$ GeV, and $m_{\tilde{t}} = 1$ TeV. The dotted curve shows the cross section of the background process $e^+e^- \to t\bar{t}$.

balance ($<$ 20%), thrust axis ($|\cos\theta_{thrust}| < 0.7$), and thrust value ($< 0.75$). A jet finding algorithm optimized for 200 GeV Higgs is then applied and further cuts are made on the number of jets (=4), charged multiplicity in each jet (> 3) and the lepton energy in each jet ($<$ 20 % of the jet energy). The remaining events are fed to a kinematical fit assuming a four-body final state with a photon radiated from the initial state. The final cut is made on the goodness of the fit. Among the combinations of jets of the selected events, the one which minimizes $|M_{ij} - M_{kl}|$ (the difference of the invariant masses of two jet-pairs) is taken, as the mass difference of H^0 and A^0 is small.

The lego plots of the two invariant masses are shown in Fig. 2.19, both for the signal (H^0A^0) and the background ($t\bar{t}$). The plot peaks at (200 GeV, 200 GeV) for the signal, while the background does not peak anywhere. We can thus discover H^0 and A^0 with masses up to ~200 GeV at JLC-I of $\sqrt{s} = 500$ GeV, although it is difficult to distinguish H^0 from A^0.

2.3.4 SUSY Scale from m_{H^0} and m_{A^0} Measurement

Due to the radiative correction, the masses of Higgs particles are related to the SUSY scale. Fig. 2.20 shows contours of m_{h^0} in the plane of scalar quark mass and $\tan\beta$, for m_t=150 GeV, and m_A=160 GeV, when the Higgsino mass term and trilinear couplings are set to zero. As seen in the figure, $m_{\tilde{q}}$ is determined by m_{h^0} if $\tan\beta$ is large ($\gtrsim 7$).

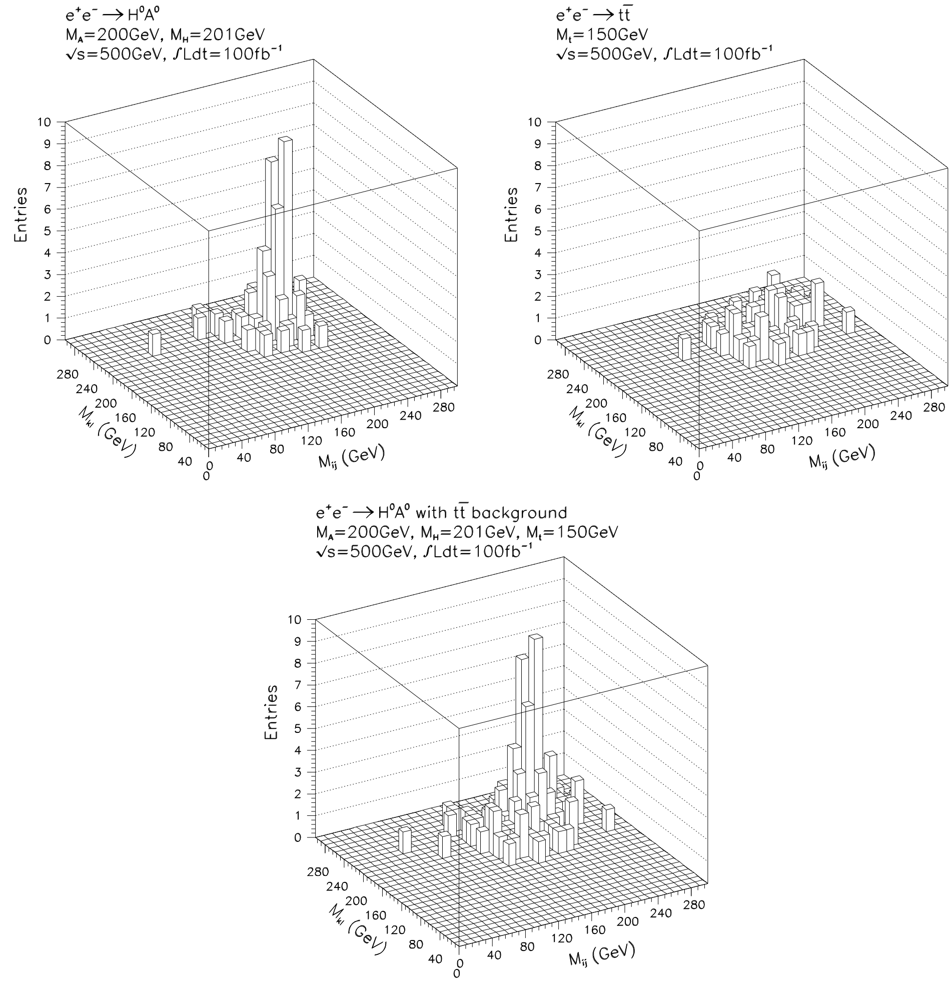

Figure 2.19: The lego plots of the reconstructed masses of the two jet pairs, at $\sqrt{s} = 500$ GeV with $\int Ldt$ 100 fb^{-1}. (a) The lego plot for the signal process $e^+e^- \to H^0A^0$ with $m_A = 200$ GeV and $m_H = 201$ GeV. (b) The lego plot for the background process $e^+e^- \to t\bar{t}$ with $m_t = 150$ GeV. (c) The sum of (a) and (b).

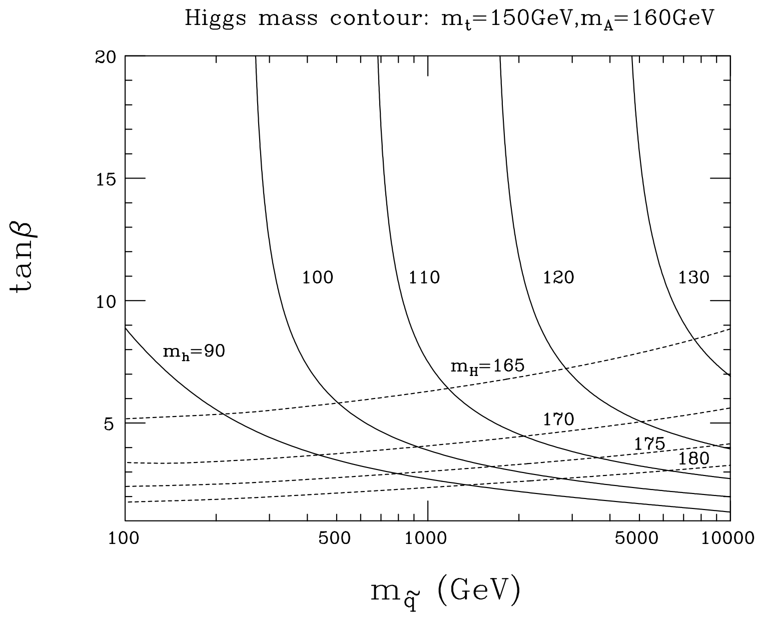

Figure 2.20: The contours of the masses of h^0(Solid) and H^0(dashed) in the plane of $m_{\tilde{q}}$ and $\tan\beta$.

2.4 SUSY Particles

Supersymmetry predicts the existence of a light neutral Higgs boson whose discovery at JLC is easy, as described in the previous sections. However the discovery of the lightest neutral Higgs boson alone is not enough to prove the supersymmetry. It is definitely necessary to discover *at least* one supersymmetric particle. We have emphasized that there are a lot of chances to discover at least one SUSY particle at JLC-I[43]. Although which is the first to be discovered is model-dependent, the SUSY search methods to be invoked at JLC-I is largely model-independent and, once we find one SUSY particle, it will tell us where to look for the next. Moreover, the mass determinations of the SUSY particles can be carried out model-independently, thereby allowing us to test model assumptions. It should be also noted that the polarized electron beam will play an essential role, in the course of the SUSY searches and studies.

2.4.1 Model Assumptions

We will work within the framework of supergravity (SUGRA) models with the "GUT-condition"s. These models involve, in general, the following parameters: (m_0, M_2, μ, $\tan\beta$), which determine the mass spectra and the interactions of supersymmetric particles[44]. μ is the higgsino mixing mass parameter and $\tan\beta$ is the ratio of the two vacuum expectation values of two Higgs doublets. m_0 is the scalar mass parameter, which is common to all the scalar particles in the case of supergravity models (the hidden sector SUSY breaking). M_2 is the $SU(2)$ gaugino mass parameter, which is related to the $SU(3)$ and $U(1)$ gaugino mass parameters:

$$\frac{M_1}{\frac{5}{3}\alpha/\cos^2\theta_W} = \frac{M_2}{\alpha/\sin^2\theta_W} = \frac{M_3}{\alpha_s}$$

under the GUT conditions. As demonstrated later, these SUGRA-GUT assumptions can be tested to a high precision.

In order to avoid unnecessary complications, we will make the following simplifying assumptions: a) the R-parity is exactly conserved which implies that SUSY particles can only be pair-produced and the lightest SUSY particle (LSP) is absolutely stable and b) the LSP is the lightest neutralino to be consistent with cosmology. In addition, we further assume that c) the supersymmetric particle in question is the lightest charged SUSY particle, unless otherwise stated.

As we will see below, assumption (c) ensures a reasonable branching fraction for direct decays into the LSP[45]. Therefore, the signal for SUSY particle productions is a missing transverse momentum or a large acoplanarity. Since colored SUSY particles are heavier than uncolored ones in general (see Figs. 2.21-a) and -b) which show the lighter chargino mass contours in the μ-M_2 plane and sfermion mass contours in the m_0-M_2 plane, respectively), we will focus our attention on chargino and slepton pair productions. In any case, it is usually straightforward to discover these SUSY particles at JLC-I, once their thresholds are crossed. Moreover, we will be able to study their properties in detail. It should be emphasized that detailed studies of the first SUSY particle alone can teach us a lot about the model parameters and will guide us to the discovery of the next.

2.4.2 Charginos

Generality of the Lighter Chargino Properties

First, we discuss the case where the chargino is the first SUSY particle to be discovered at JLC-I. The charginos $\chi_1^\pm$, $\chi_2^\pm$ are the mixtures of charged wino $\tilde{W}^\pm$ and charged higgsino $\tilde{H}^\pm$ obtained from the diagonalization of the mass matrix

$$\mathcal{L}_{\rm mass} = (\tilde{W}^+ \;\; \tilde{H}^+) \begin{pmatrix} M_2 & \sqrt{2} m_W \cos\beta \\ \sqrt{2} m_W \sin\beta & \mu \end{pmatrix} \begin{pmatrix} \tilde{W}^- \\ \tilde{H}^- \end{pmatrix}.$$

Notice that this mass matrix is given in terms of the three SUSY parameters: (M_2, μ, $\tan\beta$) of which M_2 and μ mainly control the mixing between weak eigenstates. When the splitting between M_2 and μ is large, the mixing is small and pure states, charged wino and higgsino, essentially become mass eigenstates. Our target chargino, the lighter of the two, is either the charged wino or the charged higgsino, depending on whether $M_2 \ll \mu$ or $M_2 \gg \mu$. If M_2 and μ are comparable, there is a substantial mixing between these two states and the properties of the lighter chargino share those of the charged wino and the charged higgsino. It is thus a good idea to start our discussion with the pure states, since, by doing so, we can gain intuitions into a more general case with substantial mixing.

i) Wino

When the lighter chargino state $\chi_1^\pm$ is almost a pure wino state, then the LSP is also almost a pure bino state. The charged wino, being the super partner of the W boson, does not directly couples to binos, while it couples to a left-handed fermion-sfermion pair. By our assumption, $\tilde{W}$ is lighter than all the sfermions, therefore, the decay of a wino $\tilde{W}$ into a bino $\tilde{B}$ proceeds only through a virtual sfermion exchange:

$$\tilde{W}^+ \to f_u \bar{\tilde{f}}_{d_L}^{\,*} \to f_u \tilde{B} \bar{f}_d,$$

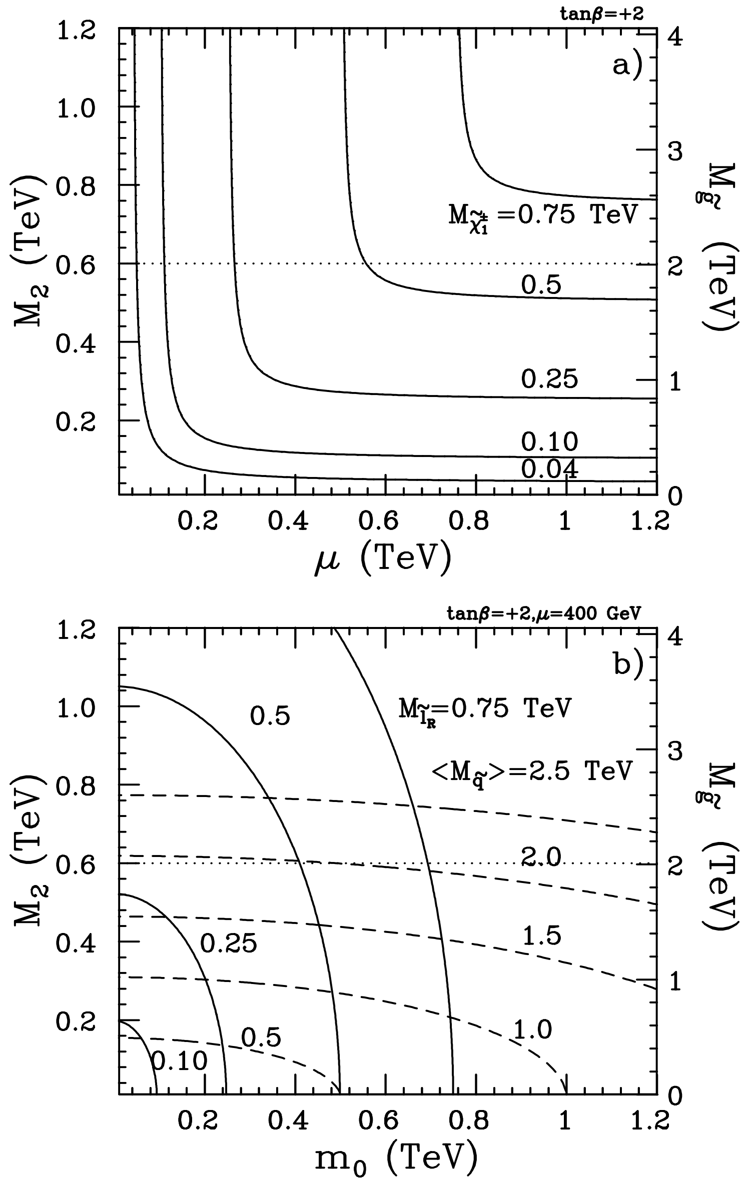

Figure 2.21: (a) Lighter chargino mass contours in the plane of the $SU(2)$ gaugino mass M_2 and the higgsino mixing mass μ for $\tan\beta \equiv v_2/v_1 = +2$. The right vertical axis is the corresponding gluino mass. Dotted line is the expected sensitivity limit for SSC and LHC. (b) Scalar fermion mass contours in the plane of M_2 and the common scalar mass m_0 for $\tan\beta = +2$ and $\mu = 400$ GeV. Solid lines are for scalar leptons and dashed lines for scalar quarks. Again the dotted line represents the expected sensitivity limit for SSC and LHC.

or

$$\tilde{W}^+ \to \tilde{f}^*_{uL} \bar{f}_d \to f_u \tilde{B} \bar{f}_d,$$

where f_u and f_d denote up-type and down-type fermions, respectively.

ii) Higgsino or Mixtures

When the lighter chargino state is dominated by the higgsino component, so is the LSP. The lighter chargino and the LSP are then almost mass-degenerate. This time, there exits a $\tilde{h}^+\tilde{h}^0W$ vertex which allows a direct decay to the LSP:

$$\tilde{h}^+ \to \tilde{h}^0 W^{(*)+} \to \tilde{h}^0 f_u \bar{f}_d.$$

The decay into a fermion and a virtual sfermion is suppressed in general, since the corresponding vertex originates from Yukawa interactions. By the same token, the t-channel sneutrino exchange diagram, active in the wino case, is negligible in this case.

The only exception is the decay into a b-quark and a virtual stop which subsequently decays into a top and the LSP. Of course, this requires a sufficiently large mass difference between the LSP and the lighter chargino. The large mass splitting, in turn, implies a substantial mixing which requires a light gaugino, since the mass splitting can be only of the order of $O(m_Z^2/(m_{\tilde{B}} - m_{\tilde{h}}))$.

In order to quantify the qualitative discussions presented above, we will examine below the production and decay of the lighter chargino($\tilde{\chi}_1^\pm$) more closely.

Chargino Production

Fig. 2.22 shows the contours of the lighter chargino pair production cross section at $\sqrt{s} =$ 500 GeV in the μ-M_2 plane. The comparison of this figure with Fig. 2.21-a) tells us that

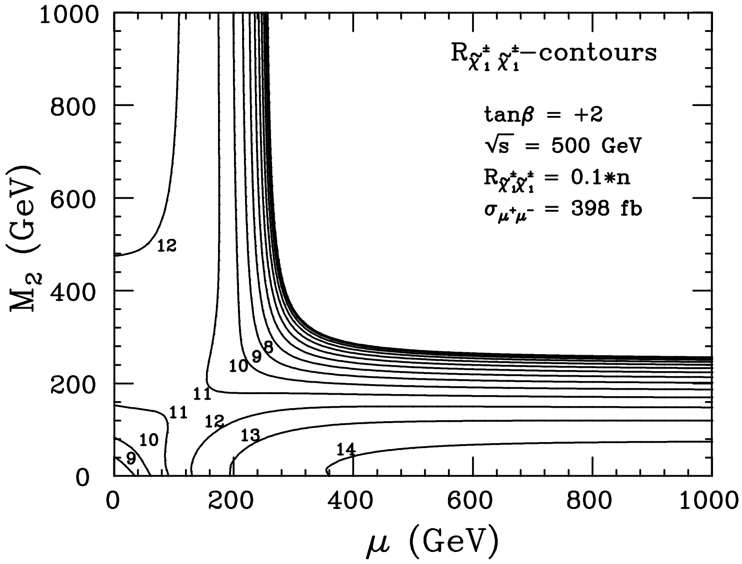

Figure 2.22: Cross section contours in the μ-M_2 plane for the lighter chargino pair productions. The cross sections are expressed in terms of the R-ratio and are calculated with $m_{\tilde{\nu}} = 500$ GeV and $\tan\beta = +2$.

the cross section is large enough everywhere above the threshold, even though the parameter dependence is rather large. Fig. 2.23-a) compares the $\sqrt{s}$ dependence of the production cross section for the following three typical cases: pure winos, equal mixtures of wino and higgsino, and pure higgsinos when the sneutrino mass is kept constant at $m_{\tilde{\nu}} = 1000$ GeV. Notice that the s-channel diagram alone cannot provide any information on m_0, since the chargino mass and the chargino-gauge-boson vertices are completely specified by μ, M_2, and $\tan\beta$. The magnitude of the production cross section, thus, determines the mixing angle between the charged wino and the charged higgsino in this case. Fig. 2.23-b) is the same figure for $m_{\tilde{\nu}} = 250$ GeV, where we can see that the t-channel sneutrino exchange diagram modifies the threshold shape as well as its magnitude. In this way, for a relatively light m_0, the t-channel sneutrino exchange diagram provides a possibility to determine m_0 through cross section measurements.

Chargino Decay

Under our assumption that the lighter chargino is the lightest charged SUSY particle, $\tilde{\chi}_1^\pm$ becomes the next to the lightest SUSY particle. Here we note that, when $\Delta m \equiv M_{\tilde{\chi}_1^\pm} - M_{\tilde{\chi}_1^0} > M_W$, the direct decay to $\tilde{\chi}_1^0 W$ dominates, unless the higgsino component is negligible. Fig. 2.24 shows this mass difference in the μ-M_2 plane. If this two-body decay mode is kinematically forbidden, the general discussions presented above apply.

We first deal with the lighter chargino which is almost a pure wino state. The supergravity models predict that the lightest sfermions are either sleptons or stop. On the other hand, the discovery of wino at JLC-I implies $\tilde{W} < 250$ GeV. Therefore, if sleptons are the lightest sfermions, we expect that the lightest sleptons are right-handed ones $\tilde{e}_R$, $\tilde{\mu}_R$, $\tilde{\tau}_R$, which are essentially mass-degenerate. Left-handed charged sleptons $\tilde{e}_L$, $\tilde{\mu}_L$, $\tilde{\tau}_L$, and left-handed neutral ones $\tilde{\nu}_e$, $\tilde{\nu}_\mu$, $\tilde{\nu}_\tau$, are nearly mass-degenerate, though they are heavier than the right-handed ones by the contribution of the gaugino mass to the renormalization group equations for the slepton masses. Since the wino component couples only to left-handed states, the decay of the wino-rich chargino thus proceeds as

$$\tilde{\chi}_1^+ \to \nu_l \tilde{l}_L^{+*} \to \nu_l \tilde{\chi}_1^0 l^+,$$

or

$$\tilde{\chi}_1^+ \to \tilde{\nu}_{lL}^* l^+ \to \nu_l \tilde{\chi}_1^0 l^+,$$

where l can be any of e, μ, and τ. The pair-produced charginos $\tilde{\chi}_1^+\tilde{\chi}_1^-$ appear as acoplanar lepton-pair events, with remarkable universality between electron, muon, and tau events. Notice that, in this case, the decay into $q\bar{q}\tilde{\chi}_1^0$ is suppressed by the heavy squark mass appearing in the squark propagator and the smallness of the weak hypercharge relevant to the coupling to the LSP which is essentially a bino state.

If stop is the lightest sfermion, then wino-rich chargino decays in the chain

$$\tilde{\chi}_1^+ \to \bar{b}_l \tilde{t}_L^* \to \bar{b}_l \tilde{\chi}_1^0 t.$$

This decay leads to an eight-jet final state with a large missing transverse momentum, which should be easy to detect.

When the lighter chargino has a sizable higgsino component, its decay is dominated by a "beta-decay", since the above mentioned $f\tilde{f}^*$ modes are strongly suppressed by the sfermion propagator, in the case where the sfermions are heavier than the lighter chargino and thus are much heavier than the W boson. This time, the decay into $q\bar{q}\tilde{\chi}_1^0$ becomes the major decay mode (67 %), while keeping a reasonable branching fraction for the leptonic mode, thereby allowing us to distinguish between the two cases.

When the $t\bar{b}\tilde{\chi}_1^0$ final state is open, the branching fraction to this mode may be large. The signature is the same as that of the light stop case for the wino-rich chargino.

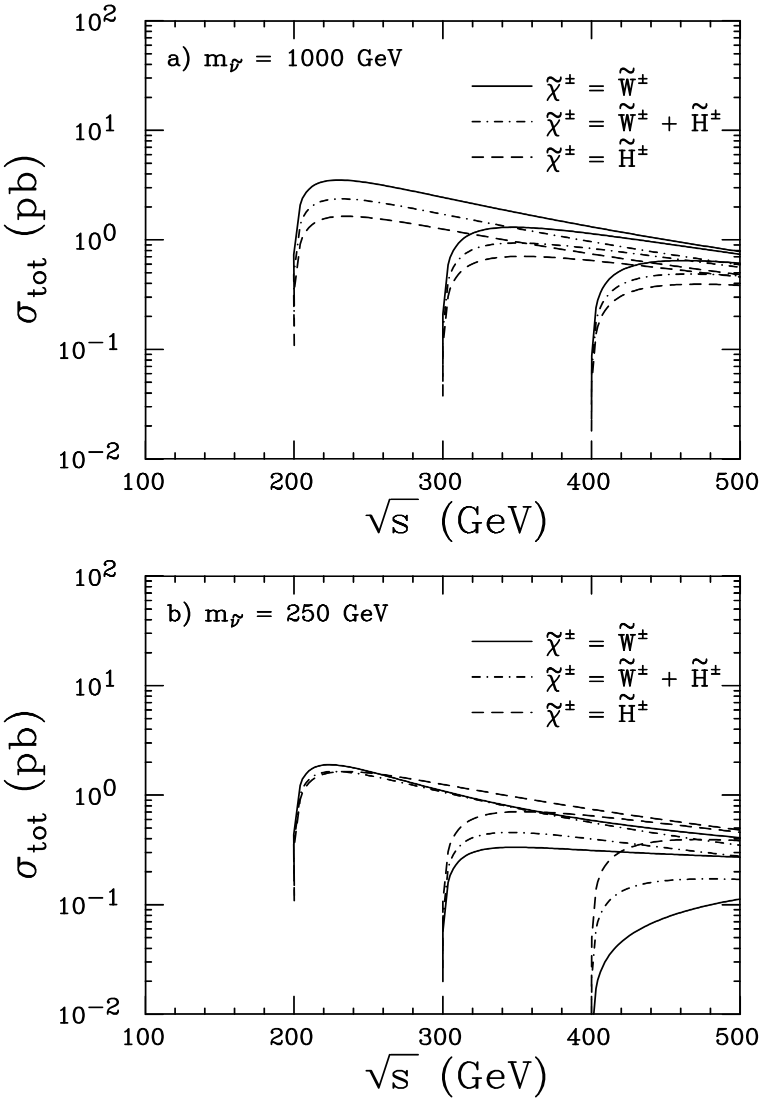

Figure 2.23: The total cross section for the pair production of the lighter charginos of $M_{\tilde{\chi}^{\pm}} =$, 100, 150, and 200 GeV as a function of $\sqrt{s}$ when (a) $m_{\tilde{\nu}} = 1000$ GeV and (b) $m_{\tilde{\nu}} = 250$ GeV. The solid, the dot-dashed, and the dashed curves correspond to pure winos, equal mixtures of wino and higgsino, and pure higgsinos, respectively.

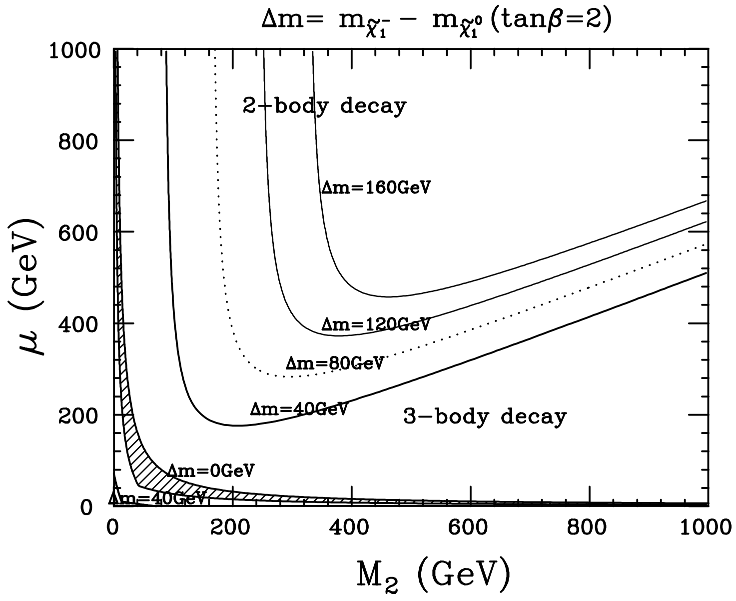

Figure 2.24: Mass difference contours in the μ-M_2 plane for the lighter chargino in the case of $\tan\beta = +2$. The shaded region is excluded by our assumption that the LSP is the lightest neutralino.

Chargino Search

Notice that in the parameter space of our interest: $m_0 \gtrsim 200$ GeV, $\mu \lesssim 1$ TeV, and $M_2 \lesssim 200$ GeV, the branching ratio for the hadronic mode always exceeds ~ 50 %, even if the lighter chargino is wino-rich. On the other hand, the branching ratio for the leptonic mode is at least 33 % which increases with the fraction of the wino component.

When the decay into a real $W(\tilde\chi_1^- \rightarrow \tilde\chi_1^0 W^-)$ is kinematically allowed, the best signal is an acoplanar pair of W's reconstructed from a four-jet final state, since the potentially most serious background from $e^+e^- \rightarrow W^+W^-$ is absent and the remaining background from $e^+e^- \rightarrow W^+W^-Z$ has only a small cross section. In this case, the detection of the chargino is straightforward.

In the following, therefore, we will focus our attention on the case where the two-body decay is kinematically forbidden. Considering the background from W-pair productions and two-photon processes, the best channel, in this case, is again the four-jet mode. However, we will try to use the final state where one of the chargino decays hadronically: $\tilde\chi_1^- \rightarrow q\bar{q}\tilde\chi_1^0$, while the other decays leptonically: $\tilde\chi_1^- \rightarrow l^-\bar\nu\tilde\chi_1^0$, since the combinatorial ambiguity is absent in this mode and, therefore, the determinations of the chargino and the LSP masses are easy.

Notice that the background from W-pair productions can be effectively removed by requiring that the invariant mass of the two-jet system and that of the lepton and the reconstructed neutrino are inconsistent with the W-pair hypothesis, while the two-photon processes can be eliminated by requiring an energetic isolated lepton. The remaining W-pair contamination can be further reduced by cuts on the polar angles of the isolated lepton and the two-jet system and a cut on the acoplanarity.

The signature to look for is then two jets and a single energetic isolated lepton with a large missing transverse momentum or a large acoplanarity, for which the W-pair hypothesis is disfavored, provided that the mass difference $\Delta m \equiv M_{\tilde\chi_1^\pm} - M_{\tilde\chi_1^0}$ is sufficiently large to produce the energetic isolated lepton. As already shown in Fig. 2.24, this mass difference is large enough

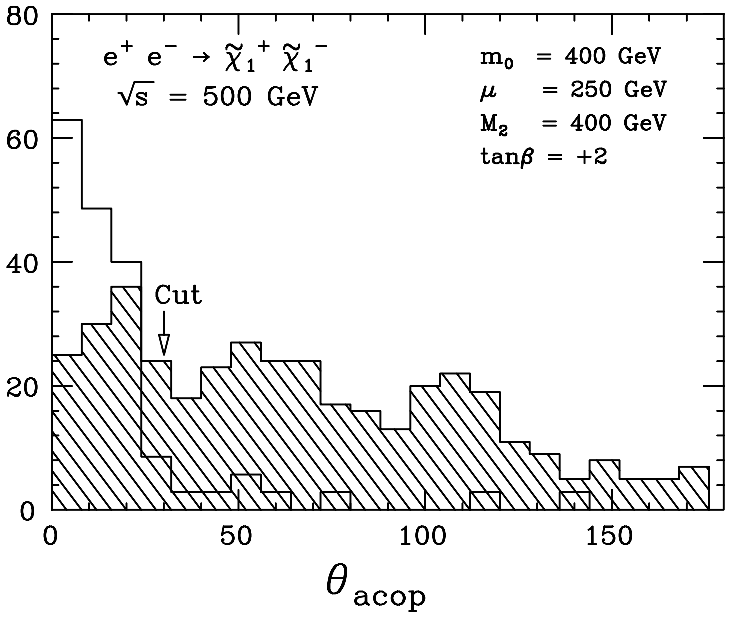

Figure 2.25: An example of the acoplanarity distribution for the two-jet+lepton final states from the lighter chargino pair productions in the case of $m_0 = 400$ GeV, $M_2 = 400$ GeV, $\mu = 250$ GeV, and $\tan\beta = +2$. The Monte Carlo data correspond to an integrated luminosity of 10 fb^{-1} at $\sqrt{s} = 500$ GeV. The hatched histogram is the signal events, while the open histogram is the background from W-pair productions.

for detection in most of the parameter space. The remaining question is whether this is large enough for the separation from the potential background processes such as two-photon processes or W-pair productions.

Fig. 2.25 is an example of the acoplanarity distribution of the two-jet+lepton final states from the chargino decays for an integrated luminosity of 10 fb^{-1} (20 days) at $\sqrt{s} = 500$ GeV. Also shown is the W-pair background (open histogram). Both the signal and the background are with all the cuts except for the one on the acoplanarity. The cut at $\theta_{acop} = 30^o$ provides a virtually background-free sample of the chargino pairs with a reasonable efficiency $\epsilon \gtrsim 13$ %, including the branching fraction of 30 %.

Chargino Study

When the chargino signal is detected, the next task is the determination of the chargino and the LSP masses. For this, we look at the energy distribution of the two-jet systems from the chargino decays which is shown in Fig. 2.26. Notice that the distribution depends on the structure of the decay vertex. Nevertheless, the end points of the distribution are determined by the chargino and the LSP masses. Therefore the shape of the distribution may provide us with additional information on the SUSY parameters.

The expected statistical errors on $M_{\tilde{\chi}_1^\pm}$ and $M_{\tilde{\chi}_1^0}$ are 3.2 GeV and 2.0 GeV, respectively, when we fit the distribution to a polynomial.

The LSP mass together with the lighter chargino mass fixes two out of the three parameters (M_2, μ, and $\tan\beta$) in the chargino-neutralino mass matrices, leaving only one parameter undetermined. If the LSP is lighter than the observed chargino by a factor of $\alpha_W/(3/5)\alpha_Y$, then it strongly suggests that they are almost pure wino and bino states. The interactions of the particles are then completely fixed by the supersymmetry, which enables us to estimate

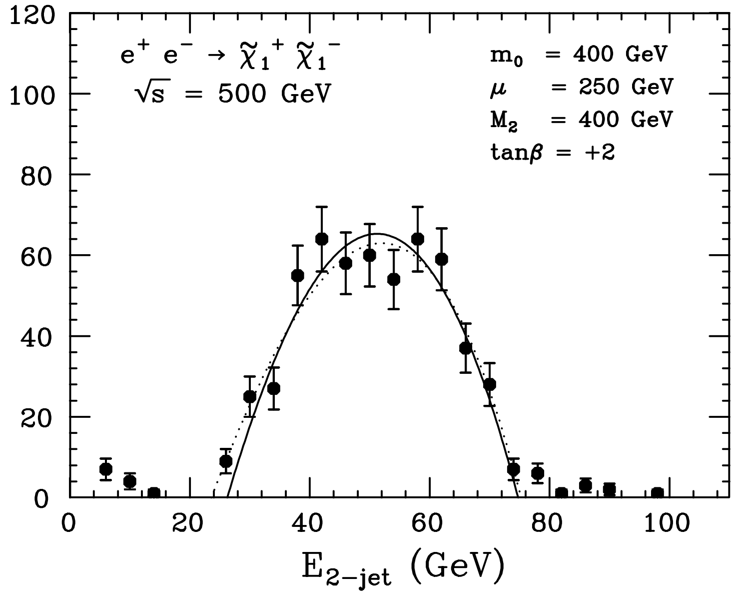

Figure 2.26: The energy distribution of the two-jet systems from the lighter chargino decays for Monte Carlo data corresponding to an integrated luminosity of 21 fb^{-1}, where the SUSY parameters are the same as with Fig. 2.25. The solid line corresponds to the input masses, while the dotted line is the best fit curve from a polynomial fit.

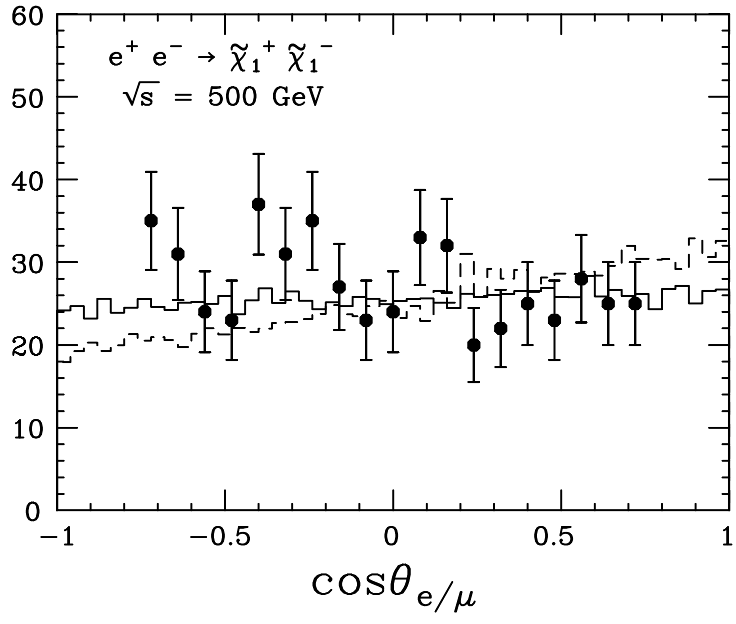

Figure 2.27: An example of the polar angle distribution for l^-'s from the lighter chargino decays compared with the theoretical predictions for different sets of the SUSY parameters: the solid histogram for $m_0 = 400$ GeV, $M_2 = 400$ GeV, $\mu = 250$ GeV, and $\tan\beta = +2$ and the dashed histogram for $m_0 = 400$ GeV, $M_2 = 250$ GeV, $\mu = 250$ GeV, and $\tan\beta = +2$. Notice that the vertical scale for the dashed histogram is arbitrarily adjusted to show the difference in the angular dependence. The Monte Carlo data corresponds to an integrated luminosity of 21 fb^{-1} and were generated with the same SUSY parameters as with the solid histogram.

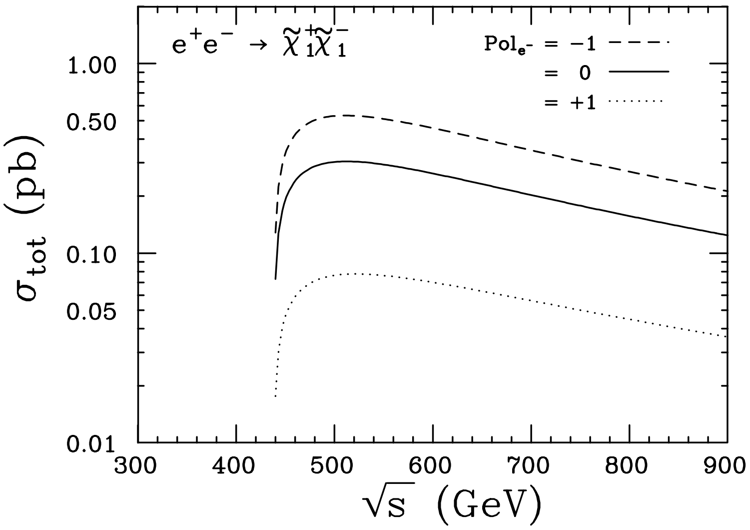

Figure 2.28: The polarization dependence of the chargino pair-production cross section for $m_0 = 400$ GeV, $M_2 = 400$ GeV, $\mu = 250$ GeV, and $\tan\beta = +2$, shown as a function of $\sqrt{s}$.

the cosmic abundance of the LSP. By requiring that their contribution to the cosmic density does not exceed the critical one, we will obtain an *upperbound* on the sfermion masses. For example, $m_{\tilde{B}} = 100$ GeV implies that $m_{\tilde{f}} < 350$ GeV for degenerate sleptons and squarks, and a stronger bound $m_{\tilde{l}} < 300$ GeV for $m_{\tilde{l}} \ll m_{\tilde{q}}$. On the other hand, if the mass ratio of the LSP and the chargino is different from $\alpha_W/(3/5)\alpha_Y$, it signals a substantial mixing with higgsino states, indicating a light higgsino. For instance, a 10% shift requires the higgsinos to be lighter than $\sim 10 m_{\tilde{\chi}^0}$.

The differential cross section gives us yet another handle to determine the SUSY parameters. Fig. 2.27 shows the corresponding polar angle distribution of the l^-'s from the $\tilde{\chi}_1^-$ decays which is compared with the theoretical predictions for different sets of the SUSY parameters. The polarized electron beam is also a powerful tool to study the nature of the chargino, since, for instance, we can switch off the t-channel sneutrino diagram by choosing a right-handed electron beam. The right-handed electron beam, at the same time, kills most of the contribution from the wino component, since the $\tilde{W}^+\tilde{W}^-Z$ and $\tilde{W}^+\tilde{W}^-\gamma$ vertices come from the $\tilde{W}^+\tilde{W}^-W^3$ vertex which vanishes for the right-handed beam in the massless Z limit. Therefore, the right-handed beam allows us to study the higgsino component separately. Fig. 2.28 shows the polarization dependence of the chargino pair-production cross section for $m_0 = 400$ GeV, $M_2 = 400$ GeV, $\mu = 250$ GeV, and $\tan\beta = +2$. The threshold shape is essentially controlled by the S-wave phase space factor β^1, indicating that the chargino in this case is higgsino-rich and the t-channel sneutrino exchange contribution is small.

Combining this information together with that from the SUSY Higgs studies, we can learn a lot about the SUSY parameters from a single charged SUSY particle by virtue of the cleanness of JLC experiments.

2.4.3 Sleptons

General Discussions on Sfermion Mass Spectrum

The discovery of sleptons at JLC-I allows us to thoroughly explore the supersymmetric mass spectrum. Studies on $\tilde{e}$, $\tilde{\mu}$, and $\tilde{\tau}$ can be carried out simultaneously, giving much useful information on gaugino and scalar masses, and even on μ and $\tan\beta$. This unique opportunity is provided by the following mass formulae:

$$\begin{aligned}
m_{\tilde{l}_L}^2 &= m_0^2 - \left(\frac{3}{2}(\alpha_2^2-\alpha_0^2)+\frac{1}{22}(\alpha_1^2-\alpha_0^2)\right)\frac{M_2^2}{\alpha_2^2} - \frac{1}{2}m_Z^2\cos 2\beta(1-2\sin^2\theta_W), \\
m_{\tilde{\nu}_L}^2 &= m_0^2 - \left(\frac{3}{2}(\alpha_2^2-\alpha_0^2)+\frac{1}{22}(\alpha_1^2-\alpha_0^2)\right)\frac{M_2^2}{\alpha_2^2} - \frac{1}{2}m_Z^2\cos 2\beta, \\
m_{\tilde{l}_R}^2 &= m_0^2 - \frac{2}{11}(\alpha_1^2-\alpha_0^2)\frac{M_2^2}{\alpha_2^2} - m_Z^2\cos 2\beta\sin^2\theta_W. \qquad (2.2)
\end{aligned}$$

By virtue of an accidental cancellation, the mass splitting between $\tilde{l}_L$ and $\tilde{l}_R$ uniquely determines the wino mass parameter M_2 and puts a tight constraint on the universal scalar mass m_0 and $\tan\beta$. These mass formulae also ensure that masses of all the sleptons are close to each other, with slight differences among the four groups: (1) ($\tilde{e}_L$, $\tilde{\mu}_L$), (2) ($\tilde{e}_R$, $\tilde{\mu}_R$), (3) $\tilde{\tau}_1$, (4) $\tilde{\tau}_2$. The right-handed ones (2) are always lighter than the left-handed ones (1), whose splitting "measures" the gaugino mass. Anyway, if one of these sleptons is found, the chance to discover the others is greatly enhanced.

Slepton Production

Smu- and stau-pair productions take place through e^+e^- annihilations into a virtual photon or Z and their differential cross sections behave as $\sin^2\theta$. Their total cross sections are completely specified by their quantum numbers. The contours of the cross sections for smu and stau pairs at $\sqrt{s} = 500$ GeV are plotted in Fig. 2.29 in the m_0-M_2 plane. Notice that the contours resemble those in Fig. 2.21-b), indicating that sensitivity limit extends up close to the production threshold.

Selectron pair production is more complicated since there exist t-channel neutralino exchange diagrams which depend strongly on the masses and couplings of the neutralinos. Fig. 2.30 is similar to Fig. 2.29 for selectron pair productions. The existence of the t-channel diagrams also modifies the angular distribution. Fig. 2.31 is an example of the differential cross sections for selectron pair productions.

Slepton Decay

Since the production cross sections for slepton pairs are of reasonable size, if they are produced at all, their detection should be easy when the direct decays into the LSP dominate and the mass difference between the target slepton and the LSP is large. This condition is satisfied when the LSP has a sizable component of the bino state. Figs. 2.32-a) and -b) show the branching fractions for the direct decays for super partners of left-handed and right-handed muons, respectively, in the m_0-M_2 plane. The figures indicate that the direct mode indeed dominates the $\tilde{\mu}_R$ decays. Figs. 2.33-a) and -b) are the corresponding contours for the mass differences. Almost everywhere in the parameter space, the mass differences are large enough for detection. In this case, the signal of slepton pair productions is again an acoplanar lepton-pair, similar to the wino-pair events. However, the two-body decay of sleptons gives a flat energy distribution for the final state leptons, which can be easily separated from the three-body decay of a charged wino. At the threshold of sleptons, the final state leptons are almost monochromatic. Furthermore, due to the difference in the threshold behavior of the total cross sections, β^3 for sleptons and β for winos, we are able to distinguish the former from the latter. If the LSP is higgsino-like, then the sleptons may decay in a completely different manner:

$$\tilde{l} \to l\tilde{w}^{0*} \to l\tilde{h}^0 h^0.$$

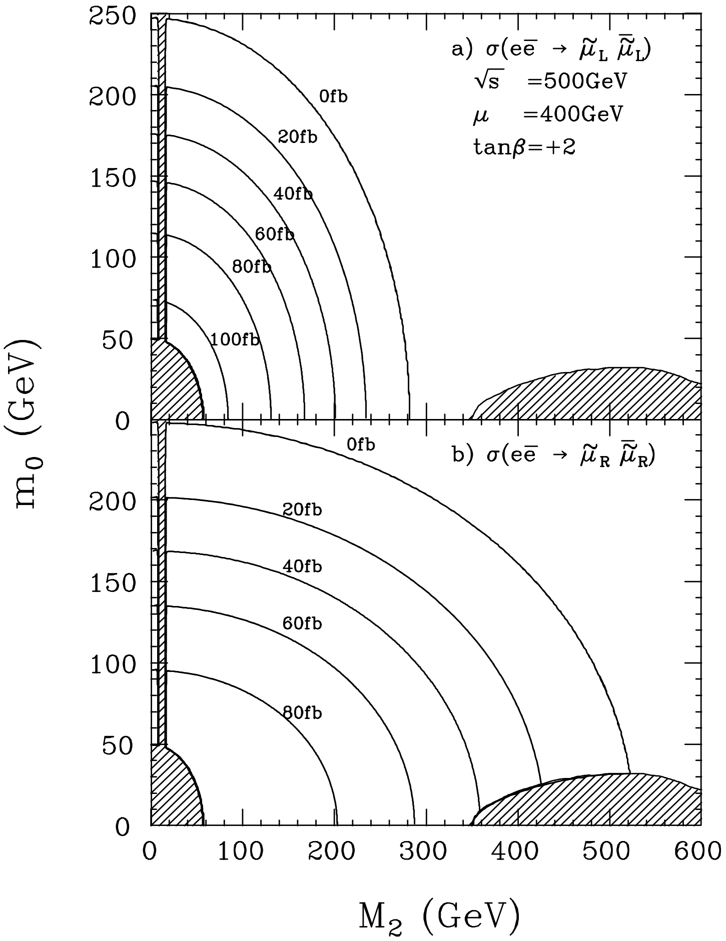

Figure 2.29: Cross section contours for slepton ($\tilde{l} \neq \tilde{e}$) pair productions in the m_0-M_2 plane, in the case of $\mu = 400$ GeV and $\tan\beta = +2$ and $\sqrt{s} = 500$ GeV: (a) $e^+e^- \to \tilde{\mu}_L^+\tilde{\mu}_L^-$ and (b) $e^+e^- \to \tilde{\mu}_R^+\tilde{\mu}_R^-$. The shaded regions are forbidden by our assumption that the LSP is the lightest neutralino.

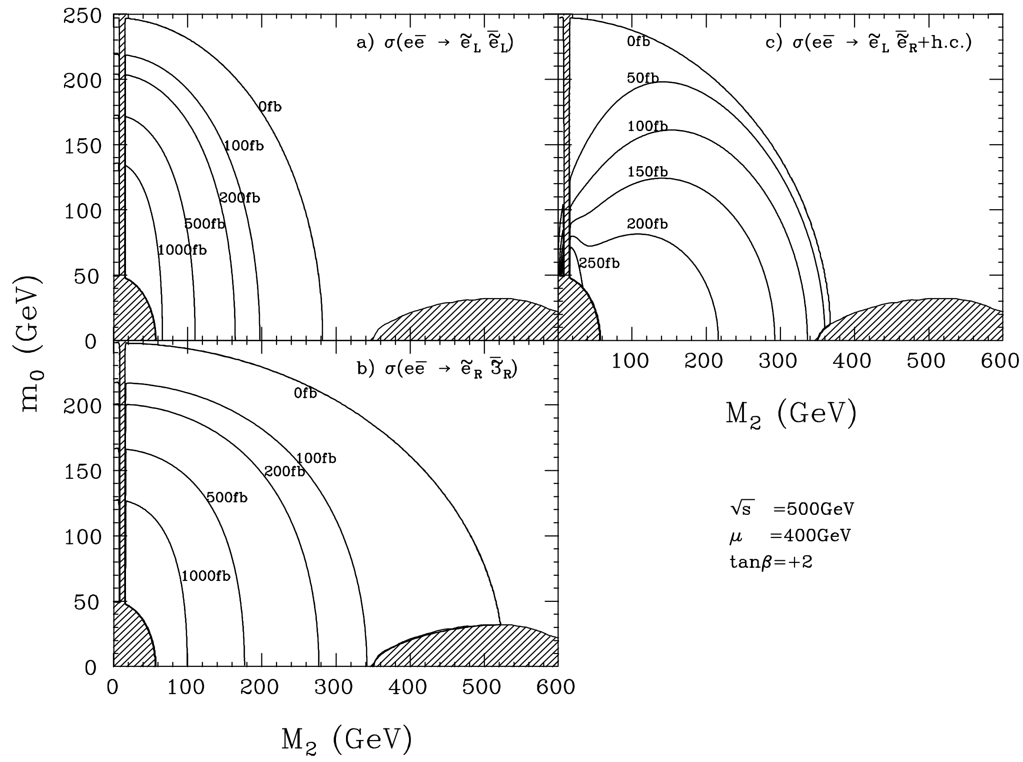

Figure 2.30: A similar plot to Fig. 2.29 for selectron pair productions: (a) $e^+e^- \to \tilde{e}_L^+\tilde{e}_L^-$, (b) $e^+e^- \to \tilde{e}_R^+\tilde{e}_R^-$, and (c) $e^+e^- \to \tilde{e}_L^+\tilde{e}_R^- + \tilde{e}_R^+\tilde{e}_L^-$.

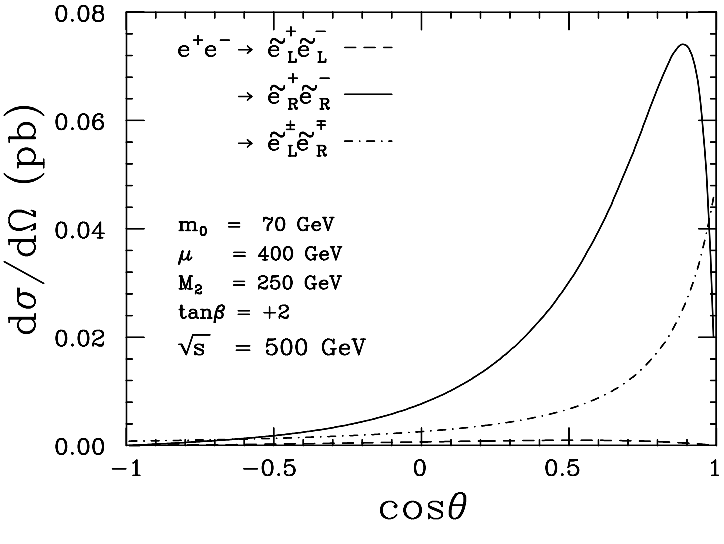

Figure 2.31: The differential cross sections for selectron pair productions in the case of $m_0 =$ 70 GeV, $M_2 = 250$ GeV, $\mu = 400$ GeV, and $\tan\beta = +2$. The three curves correspond to $e^+e^- \to \tilde{e}_L^+\tilde{e}_L^-$(dash), $e^+e^- \to \tilde{e}_R^+\tilde{e}_R^-$(solid), and $e^+e^- \to \tilde{e}_L^\pm\tilde{e}_R^\mp$(dot-dashed), respectively.

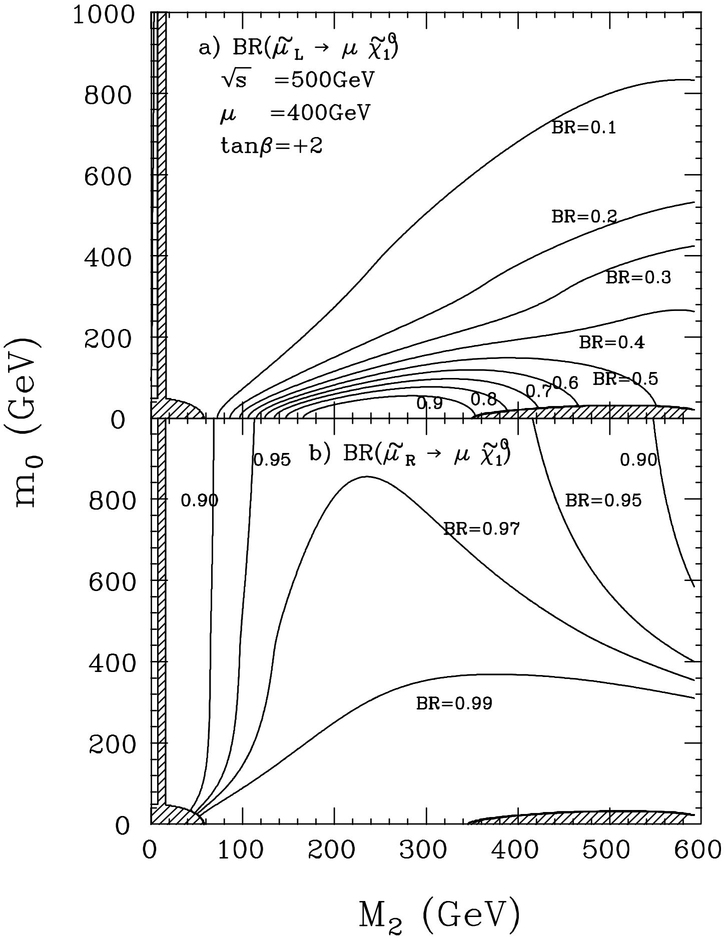

Figure 2.32: Branching fraction contours in the m_0-M_2 plane for (a) $\tilde{\mu}_L$ and (b) $\tilde{\mu}_R$ in the case of $\mu = 400$ GeV and $\tan\beta = +2$. The shaded regions are excluded by our assumption that the LSP is the lightest neutralino.

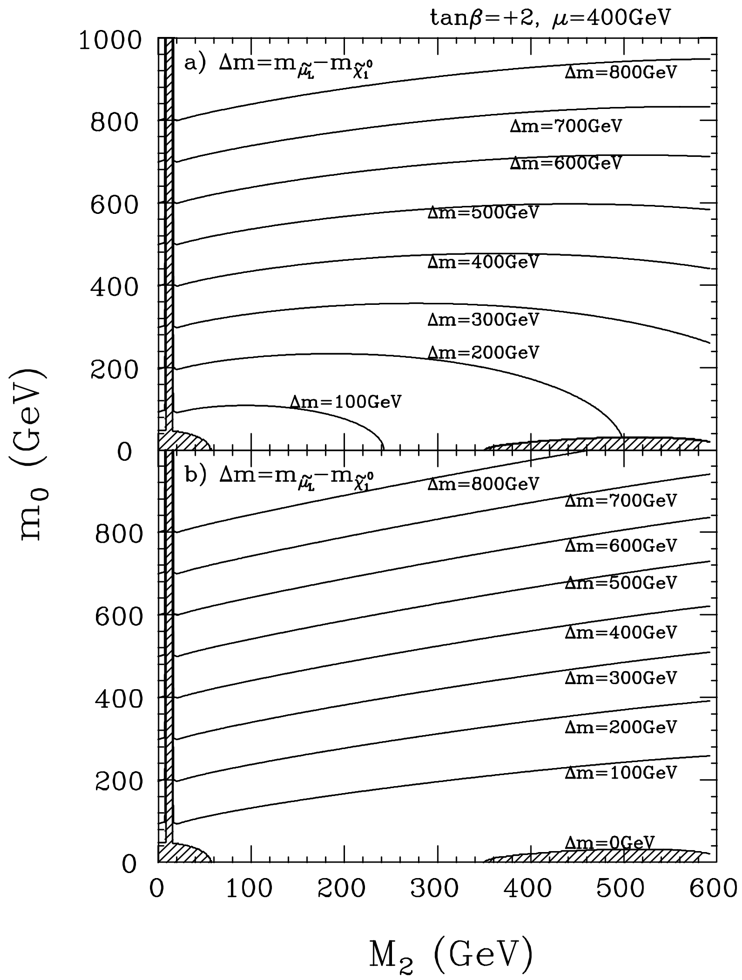

Figure 2.33: Mass difference contours in the m_0-M_2 plane for (a) $\tilde{\mu}_L$ and (b) $\tilde{\mu}_R$ in the case of $\mu = 400$ GeV and $\tan\beta = +2$.

This decay results in a spectacular event consisting of a lepton-pair and four jets with an invariant mass peak at $m(jj) \sim m_h$. In this case, the absence of the t-channel higgsino exchange amplitude provides a good proof that the LSP is indeed higgsino-like. Since the detection of this decay mode is straightforward, we will concentrate on the case of a bino-like LSP below.

Slepton Search

Figs. 2.34-a) and -b) are examples of acoplanarity distributions for selectron and smuon pair productions, respectively, after the accumulation of 10 fb^{-1} (20 days) at $\sqrt{s} = 350$ GeV. Notice that the SUSY parameters used here were so chosen that both $\tilde{l}_L^{\pm}$ and $\tilde{l}_R^{\pm}$ can be produced at $\sqrt{s} = 500$ GeV, while $m_{\tilde{l}_R^{\pm}} < M_{\tilde{\chi}_1^{\pm}}$ to be consistent with our assumption. We can see that the signals can be effectively enhanced over the background mainly consisting of W pairs, by applying a cut on the acoplanarity angle. A detection efficiency of $\epsilon \gtrsim 50$ % is easily achieved with a signal to background ratio of $S/B \gtrsim 1.6$ even for smuons. The signal to background ratio can be further improved by using a right-handed electron beam, since the production cross section for smuon pairs almost doubles, while the W-pair cross section essentially vanishes, as shown in fig. 2.34-c).

Slepton Study

Once a slepton is discovered, we can determine the masses of the slepton and the LSP from the energy spectrum of the final state leptons more reliably than in the chargino case, since we know the shape of the spectrum. Fig. 2.35-a) is the energy distribution of muons from smuon decays for an integrated luminosity of 18 fb^{-1} with a right-handed electron beam. Though the distribution is a little bit different from the expected rectangular shape due, primarily, to selection cuts, the lower and the higher edges are sharp enough. These end points of the energy spectrum determine $m_{\tilde{\mu}}$ and $M_{\tilde{\chi}_1^0}$. Fig. 2.35-b) shows the contours obtained from the fit to the Monte Carlo data. We can determine the smuon and the LSP masses with statistical errors of 1.4 GeV and 1.0 GeV, respectively.

If the LSP is bino-like, then its t-channel exchange also contributes to the selectron pair production. JLC's polarized electron beam will, again, play a crucial role here since the t-channel diagrams exist only for the selectron with the same chirality as the beam electron. Fig. 2.36 plots the production cross section of selectron pairs as a function of $\sqrt{s}$ for $\mathrm{Pol}_{e^-} = -1, 0$, and $+1$. Notice that the t-channel exchange contribution comes only from the bino-component in the cases of $\tilde{e}_R^+\tilde{e}_R^-$ and $\tilde{e}_L^{\pm}\tilde{e}_R^{\mp}$ productions. The $\tilde{e}_L^{\pm}\tilde{e}_R^{\mp}$ production is of particular interest, since there is no s-channel contribution, which allows an unambiguous test of the t-channel contribution. Thus detailed studies of the interference effects combined with the beam polarization measure the mass of the LSP exchanged in the t-channel *and* its coupling to the electron. We can check whether the LSP is indeed bino-like in this way. If we vary the energy and cross the threshold of $\tilde{e}_L^+\tilde{e}_L^-$ production, we may also be able to see the t-channel exchange of the second lightest neutralino, presumably the neutral component of wino.

Figs. 2.37-a) to -c) plot the differential cross sections for four different chirality combinations of the final state selectrons. We can see that the final state chirality combinations can be effectively selected by choosing an appropriate helicity of the electron beam. The magnitudes and the shape of the differential cross sections will tell us about the nature of the active neutralinos in the t channel.

We can play a similar game for smuon-pair productions. Fig. 2.38 is a similar plot to Fig. 2.36 for smuon pair productions. Since the cross section is completely specified by quantum numbers, the polarization dependence will confirm that the produced particles are actually smuons. When the mass splitting of $\tilde{\mu}_L$ and $\tilde{\mu}_R$ is small, however, the importance of the beam polarization increases, since it greatly helps us separate one from the other.

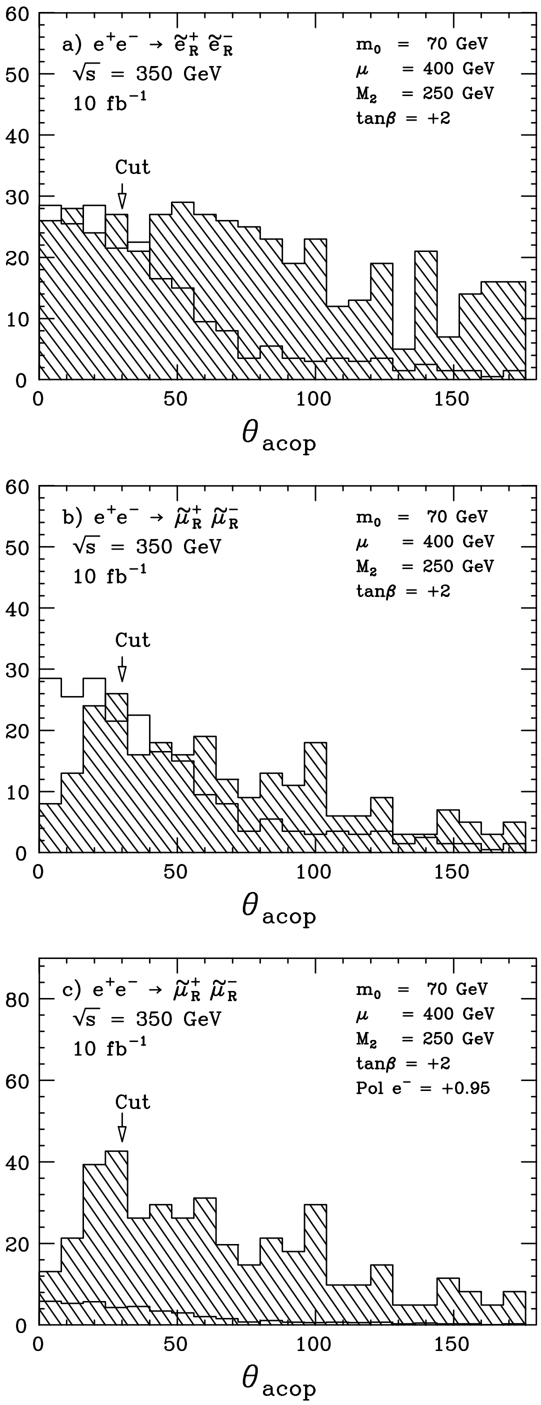

Figure 2.34: Examples of acoplanarity distributions for (a) selectron pair and (b) smuon pair productions. The Monte Carlo data correspond to an integrated luminosity of 10 fb^{-1} at $\sqrt{s} = 350$ GeV with an unpolarized electron beam. The hatched histograms are for the signal events, while the open histograms are the background from W^+W^- productions. The effect of the right-handed electron beam is demonstrated in (c).

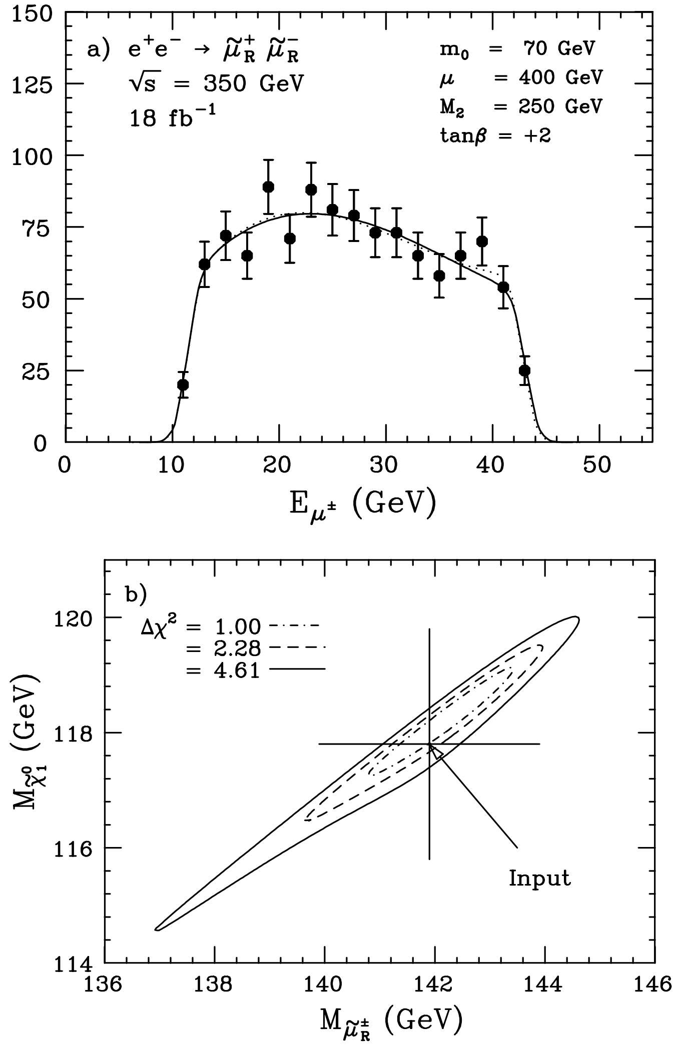

Figure 2.35: (a) The energy distribution of muons from smuon decays for the same Monte Carlo parameters as with Fig.2.34 but with a right-handed electron beam and with a doubled statistics. The solid line is the result of a fit to the Monte Carlo data with $m_{\tilde{\mu}}$ and $M_{\tilde{\chi}_1^0}$ fixed at their input values, while the doted line corresponds to the best fit curve, letting these two masses move freely. (b) The contours in the $m_{\tilde{\mu}}$-$M_{\tilde{\chi}_1^0}$ plane obtained from the fit to the energy distribution.

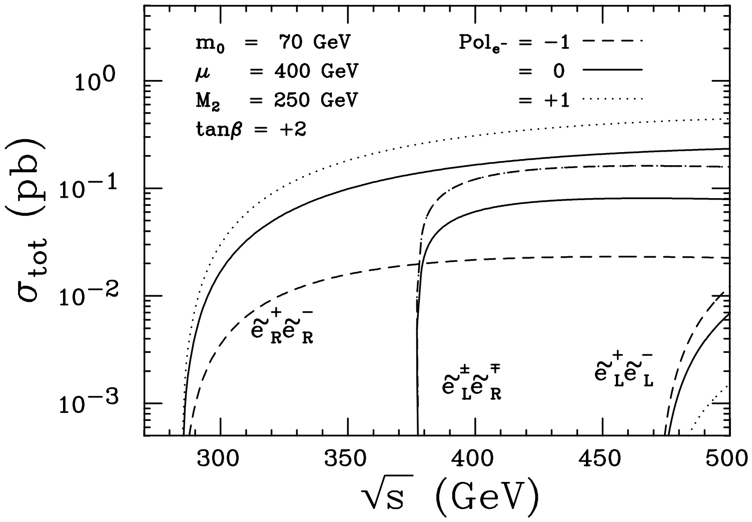

Figure 2.36: The electron polarization dependence of the selectron pair production cross section in the case of $m_0 = 70$ GeV, $M_2 = 250$ GeV, $\mu = 400$ GeV, and $\tan\beta = +2$. The solid lines are for no polarization, while the dashed and the dotted curves are for left-handed and right-handed electron beams, respectively. Notice that $\tilde{e}^\pm_L\tilde{e}^\mp_R$ production is forbidden when wrong polarization is selected.

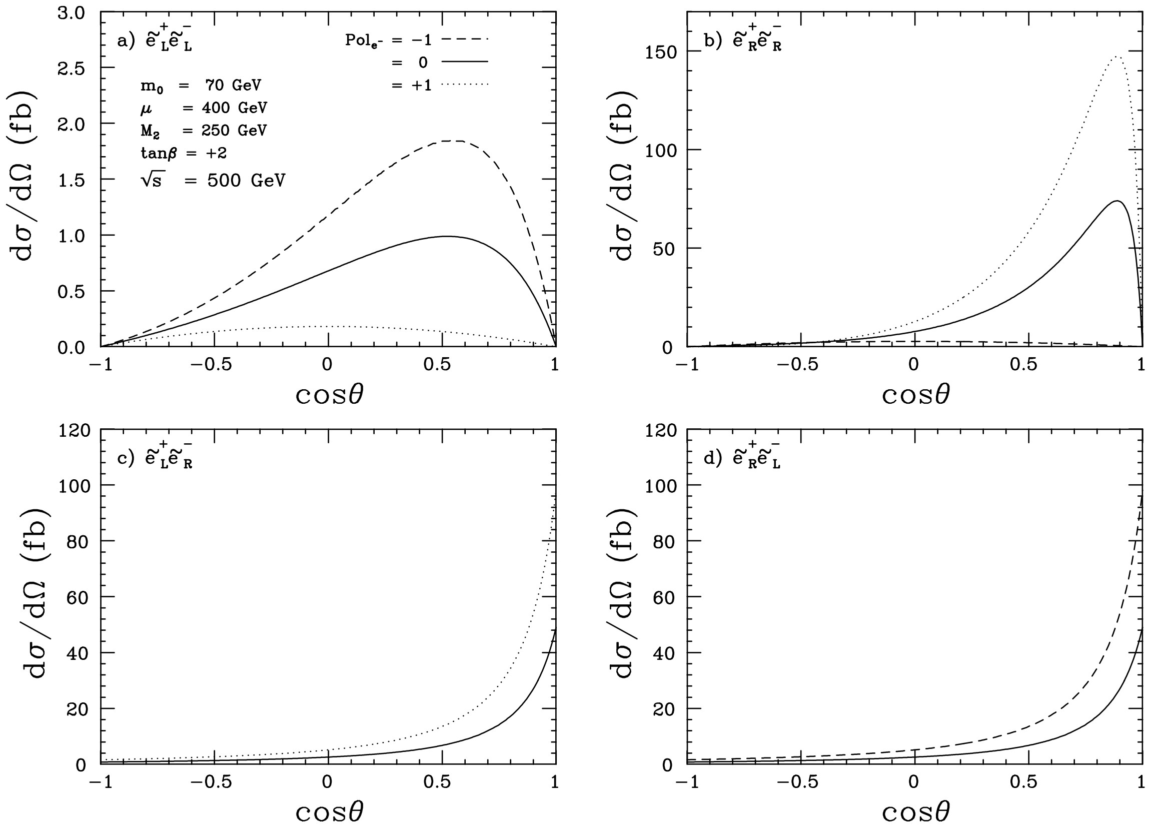

Figure 2.37: The differential cross sections for different chirality combinations for selectron pairs: (a) $\tilde{e}^+_L\tilde{e}^-_L$, (b) $\tilde{e}^+_R\tilde{e}^-_R$, (c) $\tilde{e}^+_L\tilde{e}^-_R$, and (d) $\tilde{e}^+_R\tilde{e}^-_L$.

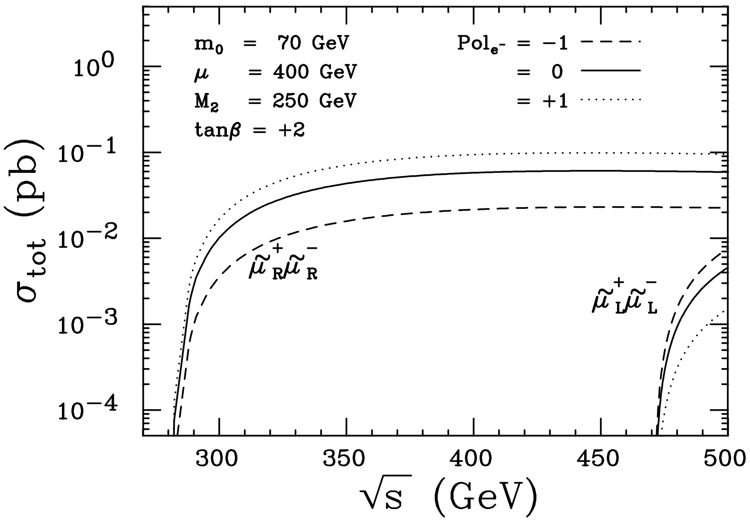

Figure 2.38: A similar plot to Fig. 2.36 for smuon pair productions.

Once the gaugino and the slepton masses are fixed in this way, then we can predict the gluino and squark masses and decide the next energy to go.

2.5 Tests of SUGRA-GUT Assumptions

As shown in the previous subsections, JLC-I can discover SUSY particles roughly to their kinematical limits, with a capability of detailed studies on their masses and decay distributions. We demonstrate in this subsection that this very capability enables us to test the SUSY-GUT and supergravity scenario. Once the lightest charged SUSY particle is found, it will serve us a great deal of information about the SUSY-particle spectrum, and we can set the c.m. energy for the next SUSY hunting. Then we will be able to find series of SUSY particles. The SUSY mass spectrum will put strong constraints on the supergravity parameters, especially on M_2 (universal gaugino mass) and m_0 (universal scalar mass). In a lucky situation, we will have opportunity to determine all the SUSY-breaking parameters in the minimal supergravity, (M_2, m_0, μ, $\tan\beta$, A, B). It is further possible to check whether the SUSY mass spectrum is indeed determined by this small number of parameters. In this way, we will explore physics at the Planck scale, since the nature of the SUSY-breaking mechanism is believed to come from the supergravity interactions.

We will demonstrate below an example of the SUSY-study strategy, for the case where the charged slepton is the first SUSY particle to be discovered. The supergravity models predict either right-handed charged slepton or chargino will be found first. The right-handed charged slepton masses are expected to be degenerate among generations.

The right-handed selectron $\tilde{e}_R$ has larger production cross section than smu $\tilde{\mu}_R$ or stau $\tilde{\tau}_R$ due to the t-channel bino $\tilde{B}$-exchange diagram. After first observations of highly acoplanar electron pair events, we will use the right-handed electron beam to suppress the background from W-pair production. Then the detection of all three right-handed charged sleptons ($\tilde{e}_R$, $\tilde{\mu}_R$, and $\tilde{\tau}_R$) is relatively easy as shown in the previous subsections. Using the energy distributions of final-state charged leptons, we can measure masses of sleptons and the LSP at the percent level. Already at this point, we can check one of the most important assumptions in the minimal

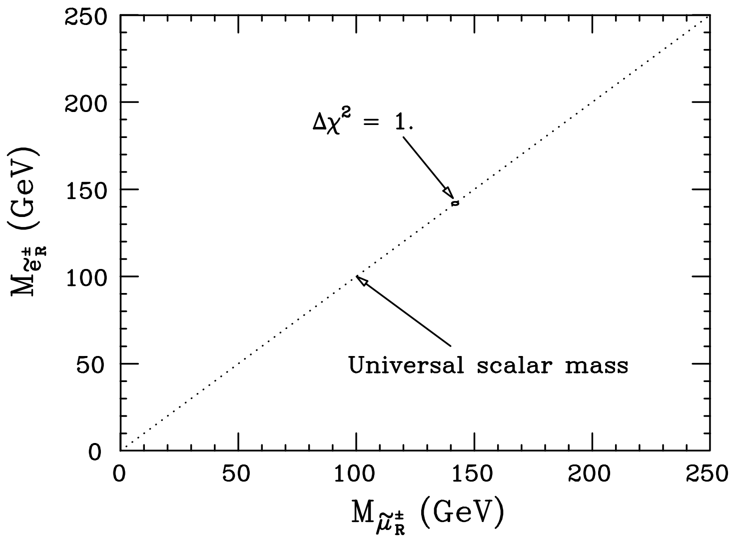

Figure 2.39: The expected $\Delta\chi^2 = 1$ contour in the $m_{\tilde{\mu}_R}$-$m_{\tilde{e}_R}$ plane. The hidden sector SUSY breaking implies the generation-independence of the right-handed slepton masses.

supergravity, that the scalar masses are degenerate among generations. The universality of the masses of $\tilde{e}_R$, $\tilde{\mu}_R$, and $\tilde{\tau}_R$ will strongly support the hidden-sector scenario of SUSY-breaking (see Fig. 2.39).

The selectron production is enhanced by the t-channel $\tilde{B}$-exchange diagram compared to the smu and stau productions which have only s-channel γ- and Z-exchange contributions. Thus the selectron production cross section essentially measures the bino mass M_1. Since the LSP mass $m_{\rm LSP}$ is already fixed, one can test whether the LSP is bino-like or higgsino-like. If the cross section is consistent with the t-channel exchange of the LSP, then it is almost a pure bino. If the cross section is almost the same with that of smus or staus, then the LSP is almost a pure higgsino. In the mixed case, the mass of the LSP and the cross section put two constraints on the neutralino-chargino mass parameters (M_2, μ, $\tan\beta$). In any case, it is remarkable that we can set an upperbound on the mass of the lighter chargino from $m_{\rm LSP}$ alone. Fig. 2.40 shows the upper limit on the lighter chargino mass as a function of the LSP mass. For the LSP mass greater than 30 GeV, the lighter chargino mass never exceeds twice the LSP mass. For a higgsino-like LSP, the lighter chargino (almost a pure charged higgsino) lies just above the LSP. For a bino-like LSP, the lighter chargino (almost a pure charged wino) is roughly twice as heavy as the LSP.

From the upperbound on the lighter chargino mass obtained from $m_{\rm LSP}$, we will fix the c.m. energy for the chargino search. We have shown that the lighter chargino mainly decays into LSP+W, whose detection is easy. Even in a small region of the parameter space where it decays into three-body final states, we can discover the chargino as far as it is heavier than the LSP by $\Delta m \gtrsim O(5)$ GeV. We can measure its mass $m_{\tilde{\chi}^\pm}$, and its production cross sections both for right-handed electron beam $\sigma_R(\tilde{\chi}^\pm)$ and left-handed beam $\sigma_L(\tilde{\chi}^\pm)$. Combining $m_{\rm LSP}$, $m_{\tilde{\chi}^\pm}$, and $\sigma_R(\tilde{\chi}^\pm)$, it is possible to fix all the three parameters of the neutralino-chargino sector (M_2, μ, $\tan\beta$), assuming the GUT-condition $M_1/M_2 = \alpha_1/\alpha_2$, if the gaugino-higgsino mixing is large (*i.e.*, $M_2 \simeq \mu$). In this case, the mass of the heavier chargino can be predicted, and should lie near above the lighter one. Its discovery at the predicted mass will confirm the GUT-condition here assumed. In our example case of $M_2 < \mu$, the lighter chargino is almost a

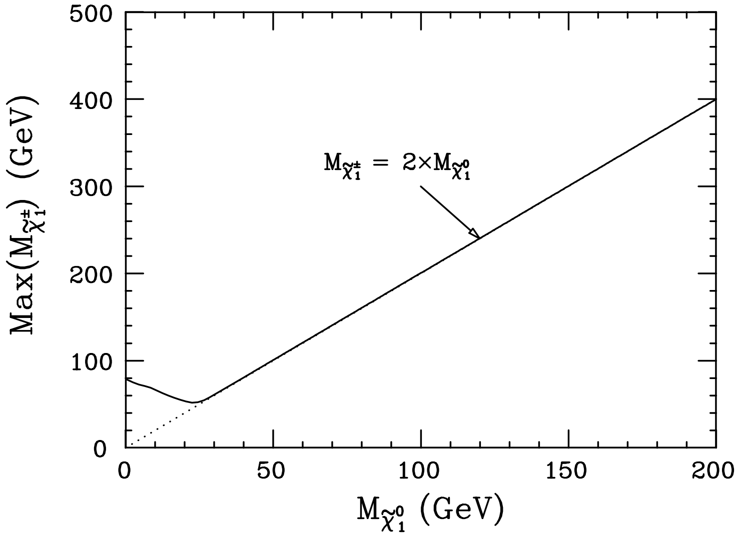

Figure 2.40: The upper limit on the lighter chargino mass as a function of the LSP mass.

pure charged wino. Then it is not easy to fix μ and $\tan\beta$. However even in this case, we can test the GUT-condition. The bino mass M_1 is roughly $m_{\rm LSP}$, and the wino mass M_2 is roughly the chargino mass $m_{\tilde{\chi}^\pm}$. Fig. 2.41 shows the $\Delta\chi^2 = 1$ contour in the (M_1, M_2) plane, which clearly demonstrates the possibility of a precision test of the SUSY-GUT assumption.

There is another information we can obtain from the study of the lighter chargino. The cross section from the left-handed electron beam $\sigma_L(\tilde{\chi}^\pm)$ carries the contribution from the t-channel sneutrino $(\tilde{\nu}_L)$ exchange. The dependence of σ_L on $m_{\tilde{\nu}_L}$ is shown in Fig. 2.42.

Note that $m_{\tilde{\nu}_L}$ is related to the mass of the left-handed charged slepton $m_{\tilde{l}_L}$ in a model-independent way,

$$m^2_{\tilde{\nu}_L} \leq m^2_{\tilde{l}_L} = m^2_{\tilde{\nu}_L} + (1-\sin^2\theta_W)m_Z^2|\cos(2\beta)| \leq m^2_{\tilde{\nu}_L} + (1-\sin^2\theta_W)m_Z^2, \tag{2.3}$$

for $\tan\beta \geq 1$. This observation will fix the next c.m. energy to go.

The left-handed charged slepton will be searched first in the process $e^-_R e^+ \to \tilde{e}^-_R \tilde{e}^+_L$, from the t-channel bino-exchange. The discovery of the left-handed selectron at the predicted mass confirms the SUSY-nature of the sleptons. If lucky, it is even possible to determine $\tan\beta$ from the above formula. The important implication of the measured $m_{\tilde{l}_L}$ is that we can check the universal scalar mass hypothesis in the hidden-sector scenario of the SUSY-breaking. The SUSY-GUT alone predicts

$$\begin{aligned} m^2_{\tilde{l}_L} &= m_5^2 - \left(\frac{3}{2}(\alpha_2^2-\alpha_0^2) + \frac{1}{22}(\alpha_1^2-\alpha_0^2)\right)\frac{M_2^2}{\alpha_2^2} - \frac{1}{2}m_Z^2\cos 2\beta(1-2\sin^2\theta_W), && (2.4)\\ m^2_{\tilde{\nu}_L} &= m_5^2 - \left(\frac{3}{2}(\alpha_2^2-\alpha_0^2) + \frac{1}{22}(\alpha_1^2-\alpha_0^2)\right)\frac{M_2^2}{\alpha_2^2} - \frac{1}{2}m_Z^2\cos 2\beta, && (2.5)\\ m^2_{\tilde{l}_R} &= m_{10}^2 - \frac{2}{11}(\alpha_1^2-\alpha_0^2)\frac{M_2^2}{\alpha_2^2} - m_Z^2\cos 2\beta\sin^2\theta_W, && (2.6) \end{aligned}$$

where m_5 and m_{10} are masses common for the **5**- and **10**-dimensional representations. The universal scalar hypothesis suggests $m_5 \simeq m_{10}$. Then the difference between left-handed and

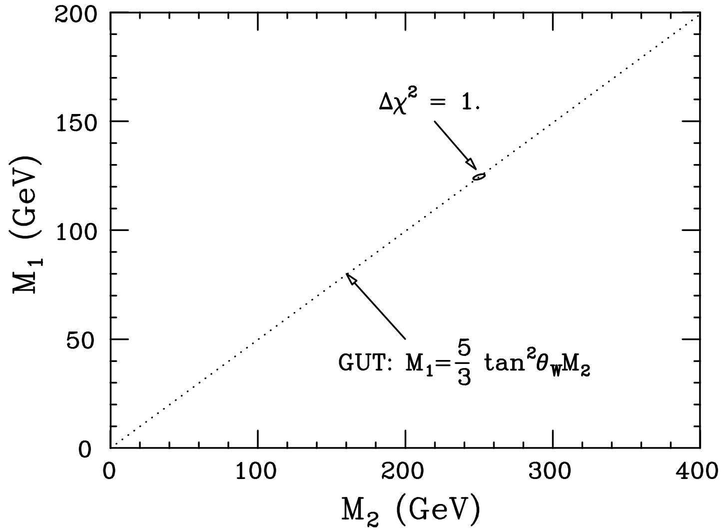

Figure 2.41: The expected $\Delta\chi^2 = 1$ contour in the M_2-M_1 plane. The dotted line shows the expectation from the SUSY-GUT condition.

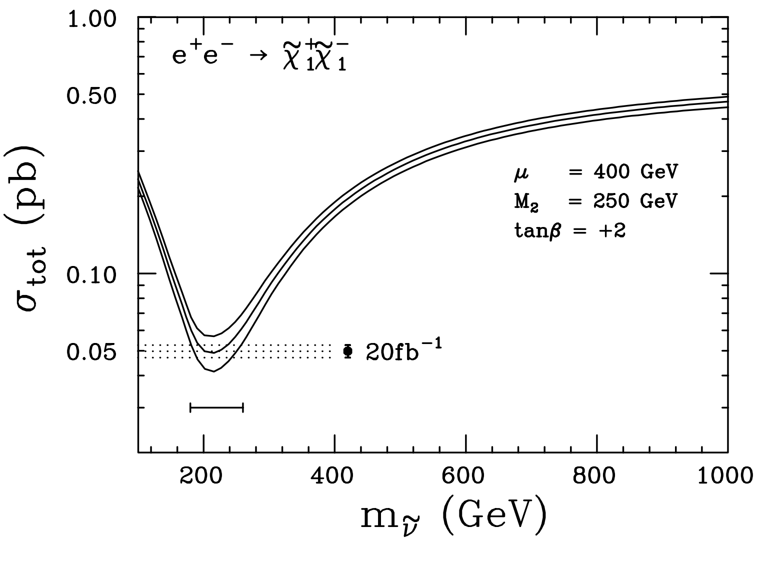

Figure 2.42: The lighter chargino pair production cross section as a function of the sneutrino mass. The three curves represent the ambiguity (1-σ) from the chargino mass determination.

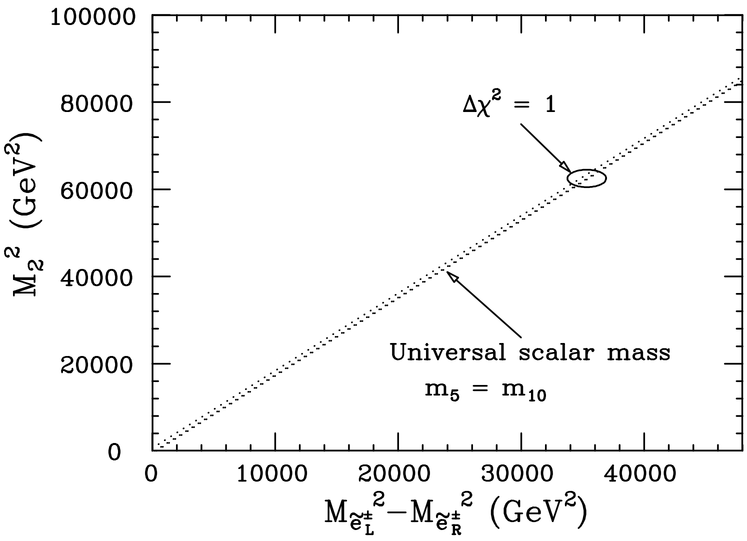

Figure 2.43: The expected $\Delta\chi^2 = 1$ contour in the plane of the squared mass difference of the left-handed and right-handed selectrons versus M_2^2. The doted lines represent the universal scalar mass hypothesis for $\tan\beta = 0, +2, +30$.

right-handed charged slepton masses is determined solely by the gaugino mass

$$m_{\tilde{l}_L}^2 - m_{\tilde{l}_R}^2 \simeq \left(\frac{3}{2}(\alpha_0^2 - \alpha_2^2) - \frac{5}{22}(\alpha_0^2 - \alpha_1^2)\right)\frac{M_2^2}{\alpha_2^2}. \tag{2.7}$$

The expected $\Delta\chi^2 = 1$ contour in the plane $m_{\tilde{l}_L}^2 - m_{\tilde{l}_R}^2$ versus M_2^2 is shown in Fig. 2.43, with the prediction of the universal scalar mass hypothesis. Thus the measurement of $m_{\tilde{l}_L}$ will put a strong constraint on the supergravity model building.

Finally, the discovery of other left-handed charged sleptons $\tilde{\mu}_L$ and $\tilde{\tau}_L$ will again put constraints on the hidden-sector scenario of SUSY-breaking which predicts the mass degeneracy among generations. Furthermore, the t-channel neutral wino ($\tilde{W}^0$) exchange diagram exists for the $\tilde{e}_L$-pair production from the left-handed electron beam, which serves as a cross-check of the measured SUSY parameters.

Though we have concentrated on the case where the right-handed charged slepton is the first to be discovered at JLC-I, the strategy is similar to the case where the lighter chargino is the first. The study of the chargino will determine the three parameters of the neutrino-chargino sector, and also the sneutrino mass can be measured from $\sigma_L(\tilde{\chi}^\pm)$. Then we obtain upperbound on $m_{\tilde{l}_L}$, and the same analysis as above can be carried out.

2.6 Top

Since we all know that top must exist and is no heavier than 200 GeV, top physics is guaranteed for JLC-I[46]. The top quark we are going to deal with has many unique features, compared to quarks of other flavors. This is primarily due to its large mass and width. We will examine below some of the new features, which will manifest themselves in the course of detailed top studies.

2.6.1 Measurements of Top Mass and $\alpha_s(M_Z)$

Here, we will start with the measurement of the top mass. There are two ways to determine the top mass: the first by threshold scan and the other by the invariant mass measurement of the 3-jet system from top decays.

Threshold Scan

For the threshold scan, there is one very important difference from the charm and bottom cases: a heavy top quark has a large width dominated by $t \to bW^+$ decays. The large width allows a $t\bar{t}$ system to form only a limited number of onium states. At first glance, this seems rather disappointing but, to the contrary, turns out to be advantageous in many ways. First remember that the continuation of multiple resonances to the continuum region has always been a troublesome process in the traditional onium spectroscopy, since the intermediate region suffers from nonperturbative and, therefore, uncontrollable theoretical ambiguities. These ambiguities are absent from the $t\bar{t}$ system because the large width acts like an infrared cutoff and prevents the non-perturbative part of the potential from affecting the threshold calculation. This implies that the cross section in the whole threshold region can be calculated from first principles(QCD). Experimentally, this new feature benefits us significantly in determinations of parameters that enter the threshold cross section:

$$\sigma(\sqrt{s}; m_t, \Gamma_t, \alpha_s(M_Z), M_H, \beta_H).$$

The identification of $t\bar{t}$ events is straightforward and we can easily get an overall detection efficiency in excess of 25 % with a signal to background ratio greater than 10. Fig. 2.44-a) is an example of a threshold scan, selecting $t\bar{t}$ events in the 6-jet final states, where we have assumed 11 points with 1 fb^{-1} each. The Monte Carlo data were generated with $\alpha_s(M_Z) = 0.12$ and $m_t = 150$ GeV without the contribution from Higgs exchange. When we fit these data points to the cross section formula, letting $\alpha_s(M_Z)$ and m_t move freely, we obtain the contours shown in Fig. 2.44-b). Even if $\alpha_s(M_Z)$ is totally unconstrained, we can determine m_t with a precision $\Delta m_t \simeq 0.2$ GeV.

3-Jet Invariant Mass

On the other hand, we can also determine m_t directly from the 3-jet invariant mass. Fig. 2.45[47] plots the invariant mass for a 3-jet system which consists of a jet pair corresponding to a W boson candidate and a b-jet candidate chosen from the remaining two jets. We can see a clear top quark peak over a broad background coming from wrong combinations. The width of the peak is dominated by detector resolutions. An integrated luminosity of 10 fb^{-1} at $\sqrt{s} = 500$ GeV enables us to achieve a statistical error $\Delta m_t \simeq 0.1$ GeV. When the measurement reaches this precision, we must take a proper account of various systematic errors. It should be noted that the theoretical ambiguities due to nonperturbative QCD effects might be minimal again because of the large top width acting as an infrared cutoff. Assuming that this is actually the case and that the systematic errors in calorimetry can be well controlled, we can input this m_t information to the threshold scan. This may allow us to make a reliable measurement of $\alpha_s(M_Z)$ which is largely free from theoretical ambiguities due to nonperturbative QCD, unlike those from jet shape variables.

The importance of this $\alpha_s(M_Z)$ measurement is enhanced in the SUSY scenario, since, there, the $\alpha_s(M_Z)$ is the key link between the weak scale and the GUT scale. In this case, the significance of the precision m_t measurements cannot be underestimated, since the top mass, which determines the top Yukawa coupling, is an indispensable input parameter for the calculations of masses and widths of Higgses and SUSY particles.

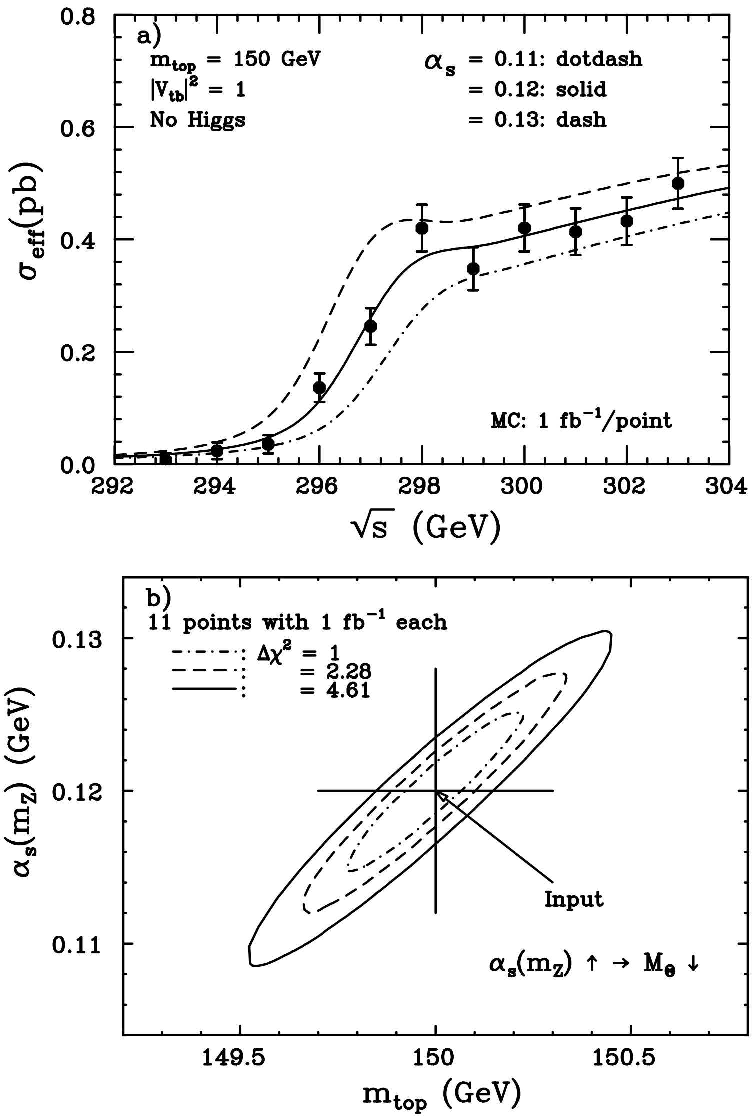

Figure 2.44: (a) An example of energy scan to determine m_t and $\alpha_s(M_Z)$ where each point corresponds to 1 fb^{-1}. (b) The contour resulting from the fit to the data points.

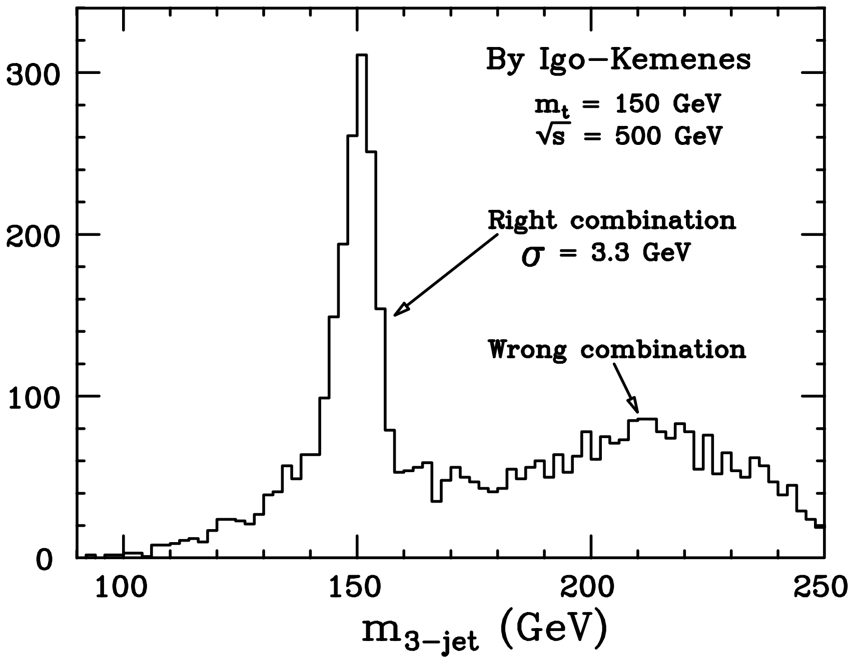

Figure 2.45: Invariant mass distribution for the 3-jet system resulting from $t \to bW$ decays.

2.6.2 Measurement of Top Width

The threshold scan also allows us to measure the top width. Fig. 2.46-a) compares the same Monte Carlo data as used for Fig. 2.44-a) with theoretical expectations for various onium widths. Fig. 2.46-b) shows the contours obtained from the fit to the Monte Carlo data, letting the top width and the top mass move freely. The expected statistical error is $\Delta|V_{tb}|^2 = 0.15 \sim 0.20$. We can improve this by optimizing the energy points and, of course, by increasing statistics. $|V_{tb}|^2 < 1$ suggests a fourth generation, while $|V_{tb}|^2 > 1$ signals some exotic decay mode such as $t \to bH^+$ or $t \to \tilde{t}\tilde{\chi}_1^0$.

2.6.3 Measurement of Top Yukawa Coupling

The heaviness of the top quark, on the other hand, allows us to directly measure the top Yukawa coupling. One way to do this is to examine closely the threshold shape. Notice that, if it were not for the large top width, the reliable estimation of the QCD contribution would become impossible and would make hopeless the extraction of the effect of Higgs exchange. Figs. 2.47-a) and -b) compare the same Monte Carlo data shown in Fig. 2.44-a) with theoretical expectations for various M_H and β_H(the normalized top Yukawa coupling). A 2-parameter fit to the data yields the contours shown in Fig. 2.47-c). The expected precision for a standard model Higgs of $M_H = 100$ GeV is about $\Delta\beta_H = 0.2$ for $m_t = 150$ GeV. We can also measure the Yukawa coupling using the process $e^+e^- \to t\bar{t}H$. The precision expected in this case is comparable to that from the threshold scan.

2.6.4 Angular Analyses

There is yet another new and remarkable property of a heavy top quark: the heavy top will decay before forming a top-hadron. This will, for the first time, enable us to measure the helicities

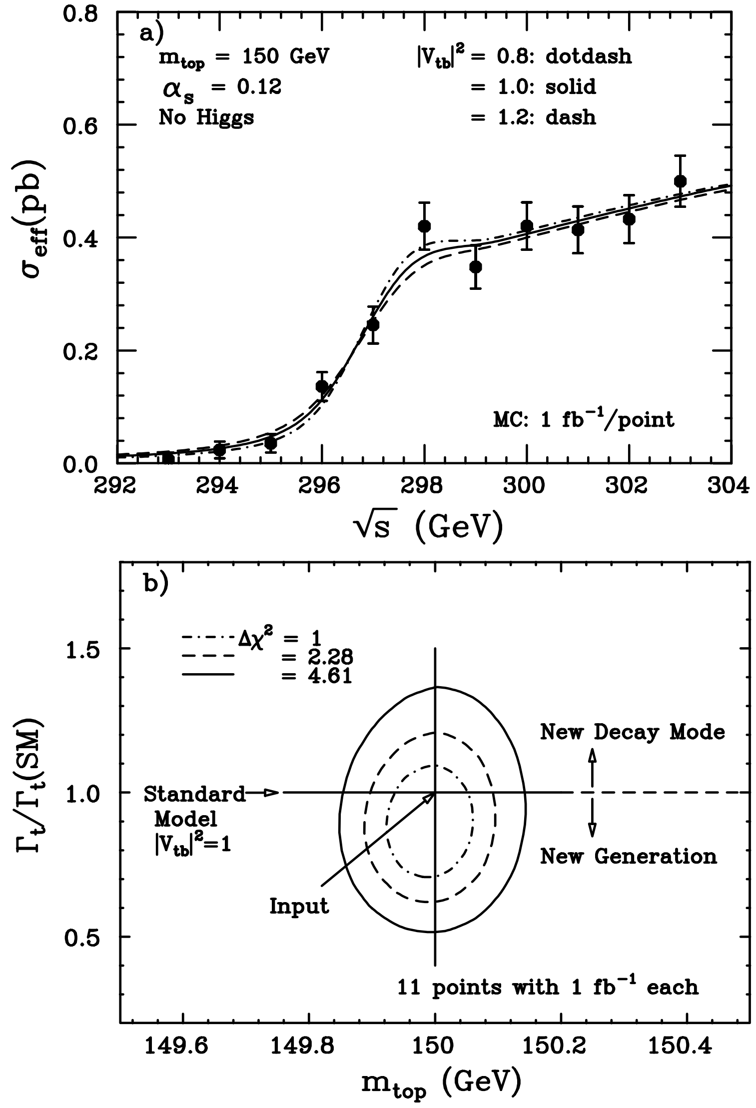

Figure 2.46: (a) An example of energy scan to determine m_t and $|V_{tb}|^2$ where each point corresponds to 1 fb^{-1}. (b) The contour resulting from the fit to the data points.

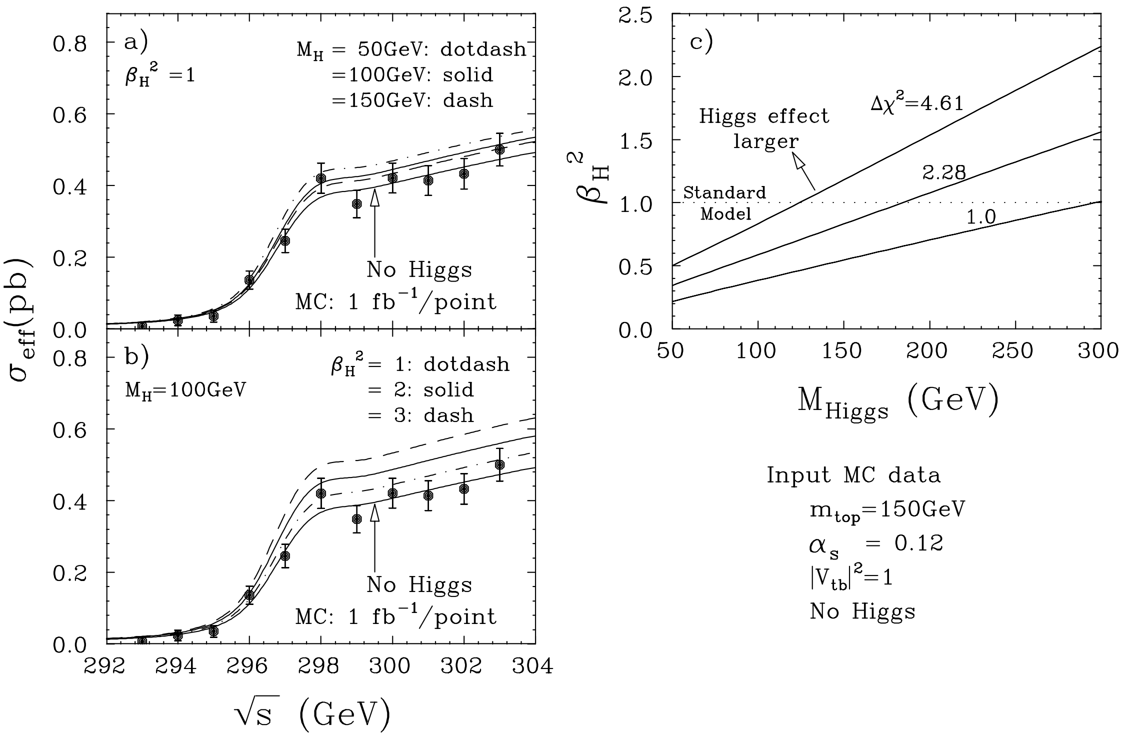

Figure 2.47: (a) An example of energy scan to determine M_H and β_H^2 where the effective cross section curves are superimposed for several M_H values. (b) The same plot with the effective cross section curves for several β_H^2 values. (c) The contour resulting from the fit to the data points.

of parent quarks via angular analyses of their decay daughters. The helicity measurement will provide us with a powerful tool to systematically investigate the top quark's production and decay vertices, in particular, when the vertices involve new particles expected in the SUSY scenario.

As a warmup exercise, let us first try to determine the polarization of W's from top decays. Heavy top quarks predominantly decay into longitudinal W bosons which are a good probe to investigate the symmetry breaking sector. Therefore, if the symmetry breaking sector is different from that of the standard model, the branching fraction

$$R = \frac{\Gamma(t \to bW_L)}{\Gamma(t \to bW_T) + \Gamma(t \to bW_L)}$$

might also differ from the standard model prediction. Fig. 2.48-a) is an example of the helicity angle distribution for jets from W decays. The Monte Carlo events, which were generated with the standard model coupling, agree well with the standard model prediction. A fit to the helicity angle distribution results in the 1-σ bounds shown in Fig. 2.48-b) as a function of m_t. Given a data sample of 1k top events, it is easy to determine the branching fraction R with a statistical error of less than 2 %.

To see the capability of the top helicity determination, we consider here an imaginary case, in which the tbW vertex is right-handed, and compare the resultant angular distribution with that of the left-handed(the standard model) case in Fig. 2.49[48]. The Monte Carlo data correspond to 10 fb^{-1} with an electron beam polarization of 80 %. The difference is clear.

2.7 Precision Electroweak Physics

So far, we have been assuming the existence of a light Higgs boson. In this section, we will turn our attention to the case in which no light Higgs bosons have been found. As we stressed earlier, the absence of light Higgs bosons itself will make a very strong impact on high energy physics, since it implies the death of low energy supersymmetry and GUT.

In the absence of the light Higgs boson, we have to learn as much as possible from what we have at hand, W, Z, and top. The important lesson at LEP is that precision measurements can provide valuable information to guide us in deciding our next step. This virtue of e^+e^- colliders will persist as we will see below.

2.7.1 Looking for New Physics in Loops

In the standard model, the Higgs mass, the W mass, and the top mass are interrelated through radiative corrections as shown in Fig. 2.50[49]. Therefore, we can estimate the Higgs mass by measuring the masses of W and top. For a precise determination of the W mass, we go down to the Z-pole and measure the polarization asymmetry for lepton pair productions, taking advantage of a highly polarized electron beam ($P_e > 90$ %) which is available only at linear colliders. The polarization asymmetry is directly related to $\sin^2\theta_W$ which, in turn, determines M_W. Given the design luminosity of JLC-I, the error on $\sin^2\theta_W$ will be dominated by the error on the beam polarization(see Fig. 2.51). If we can control this error down to the one percent level, the error on $\sin^2\theta_W$ will be about 0.1 %. Including theoretical ambiguities due to light quark loop corrections, we expect $\Delta M_W = 21$ MeV. The measurements of M_W and m_t determine the allowed range of the Higgs mass through the relation shown in Fig. 2.50. Plotted

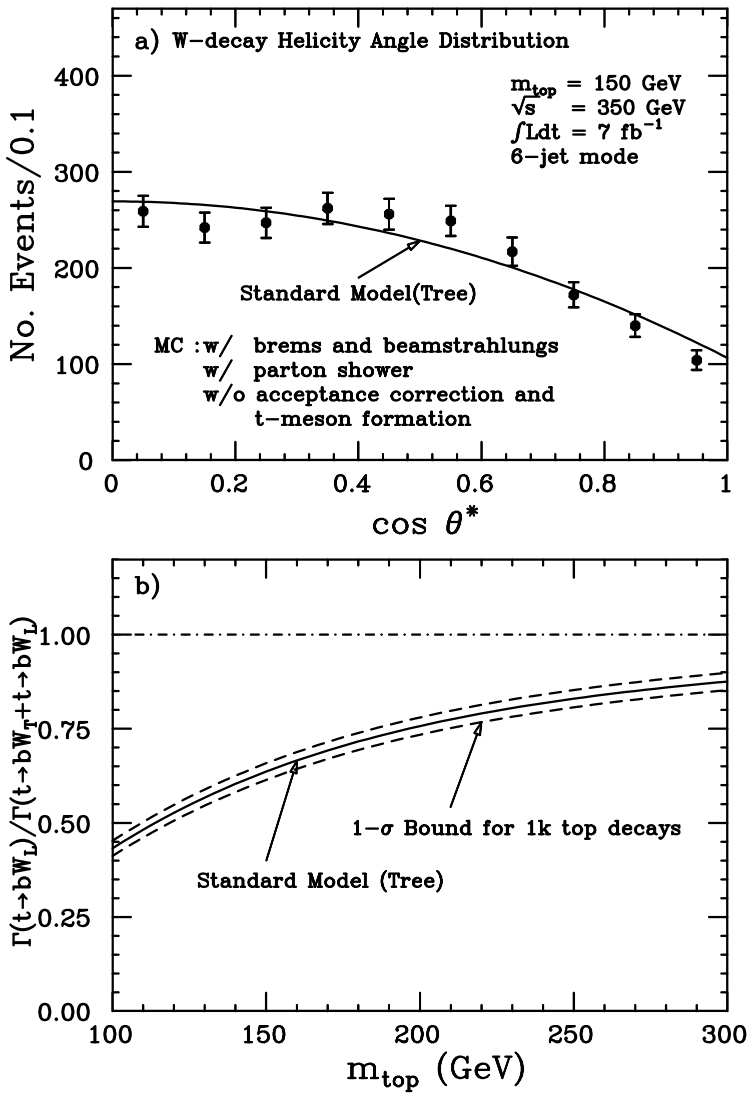

Figure 2.48: (a) Helicity angle of q or $\bar{q}$ from W decay. (b) Branching fraction of the $t \to bW_L$ decay as a function of m_t. The dashed curves indicate 1-σ boundaries expected for 1k top decays.

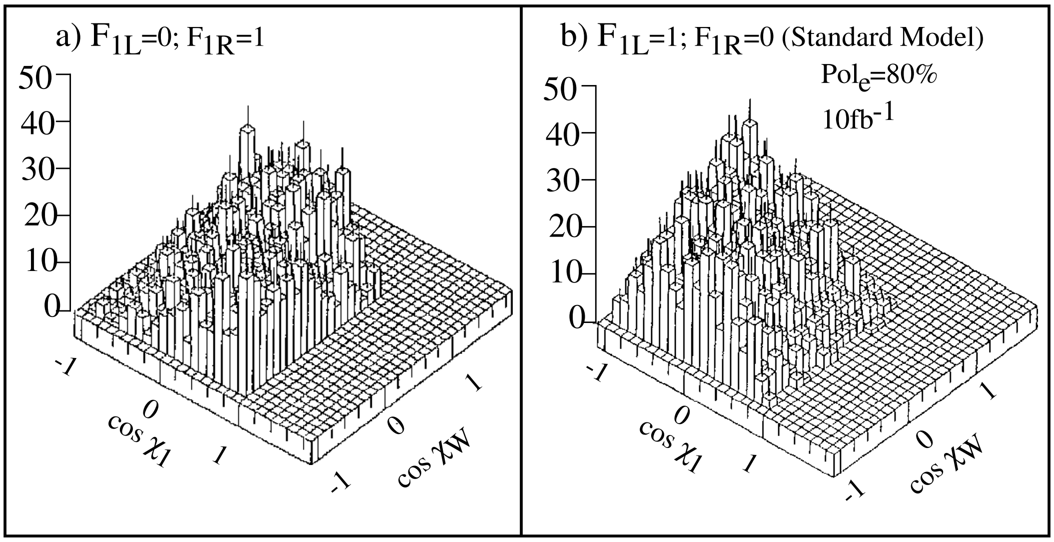

Figure 2.49: The top decay angle distributions for (a) $F_{1L} = 0$ and $F_{1R} = 1$ and (b) $F_{1L} = 1$ and $F_{1R} = 0$(Standard Model). χ_W is the helicity angle of W in the t rest frame and χ_l is the helicity angle of the lepton in the W rest frame.

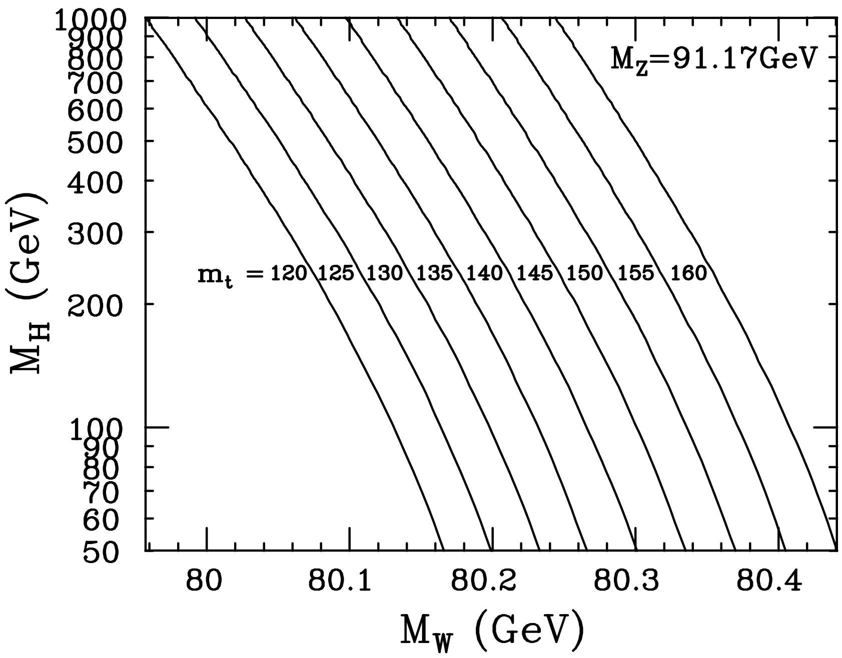

Figure 2.50: The mass of the standard model Higgs as a function of the W mass for various top masses.

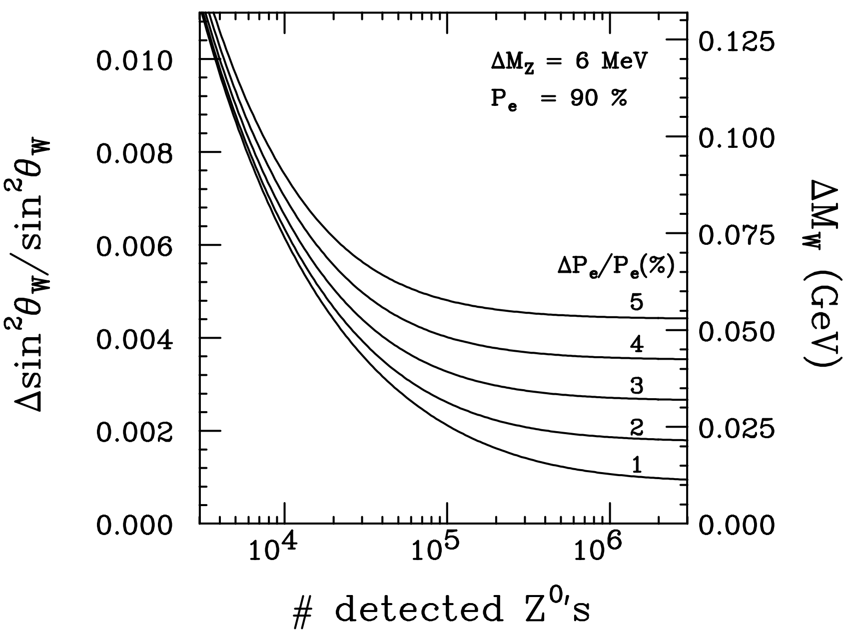

Figure 2.51: The expected error on $\sin^2\theta_W$ from the measurement of the electron beam polarization asymmetry as a function of the number of detected lepton pairs. Different curves correspond to different errors on the beam polarization.

in Fig. 2.52 are 1-σ contours in the m_t-M_H plane corresponding to different measurement errors on m_t: $\Delta m_t = 0.5$, 5.0, and 10.0 GeV, for $M_H = 500$ GeV and $m_t = 150$ GeV. This figure clearly demonstrates the importance of a precise determination of the top mass. As demonstrated in the last section, we can determine the top mass with a precision better than 0.5 GeV, which means the Higgs mass bound will be essentially controlled by the error on the W mass. Fig. 2.53 indicates the 1-σ bound for the Higgs mass as a function of the input Higgs mass. We can see that the JLC experiments will be able to significantly improve the present bound on the Higgs mass and will show us the next step to take.

The analysis presented above is based on the standard model framework. We can generalize the analysis with the help of the S and T parameters, which have been introduced by Peskin and Takeuchi[51] to parametrize loop contributions from new high-mass-scale physics. S and T represent, respectively, the effects of isospin-conserving and isospin-breaking loop contributions to weak boson self-energies. The power of the precision measurements at JLC-I can be best demonstrated in the S-T plane as shown in Fig. 2.54. The dotted line is the current limit[51] obtained from the precision electroweak data at LEP and other low energy data including those from deep-inelastic scattering and atomic parity violation experiments. The limit will be improved to the dot-dashed line, when the M_W measurement at LEP-II with $\Delta M_W = 100$ MeV becomes available. The three solid lines correspond to the JLC-I limits when $\Delta M_W = 21, 50,$ and 100 MeV, respectively. Notice that the JLC-I limits are estimated by assuming center values at $S = T = 0$ and a 0.1 % measurement of $\sin^2\theta_W$ and a 0.14 % measurement of R_Z which is the ratio of the hadronic and the leptonic widths of the Z boson. It should be emphasized that the JLC-I limits are *free* from hadronic and atomic uncertainties inherent in the present-day low energy data. When compared with the predictions of technicolor models indicated by arrows in the figure, one can see that the JLC-I limits severly constrain the possible scenarios.

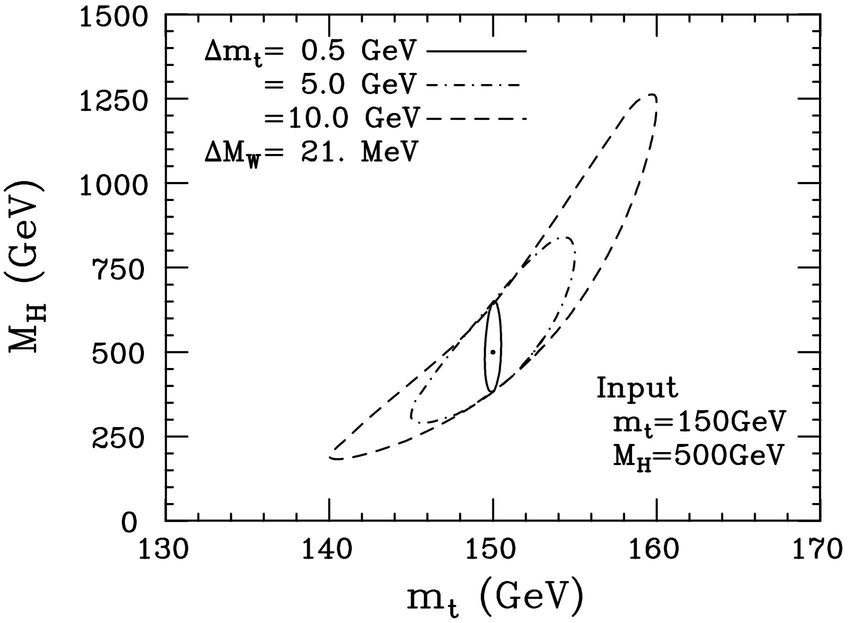

Figure 2.52: The 1-σ contours in the m_t-M_H plane showing how the Higgs mass bound improves with the error on m_t. The input values are $m_t = 150$ GeV and $M_H = 500$ GeV.

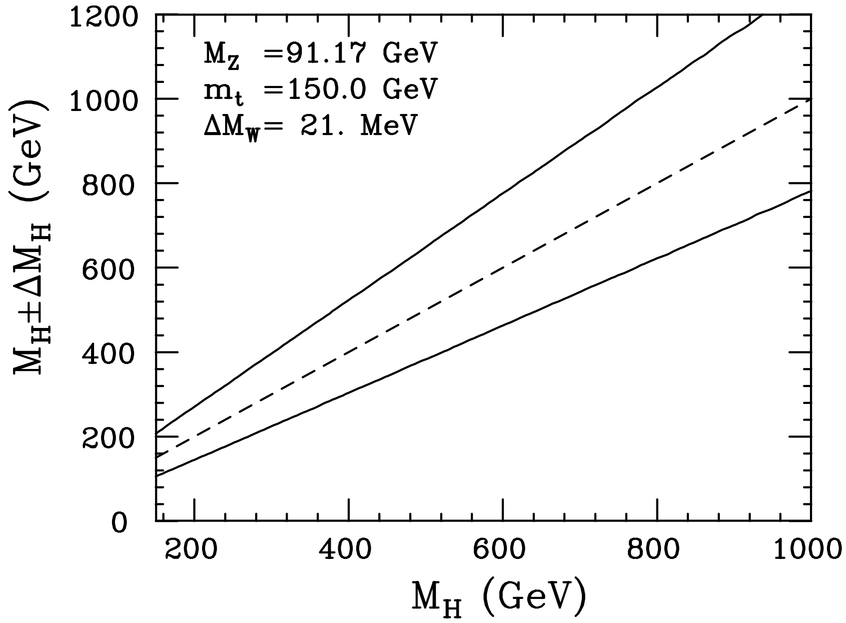

Figure 2.53: The 1-σ bounds on the Higgs mass as a function of the input Higgs mass.

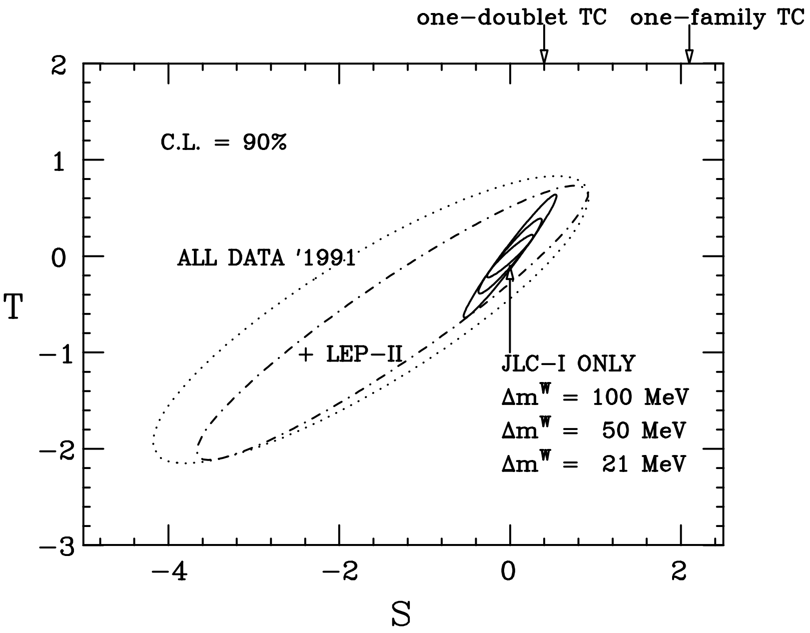

Figure 2.54: The 90 % confidence level limits on the S and T parameters. The dotted line is the present limit obtained from all the available data as of 1991[51]. The dot-dashed line is the expected limit after the precision M_W measurement at LEP-II: $\Delta M_W = 100$ MeV. The three solid lines are the limits expected for JLC-I data alone with $\Delta M_W = 21, 50$, and 100 MeV, respectively.

2.7.2 Self-couplings of W, Z, and γ

If the expected mass of the Higgs boson enters the heavy Higgs regime, the most likely scenarios will then become those based on a strongly interacting Higgs sector. In this case, one of the most important questions to address is whether only the longitudinal components of W and Z are composite or both of their transverse and longitudinal components are composite. In order to answer this question, we need to scrutinize the self-interactions of the vector bosons: W, Z, and γ. Though the possible forms of the self-interactions are rescricted, to some extent, by the data available at present[52, 53], the study of the direct productions of the weak bosons is inevitable to reveal the possible non-gauge nature of the weak bosons.

The total cross sections of the processes involving the weak bosons in the JLC energy region are shown in Fig. 2.55, together with the other standard model processes. In the JLC energy region, the weak boson production processes occupy the major part of the e^+e^- annihilation cross section. This is in contrast with the lower energy region such as of TRISTAN and LEP-I, where the dominant annihilation processes are fermion-pair productions. The processes, $e^+e^- \to W^+W^-$, $e^\pm\nu W^\mp$, and $\nu\bar{\nu}Z$ include the three-vector-boson coupling, while the processes such as $e^+e^- \to W^+W^-Z$ and $\nu\bar{\nu}W^+W^-$ include both the three- and the four-vector-boson couplings. Therefore the study of these processes allows us to test various aspects of the self-interactions among the vector bosons[54]. Such a study is discussed below, taking the anomalous three-vector-boson coupling as an example.

If there were anomalous pieces in three-vector-boson couplings, CP-conserving terms for

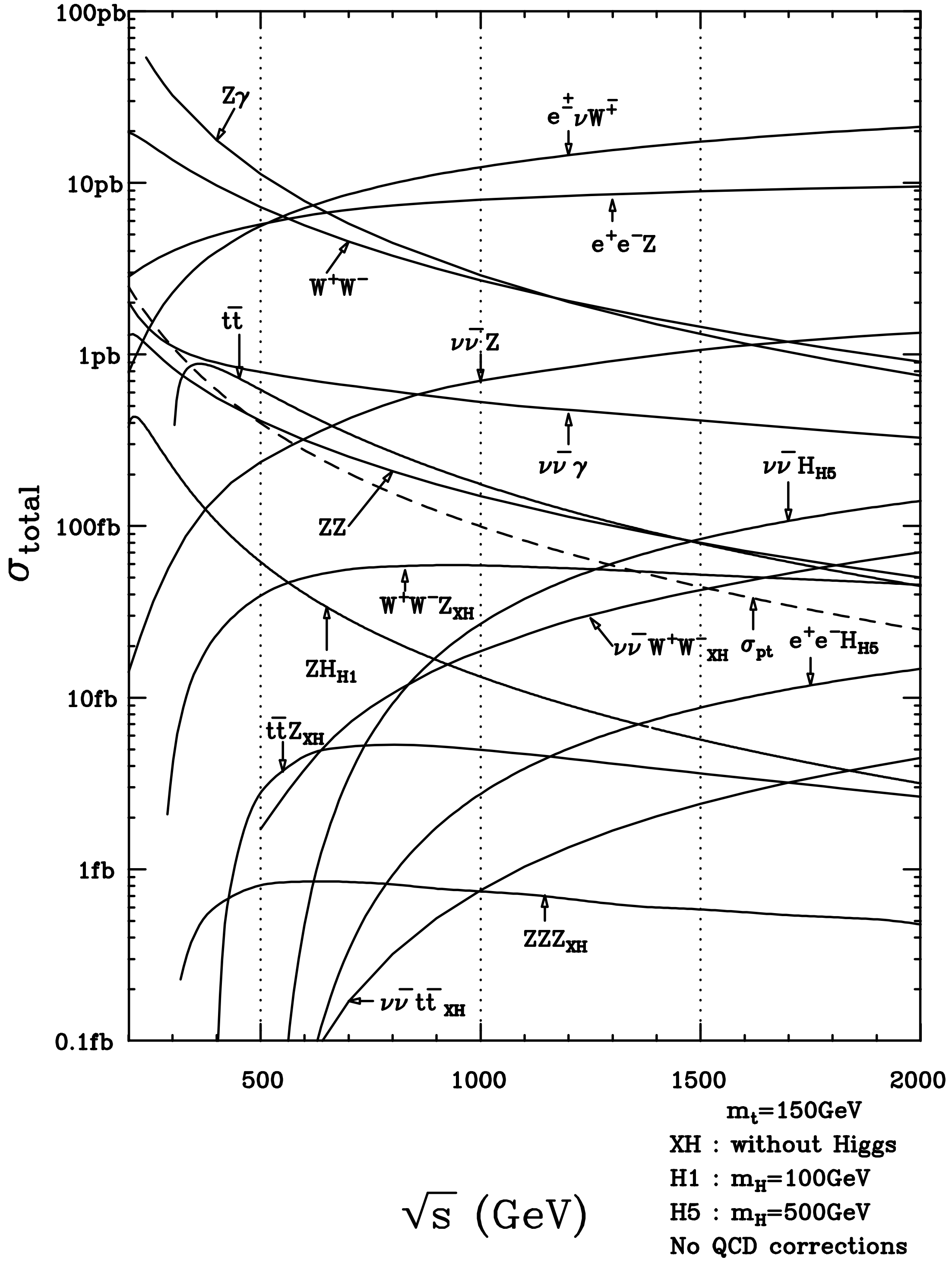

Figure 2.55: The total cross sections of the standard model processes in the JLC energy region. We require $E_\gamma > 0.1 \times E_{beam}$ and $|\cos\theta_\gamma| < 0.85$ for the $\nu\bar{\nu}\gamma$ process.

them can be parametrized as

$$\Delta L_{WWV} \sim \Delta\kappa_V W_\mu^\dagger W_\nu V^{\mu\nu} + \frac{\lambda_V}{M_W^2} W_{\rho\mu}^\dagger W_\nu^\mu V^{\nu\rho}$$

where

$$F^{\mu\nu} \equiv \partial^\mu F^\nu - \partial^\nu F^\mu \quad (F = W/V)$$

and V stands for either γ or Z. At JLC-I, we can study the $WW\gamma$ couplings, using the following three processes: $e^+e^- \to W^+W^-$, $e^\pm\nu W^\mp$, and $\nu\bar{\nu}\gamma$. The $e^\pm\nu W^\mp$ and $\nu\bar{\nu}\gamma$ processes are sensitive only to the $WW\gamma$ couplings; the $e^\pm\nu W^\mp$ process contains the WWZ couplings, however, its contribution to the total cross section is negligible. On the other hand, the W^+W^- process is sensitive to both the $WW\gamma$ and the WWZ couplings.

Fig. 2.56 compares the expected limits on the anomalous $WW\gamma$ couplings obtained from these processes for an integrated luminosity of 30 fb^{-1} and a beam polarization of 80 %, when the self-couplings are those of the standard model. As seen in the figure, the most sensitive is

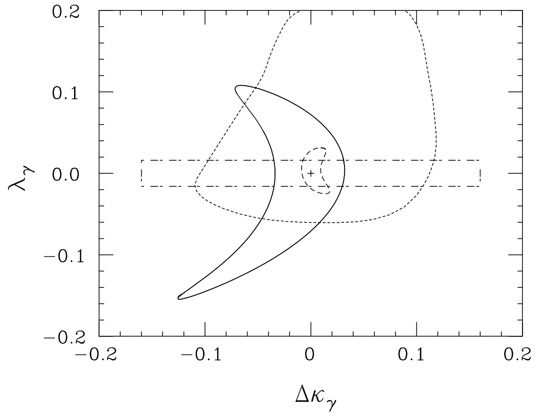

Figure 2.56: The expected 90% confidence level contours representing the sensitivities to the anomalous couplings in the plane of $\Delta\kappa_\gamma$ and λ_γ, when an integrated luminosity of 30 fb^{-1} is accumulated at $\sqrt{s} = 500$ GeV with a beam polarization of 80 %. The solid, dashed, and dotted curves are the limits obtained from the processes, $e^+e^- \to e^\pm\nu W^\mp$, W^+W^-, and $\nu\bar{\nu}\gamma$, respectively. The dot-dashed curve is that expected at SSC[55]. The vertical cross symbol indicates the input values corresponding to the standard model.

the process $e^+e^- \to W^+W^-$, because of the severe gauge cancellation among the diagrams.

Though this process contains both the $WW\gamma$ and the WWZ vertices, the measurements of the full differential cross section including the W-decay angular distributions, as well as the beam polarization dependence, help us disentangle possible anomalous self-couplings. Figs. 2.57-a) to -d) show the expected limits on various combinations of anomalous couplings for an integrated luminosity of 30 fb^{-1} at $\sqrt{s} = 500$ GeV[50], when we fit the differential cross section of the $e^+e^- \to W^+W^-$ process for the Monte Carlo data generated with the standard model couplings ($\Delta\kappa = \lambda = 0$). In the figures, the solid and the dashed lines are those obtained with and without the beam polarization asymmetry, respectively, and the dot-dashed lines are the limits expected from SSC. Notice that the polarized electron beam plays a crucial role here. It should also be emphasized that JLC experiments are indispensable to constrain $\Delta\kappa$, though SSC can set similarly stringent limits on the λ couplings.

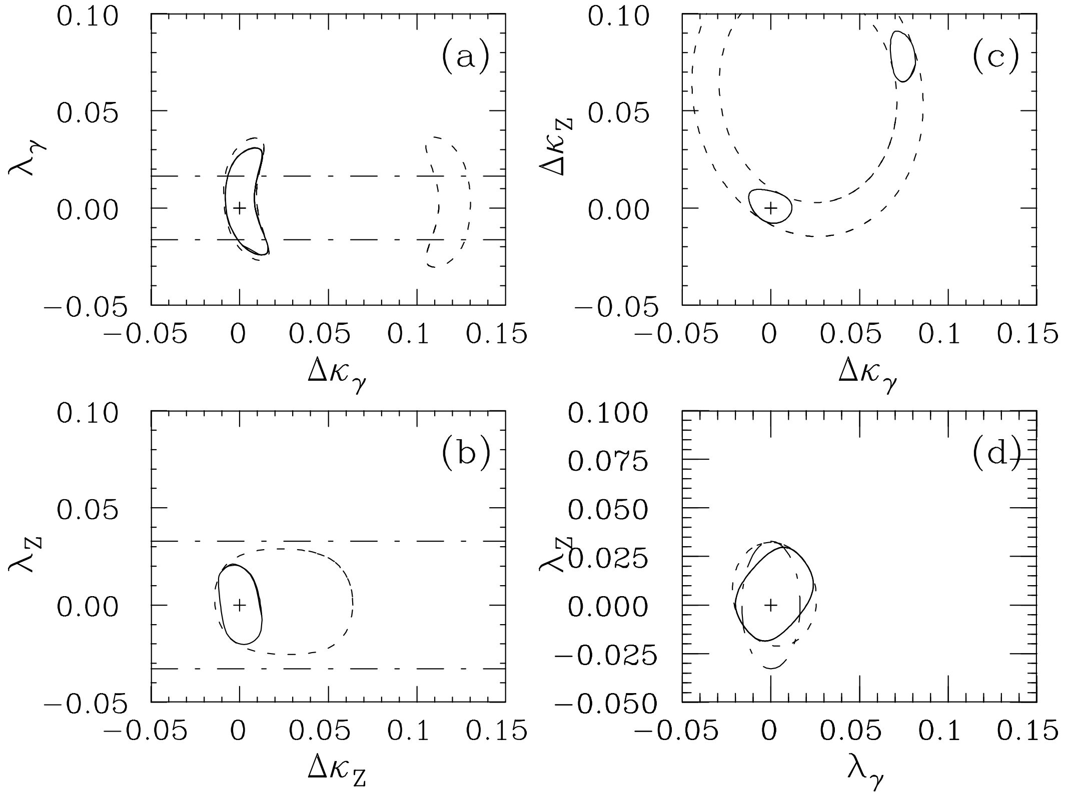

Figure 2.57: The expected 90 % confidence level limits on pairs of anomalous self-couplings for an integrated luminosity of 30 fb^{-1} at $\sqrt{s} = 500$ GeV. (a) $\Delta\kappa_\gamma$ and λ_γ. (b) $\Delta\kappa_Z$ and λ_Z. (c) $\Delta\kappa_\gamma$ and $\Delta\kappa_Z$. (d) λ_γ and λ_Z. The vertical cross symbols indicate the standard model positions used as inputs. Solid and dashed lines are with and without using 80 %-polarized electron beam. Dot-dashed lines correspond to expected SSC limits.

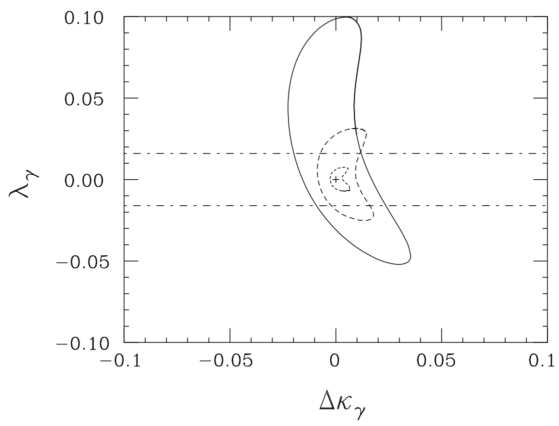

Figure 2.58: Same as Fig. 2.56-a) but at three different energies, $\sqrt{s} = 300$ GeV (solid), 500 GeV (dashed), and 1000 GeV (dotted). Also shown is that expected for SSC (dot-dashed).

The higher the energy, the severer the gauge cancellation becomes. Therefore, we expect that the sensitivity to the anomalous couplings is enhanced at higher energies. Fig. 2.58 shows, for three different energies, the expected sensitivity of the $e^+e^- \to W^+W^-$ process to the anomalous $WW\gamma$ couplings. The advantage of the higher energy is clear. Since this energy dependence and the higher luminosity more than compensate the cross section drop, the expected JLC limits exceed the precision obtainable at LEP-II by more than one order of magnitude and reach the expected size of loop-corrections. The existence of a light Higgs boson will not, therefore, diminish the importance of the precision measurement of this process, since, then, it will open up the possibility to get insights into physics at higher energy scales through radiative corrections.

2.8 CP Violation on the Z Pole

In the standard model, CP violation and flavor mixing have the same origin, the Yukawa sector governing the Yukawa interactions of fermions with the Higgs boson. When the Higgs field acquires a vacuum expectation value (the electroweak symmetry breaking), the Yukawa interactions give rise to the flavor-mixing represented by the Kobayashi-Masukawa matrix. Since this mixing matrix has a physical phase, meaning that at least one of its components is complex, CP violation naturally results. The underlying principle to determine the Yukawa couplings is, however, completely unknown. The relevant physics is presumably at very high energies, of the GUT scale or even of the Planck scale. Moreover, there are many ways to violate CP, for instance, a model with two Higgs doublets implies, in general, CP violation in its Higgs sector. The studies of CP violation and mixing are, therefore, not only essential to test the standard model, but also very important to probe the underlying physics at very high energies. In order to sort out many possible mechanisms for CP violation, however, we definitely need information on the physics beyond the standard model. We believe that, when SUSY particles are found and studied in detail at JLC-I, the range of the possibilities will be narrowed and the importance of the studies on CP violation and flavor mixing will be greately enhanced.

In this section, two topics of B-physics, CP-violation of B_d meson in $B_d \to \Psi K_s$ decay and B_s-$\bar{B}_s$ mixing, are discussed. There are four advantages to investigating B-physics on the Z-pole with JLC-I: (1) high luminosity, $L > 1.0 \times 10^{33}\ \mathrm{cm}^{-2}s^{-1}$, which is 50 times larger than that of LEP-I, (2) a highly polarized electron beam, which enables the tagging of b and $\bar{b}$ quarks in a geometrical way, (3) a large production cross section of B mesons, which is 5 times larger than that on $\Upsilon(4S)$, and (4) the narrow beam, which allows us to install a vertex detector very close to the interaction point to detect the B-decay vertices. The background due to beamstrahlung will be manageable on the Z-pole.

2.8.1 Compatibility with TeV Operation

The possibility to investigate B physics on the Z-pole with a linear collider was discussed at Snowmass '88[56] in comparison with other accelerators. It should be emphasized, however, that the design concept of the linear collider discussed there was quite different from that of JLC-I. At that time, there was a general belief that high repetition rate ($\geq$ kHz) would be necessary on the Z-pole to get high luminosity with a linear collider, so that it would be incompatible with a TeV linear collider design assuming a rather low repetition rate (about 200 Hz). A

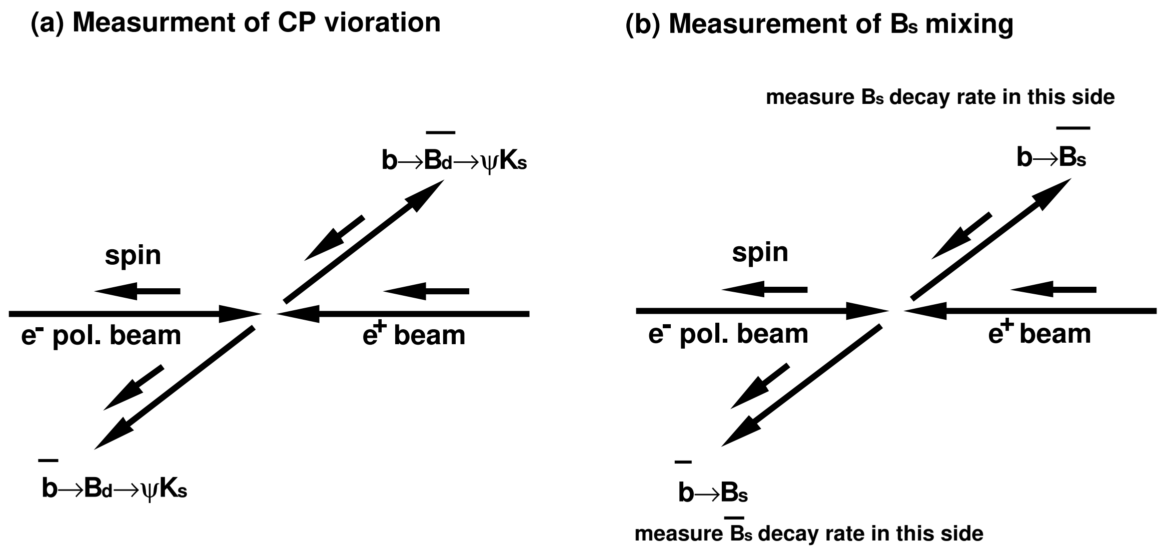

Figure 2.59: Schematical figures of relation between electron spin and b-quark spin in favoring condition. (a) is for CP violation measurement and (b) is for B_s mixing.

recent study at KEK[57], however, shows that a linear collider optimized for TeV operation can also serve a high-enough luminosity on the Z-pole, $L = 2.0 \times 10^{33}$ cm$^{-2}s^{-1}$, without crab-crossing, provided that its final focus system is properly modified. JLC-I is, therefore, capable of producing fruitful results not only in the TeV region but also on the Z-pole.

2.8.2 Forward-Backward Asymmetry

A large forward-backward asymmetry caused by the polarization of an electron beam plays an essential role (geometrical tagging) in the measurements of both CP violation and B_s-$\bar{B}_s$ mixing[58]. When the electron beam is polarized left handed, a b-quark ($\bar{B}$ meson) prefers to go in the forward direction (direction of the electron beam) as shown schematically in Figs.2.59-a) and -b). When we use a 95%-polarized beam[59] and detect the events in the polar angle region of $0.22 < |\cos\theta| < 0.94$, the forward-backward (F-B) asymmetry is 76% and the wrong-tag fraction is 12%. This wrong-tag fraction should be compared with 43.5% expected for an unpolarized beam for which the F-B asymmetry is 13%. CP violation can be measured by comparing the decay rates for $B_d(\bar{B}_d) \to \Psi K_s$, in the forward and the backward hemispheres. In order to enhance the sensitivity, we measure the decay rate as a function of the decay proper time,

$$\Gamma(B_d(\bar{B}_d) \to \Psi K_s) \propto e^{-\Gamma t}\{1 \pm \sin 2\phi_1 \sin X_d \Gamma t\},$$

where X_d is a mixing parameter (=0.7), Γ is the total decay width, and $\sin 2\phi_1$ is the CP violation parameter. The most probable value of $\sin 2\phi_1$ is estimated to be[60]

$$\sin 2\phi_1 = 0.37 \begin{array}{c} +0.54 \\ -0.21 \end{array} .$$

To observe the B_s-$\bar{B}_s$ mixing, we measure the decay rate of $B_s(\bar{B}_s)$ in the forward (backward) hemisphere. Then we fit the oscillation of the decay rate as a function of the decay proper time.

2.8.3 Measurement of $B_d(\bar{B}_d) \to \Psi K_s$

To study the detection sensitivity, we made an event-generator which includes the forward-backward asymmetry with a polarized electron beam. In our generator, B_d mesons decay into ΨK_s (the signal), or into $\Psi K_s \pi^0$ which is the most serious background. The Ψ's decay into leptonic channels with a 100% branching ratio (e^+e^- and $\mu^+\mu^-$), instead of the real branching ratio of 14%. The K_s mesons decay into $\pi^+\pi^-$ and $\pi^0\pi^0$ with branching ratios of 69% and 31%, respectively. Parameters used for the generation are $X_d = 0.7, \Gamma = 1/(13.1 \times 10^{-13}$ sec), and $|\cos\theta_b| < 0.94$.

The ΨK_s events are selected as follows. We first look for a pair of opposite sign tracks which has an invariant mass within ± 35 MeV around the Ψ mass and require that at least one track is identified as an electron or a muon: a track which has a momentum larger than 1.5 GeV and E/P larger than 0.5 is identified as an electron, while 95% of muons whose momentum are larger than 3.5 GeV are randomly selected as identified muons. For an unidentified track, no momentum cut is applied. K_s's are then reconstructed by looking for a pair of oppositely charged tracks, each of which has the closest distance to the z-axis larger than 0.04 cm and is identified neither as an electron nor as a muon. We require the pair to have an invariant mass consistent with that of K_s. Finally, if the pair of the K_s and the Ψ has an invariant mass within ± 50 MeV around the B_d mass, it is identified as B_d.

Fig.2.60 shows the invariant mass distributions of ΨK_s pairs for $B_d(\bar{B}_d) \to \Psi K_s$ (solid line) and $B_d(\bar{B}_d) \to \Psi K_s \pi^0$ (dotted line), respectively. One can see a clear peak of B_d in the solid histogram. On the other hand, the dotted histogram has a broad distribution of invariant masses ranging from 3.92 to 5.16 GeV, because of escaping π^0s. The detection efficiency for $B_d(\bar{B}_d) \to \Psi K_s$ is 37.1%, when we take the average in the $|\cos\theta|$ range between 0.22 and 0.94. Since the peak is clearly separated from the broad distribution, we neglect the background coming from $B_d(\bar{B}_d) \to \Psi K_s \pi^0$ which has an opposite CP to that of $B_d(\bar{B}_d) \to \Psi K_s$. To compromise the wrong-tag fraction and statistics, the $B_d(\bar{B}_d)$ mesons are required to be detected at $|\cos\theta|$ between 0.22 and 0.94.

We use a maximum likelihood method to get the CP violation parameter $\sin 2\phi_1$ from the distributions of decay proper time and $\cos\theta$. When the branching ratio for $B_d(\bar{B}_d) \to \Psi K_s$ is taken to be 0.03%, the expected $\sin 2\phi$ range of 0.16 to 0.91 requires an integrated luminosity of $(2.7 \sim 0.083) \times 10^{40}$ cm^{-2}, in order to confirm the CP violation in the B-meson decay at the level of three standard deviations. The required integrated luminosity corresponds to $1.4 \sim 0.043$ years (we assume 100 days operation per year) of JLC-I operation on the Z pole (Fig.2.61). If we assume the most probable value (0.37) of $\sin 2\phi_1$, quarter a year is enough to measure it. If we do not apply the maximum likelihood method and just use the integrated event ratio of $B_d(\bar{B}_d) \to \Psi K_s$ in the forward and backward regions, we need 2.6 times more statistics.

2.8.4 Measurement of B_s-$\bar{B}_s$ Mixing

We use $B_s \to l\nu D_s$ as the signal of B_s decay, where l is an electron or a muon to be identified as described above, while the D_s has to be detected through its decay into three charged hadrons and neutral particles, if any. There are altogether four charged tracks expected to have finite impact parameters. These four tracks are, therefore, required to be more than 2σ-away from the z-axis, where σ is the impact parameter resolution of the vertex detector. The three charged hadrons have to have an invariant mass less than 2 GeV to be consistent with the D_s decay. In

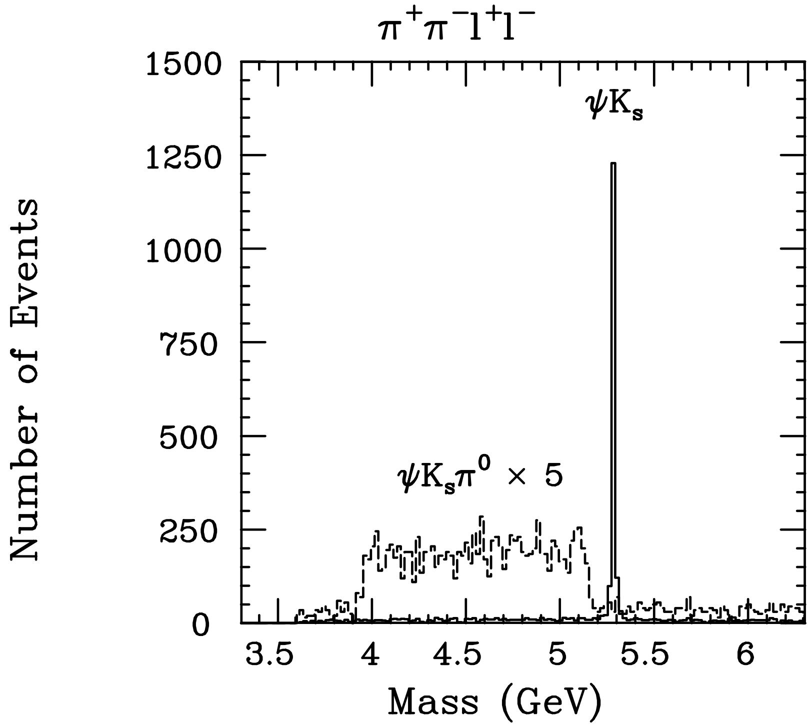

Figure 2.60: Invariant mass distributions of $\pi^+\pi^-l^+l^-$. The solid histogram shows ψK_s decay and the dotted one shows $\psi K_s\pi^0$ decay.

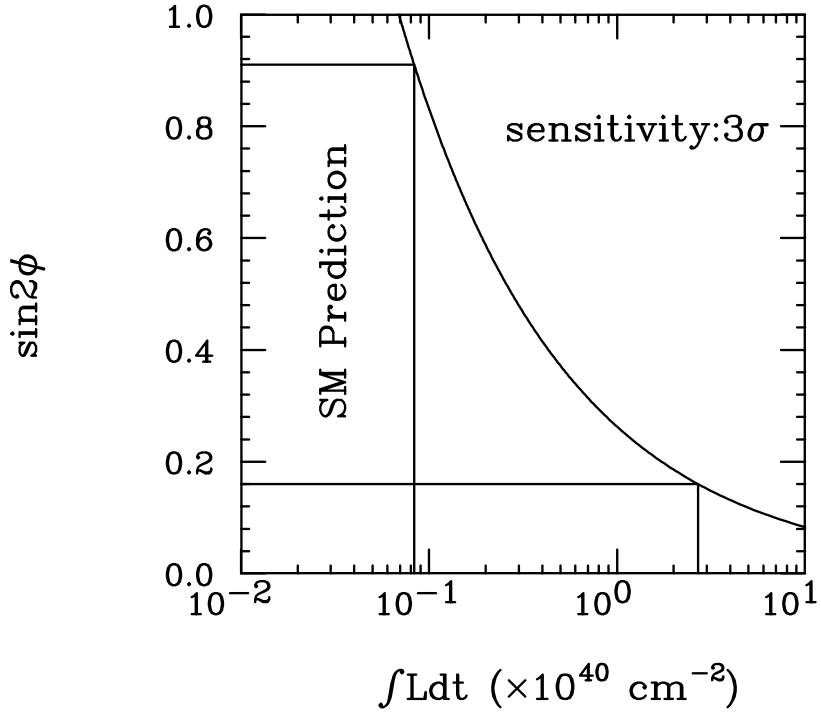

Figure 2.61: The required luminosity to measure $sin2\phi_1$ with three standard deviation.

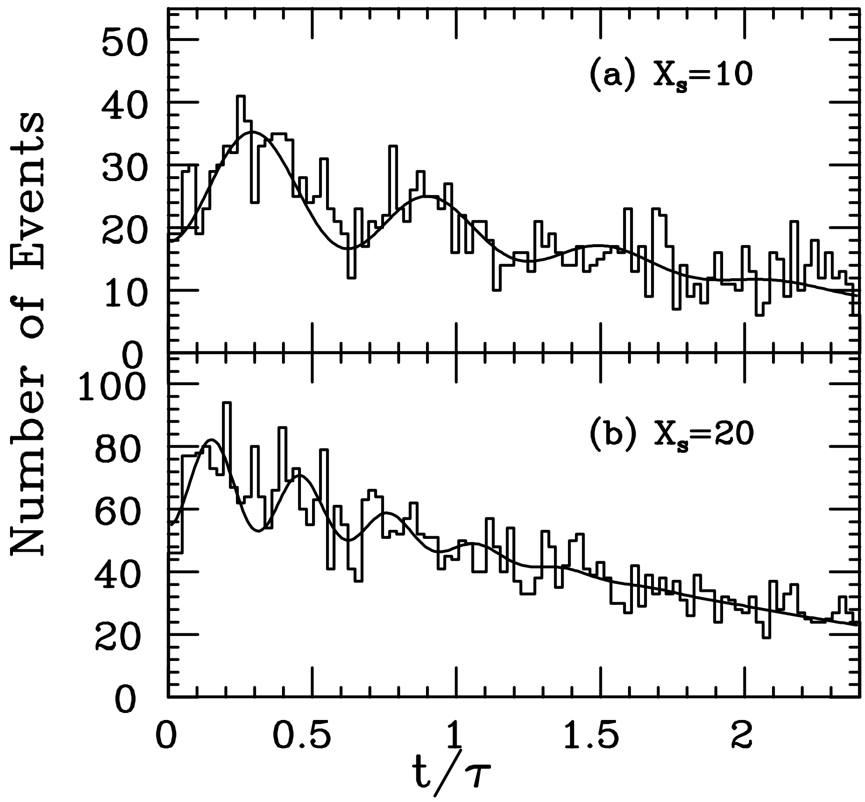

Figure 2.62: The decay proper time distribution for (a) $X_s = 10$ and (b) $X_s = 20$.

addition, we require that the decay point of D_s (the vertex formed by the three hadron tracks) is farther away from the interaction point, when compared with the decay point of B_s (the vertex formed by the lepton track and the combined momentum vector of the three hadron tracks). These cuts are very effective to eliminate the background from non-$b\bar{b}$ jets.

To calculate the decay proper time from the decay point, it is necessary to know the B_s momentum. Its event-by-event determination is, however, impossible because of the missing neutrino from the B_s decay and the unidentified neutral particles from the D_s decay. We, therefore, use the average momentum of B_s's estimated by the Monte Carlo simulation. This approximation is justified, as long as we use a tight sphericity cut. We thus require the event to have a sphericity smaller than 0.05. After this final cut, the efficiency for detecting $b\bar{b}$-jets is 4%, while that for $c\bar{c}$-jets (the most serious background) is only 0.2%. The backgound from light quarks is negligible. The resultant $b\bar{b}$-jet sample contains 20% of B_s mesons.

The vertex resolution for B_s decay is 90 μm mainly limited by the effect of missing neutral particles. Figs.2.62-a) and -b) show that the oscillation of the B_s decay can be clearly observed for both of $X_s = 10$ and 20, respectively. The amount of data used for the fitting in Figs.2.62-a) and -b) are 2.0×10^6 Z^0 and $4.0 \times 10^6 Z^0$, respectively, which correspond to less than half a day and one day of data acquisition with JLC-I on the Z-pole.

2.9 Heavy Higgs or Strongly Interacting W's

Even if JLC-I does not find any light Higgs bosons at center-of-mass energies up to 500 GeV, it can predict the Higgs mass through the precision electroweak measurements as described in

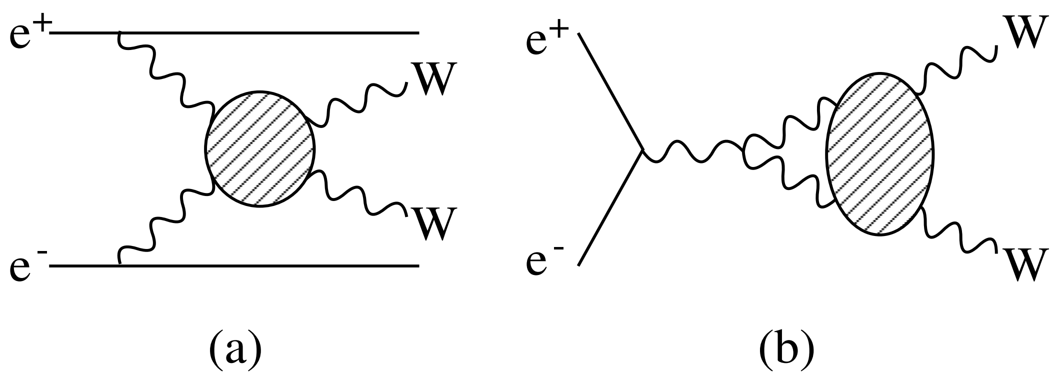

Figure 2.63: a) W-fusion process. b) Rescattering in W-pair creation.

the previous section. If this is the case, we have to upgrade the machine and increase the beam energy accordingly, to detect the Higgs boson. Such a heavy Higgs boson can be searched for in the W-fusion process shown in Fig.2.63-a).

If the predicted Higgs mass exceeds O(1 TeV), however, it does not necessarily mean the existence of an elementary Higgs boson of this mass. The Higgs mass should be regarded as the energy scale of a new strong interaction which is resposnsible for the mass-generation of the weak bosons. In this case, we need to understand the underlying dynamics governing the new strong interaction. The best probe to investigate it is the longitudinal components of the weak bosons, since they are closely related to the mass-generation[61]. At JLC, we can study the interaction of the longitudinal weak bosons via the WW-rescattering process shown in Fig.2.63-b).

In this section, we describe the heavy Higgs search via the W-fusion process and the search for a new strong interaction between W bosons via the WW-rescattering at JLC with $\sqrt{s} \gtrsim 1$ TeV.

2.9.1 W-fusion process

First we discuss the JLC's capability of heavy Higgs search at $\sqrt{s} = 1$ TeV and 1.5 TeV via the W-fusion process: $e^+e^- \to \nu_e\bar{\nu}_e W^+W^-$. The background to this process consists of

$$\begin{aligned} e^+e^- \quad & \to e^+e^-W^+W^-, \\ & \to \nu_e\bar{\nu}_e Z^0Z^0, \\ & \to e^-\bar{\nu}_e W^+Z^0,\ (e^+\nu_e W^-Z^0), \\ & \to e^+e^-Z^0Z^0, \\ & \to W^+W^-. \end{aligned}$$

The exact cross-section calculations of these processes are quite complicated, since there are many diagrams leading to the same final states. We have carried out the calculations, using the helicity amplitude technique with the help of GRACE/CHANEL[62].

It should be emphasized that, if the Higgs boson mass is greater than 800 GeV, the S-wave amplitude for the scattering of longitudinally polarized gauge bosons violates unitarity at the tree level[63]. To avoid this unitarity violation, we enlarged the width of the Higgs boson by a minimal amount in our cross section calculations.

Given these cross sections, we can study the feasibility of heavy Higgs search at JLC. The analysis proceeds as follows: we first select four-jet events from which W-pair events are selected

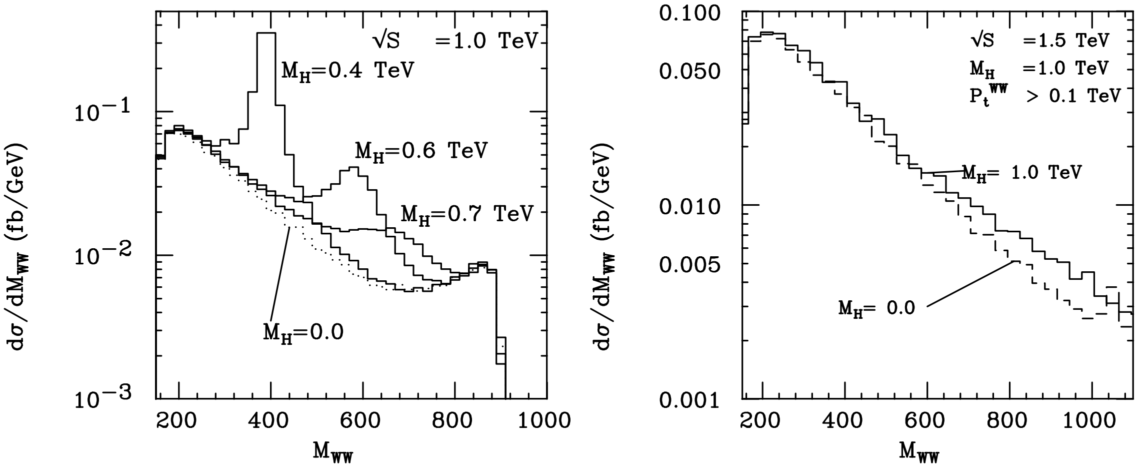

Figure 2.64: Differential cross sections as a function of WW invariant mass at (a) $\sqrt{s} = 1$ TeV and for Higgs masses of 0, 400 GeV, 600 GeV, and 700 GeV, and at (b) $\sqrt{s} = 1.5$ TeV and for Higgs masses of 0 and 1.0 TeV.

by reconstructing jet-jet invariant masses. We then look for a resonance or an excess of events in the invariant mass distribution of the so reconstructed W-pairs, by comparing the distribution with that expected for $m_{H_{SM}} = 0$ (the massless Higgs case). Figs.2.64-a) and -b) show the differential cross sections at $\sqrt{s} = 1.0$ and 1.5 TeV, respectively, as a function of the W-pair mass.

When the Higgs mass is greater than 700 GeV, the signal of the Higgs boson becomes less significant compared with the massless Higgs case. The largest background, before making any cuts, comes from $e^+e^-W^+W^-$ and $e^+e^-Z^0Z^0$ (two-photon processes). To reduce the background events from these two processes, we vetoed the events which had high energy electrons in the visible area. When the electrons go through the beam pipe, the W-pair cannot have a large transverse momentum with respect to the beam axis. If it is required that the transverse momentum of the W-pair should be greater than 70 GeV at $\sqrt{s} = 1$ TeV (100 GeV for 1.5 TeV), and that the events with an electron which has an energy greater than 50 GeV and a polar angle greater than 150 mrad are vetoed, about 95% of the two-photon events are rejected. The W-pair production process ($e^+e^- \to W^+W^-$) can also be a background source, when the electron or positron emits high energy photon(s) due to beamstrahlung or initial state radiation. This background is also reduced by the cut on missing transverse momentum. For further reduction of the W-pair background, we use the decay angle distribution of quarks in the W-boson rest frame. The details of the analysis are described elsewhere[64].

After all of these cuts, the WW invariant mass distributions shown in Figs.2.65-a) and -b) are expected for an integrated luminosity of 200 fb^{-1}. We can detect the excess due to the heavy Higgs boson signal over the background coming from the processes listed above, at the level of three standard-deviations.

2.9.2 Rescattering in $e^+e^- \to W^+W^-$

As demonstrated above, the Higgs search at JLC will never fail, if there is an elementary Higgs boson at all. Therefore, its non-observation at JLC will force us to consider that at least the longitudinal components of the weak bosons are some composite objects governed by a new strong interaction. If their transverse components are also composite, there must exist

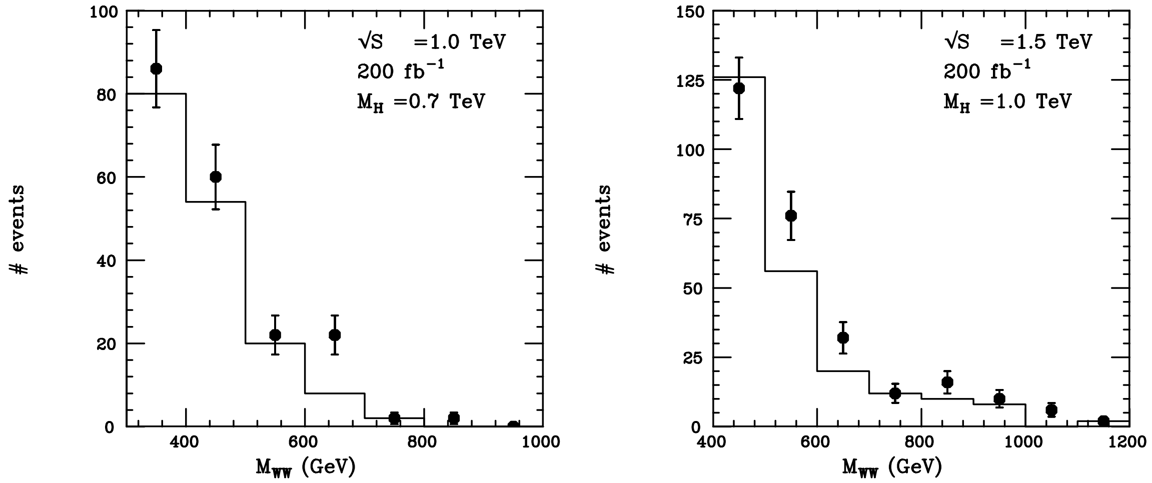

Figure 2.65: The expected distribution of W-pair invariant masses for an integrated luminosity of 200 fb^{-1} at $\sqrt{s}$=1.0 TeV (1.5 TeV). The data points were calculated with a Higgs mass of 0.7 TeV (1.0 TeV) and the histograms with the massless Higgs.

some anomalous self-coupling among the weak bosons, which can be observed as discussed in subsection 2.7.2. When no such anomalous coupling is observed and the transverse components are verified to be gauge-like, the remaining possibility is that the weak bosons are gauge bosons which acquire their masses from the spontaneous symmetry breaking induced by a new strong interaction. In this subsection, we consider such a case and discuss how to observe the new strong interaction through studies of the $e^+e^- \to W^+W^-$ process.

There are nine WW helicity combinations for the $e^+e^- \to W^+W^-$ process, of which only the following three survive at high energies ($s \gg m_W^2$): $W_+^+W_-^-$, $W_-^+W_+^-$, and $W_0^+W_0^-$, where suffixes indicate the W helicities. The new strong interaction among the longitudinal weak bosons induces a rescattering of the final-state $W_0^+W_0^-$. The rescattering gives rise to a P-wave phase shift $\delta_{11}(s)$, since the lowest order amplitude is predominantly in $J = 1$, and a possible form-factor effect $|F(s)|$, in the $W_0^+W_0^-$ amplitude:

$$\mathcal{T}(e^+e^- \to W_0^+W_0^-) \approx \mathcal{T}^{(lowest)}|F(s)|e^{i\delta_{11}(s)}.$$

The amplitudes for the other two helicity combinations, $W_\pm^+W_\mp^-$, remain the same and are almost real. Here, we assume, conservatively, no techni-ρ-like resonance ($|F(s)| = 1$) and the phase shift given by the low energy theorem: $\delta_{11} = 0.055(0.12)$ rad. at $\sqrt{s} = 1$ TeV (1.5 TeV). We can observe this phase shift through the interference of the $W_\pm^+W_\mp^-$ and $W_0^+W_0^-$ amplitudes, which is possible after the weak bosons decay into fermion pairs[61].

The phase shift appears as a change in the correlation of the azimuthal angles of the final-state fermions. Let $\phi(\bar{\phi})$ be the azimuthal angle of the final-state fermion from $W^+(W^-)$, with respect to the axis formed by the two W momenta, measured from the production plane (the plane spanned by the beam direction and the W momenta), then the variable sensitive to the strong WW final-state interaction is the sine of the sum of the two azimuthal angles, $\sin(\phi+\bar{\phi})$.

The sensitivity to the phase shift is maximum in the kinematical region where the magnitude of the $W_0^+W_0^-$ amplitude and those of the $W_\pm^+W_\mp^-$ amplitude are of the same order. Therefore, we require the production angle (Θ) of the W^- to satisfy $-1 < \cos\Theta < 0.5$, since the production amplitude for $W_\pm^+W_\mp^-$ peaks at $\cos\Theta = 1$ due to the t-channel neutrino exchange diagram. We also impose cuts on the decay polar angles (θ and $\bar{\theta}$) of the final-state fermions: $|\cos\theta| < 0.9$

and $|\cos\bar{\theta}| < 0.9$, since the decay amplitude of a longitudinal W boson behaves like $\sin\theta(\bar{\theta})$, while that of a transvers W boson like $1 \pm \cos\theta(\bar{\theta})$.

After all of these cuts, we obtain the angular distributions, with and without the rescattering at $\sqrt{s} = 1.5$ TeV, plotted in Fig.2.66-a). The effective cross section after the cuts is 52 fb. In the figure, the $\cos(2(\phi+\bar{\phi}))$ structure, corresponding to the four peaks, is due to the interference between the transverse W bosons, which has nothing to do with the rescattering. Our signal is the $\sin(\phi + \bar{\phi})$ structure, which results in an asymmetry in the peak heights.

In order to carry out this analysis, we need to measure all the angles defined above. This requires the full reconstruction of the final state. For this purpose, we select events in which one of the W bosons decays leptonically, and the other hadronically. We can then solve the kinematics, even if there is a beamstrahlung or bremsstrahlung photon. In addition, since we know the charge of the leptonic side, the charm tagging for $W^+(W^-) \to c\bar{s}(\bar{c}s)$ enables us to uniquely assign the charges to the final-state fermions.

The sensitivity to the phase shift δ_{11} of this measurement is shown in Fig.2.66-b). For example, for the low-energy-theorem phase shift at $\sqrt{s} = 1.5$ TeV, about 800 fully reconstructed WW events are necessary to confirm the strong rescattering at the 90% confidence level. This corresponds to an integrated luminosity of about 300 fb^{-1}, if the charm tagging efficiency is 100%. If a techni-ρ-like resonance exists in the $J = 1$ channel, the prospect of seeing the effect becomes brighter[65].

The complete understanding of the new strong interaction becomes possible only after extensive spectroscopic studies of the WW system and probably after weak-boson-jet studies to investigate the perturbative regime of the underlying dynamics. We believe that, if there is a new strong interaction among the weak bosons, its evidence obtained through the studies described above will place a solid foundation to promote construction of a new multi-TeV linear collider.

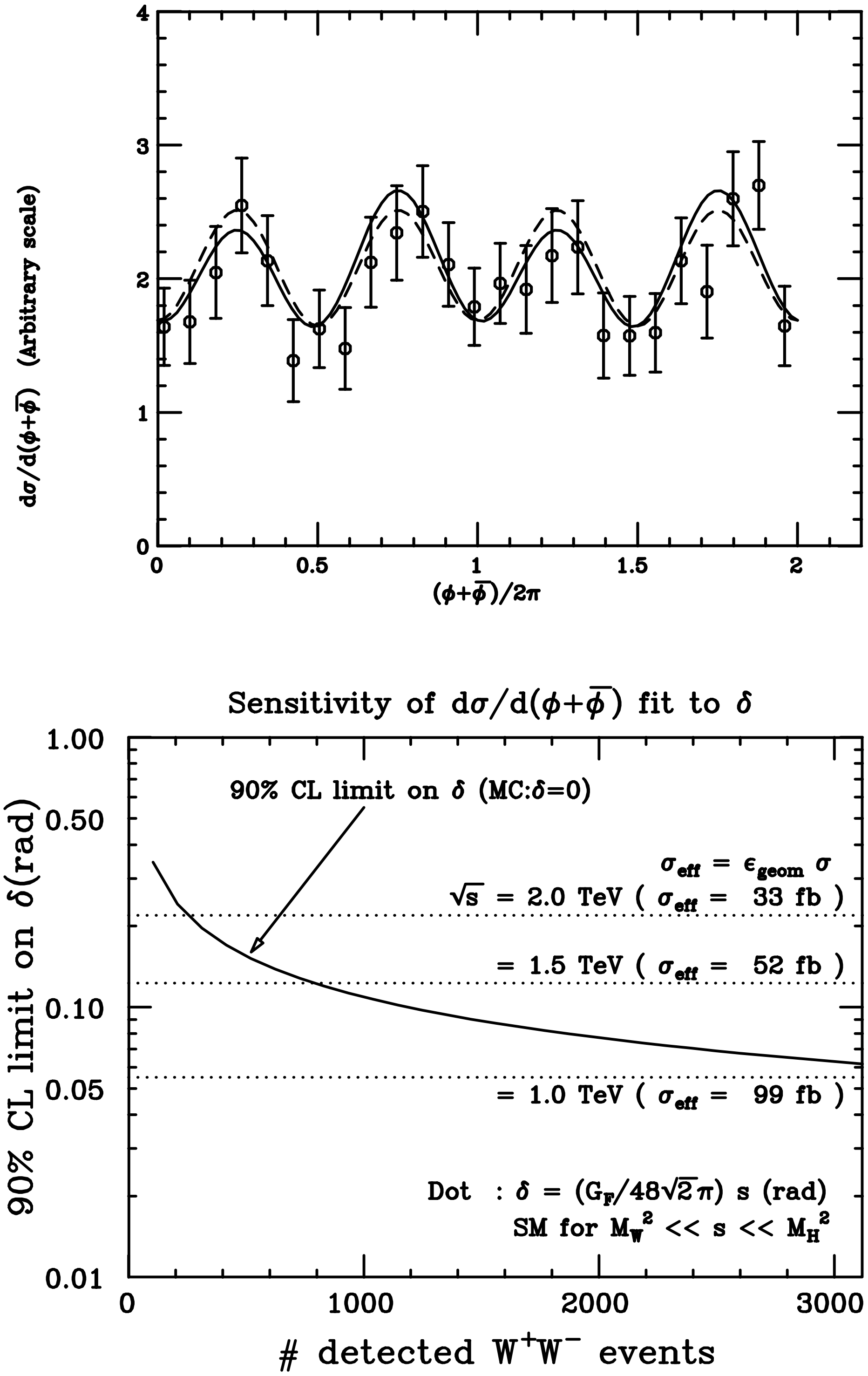

Figure 2.66: (a) The azimuthal angle correlation for $e^+e^- \to W^+W^-$ at $\sqrt{s}$=1.5 TeV. The solid line corresponds to a rescattering phase δ_{11}=0.1 and the dashed line to no rescattring. The data points are for 1000 fully reconstructed Monte Carlo events. (b) Sensitivity to the phase.

Bibliography

[1] S. Weinberg, *Phys. Rev. Lett.* **19** (1967) 1264;
A. Salam, Proc. 8th Nobel Sympos., Stockholm, ed. by N. Svartholm (Almqvist and Wiksell, Stockholm, 1968) p. 367.

[2] Y. Nambu and G. Jona-Lasinio, *Phys. Rev.* **122** (1961) 345;
P.W. Higgs, *Phys. Lett.* **12** (1964) 132, *Phys. Rev.* **145** (1966) 1156.

[3] UA1 Collaboration, *Phys. Lett.* **122B** (1983) 103, **126B** (1983) 398;
UA2 Collaboration, *Phys. Lett.* **122B** (1983) 476; **129B** (1983) 130.

[4] S.L. Glashow, *Nucl. Phys.* **22** (1961) 579.

[5] W.J. Marciano, BNL-45999 (April, 1991).

[6] M. Kobayashi and T. Maskawa, *Prog. Theor. Phys.* **49** (1973) 652.

[7] TOPAZ collaboration, *Phys. Lett.* **B255** (1991) 613, *KEK Preprint 92-49*; VENUS collaboration, *Phys. Lett.* **B278** (1992) 499, *Phys. Lett.* **B278** (1992) 393; AMY collaboration, *Phys. Lett.* **B218** (1989) 112, *Phys. Rev. Lett.* **64** (1990) 983.

[8] DELPHI collaboration, *Phys. Lett.* **B260** (1991) 240; L3 collaboration, *Z. Phys.* **C51** (1991) 179; OPAL collaboration, *Phys. Lett.* **B264** (1991) 269.

[9] P. Langacker, Pennsylvania preprint, UPR-0492T, (Jan 1992).

[10] TOPAZ collaboration, *Phys. Lett.* **B268** (1991) 457; ALEPH collaboration, *Phys. Lett.* **B263** (1991) 325; OPAL collaboration, *Phys. Lett.* **B263** (1991) 311.

[11] LEP Collaborations, *Phys. Lett.* **B276** (1992) 247.

[12] V.S. Fadin and V.A. Khoze, *JETP Lett.* **46** (1987) 525;
M.J. Strassler and M.E. Peskin, *Phys. Rev.* **D43** (1991) 1500;
Y. Sumino, K. Fujii, K. Hagiwara, H. Murayama and C.K. Ng, KEK preprint, KEK-TH-284, (Mar 1992);
H. Murayama and Y. Sumino, Tohoku University preprint, TU-401, (May 1992).

[13] L. Alvarez-Gaumé, J. Polchinski and M.B. Wise, *Nucl. Phys.* **B221** (1983) 495;
R. Barbieri and L. Maiani, *Nucl. Phys.* **B224** (1983) 32;
C.S. Lim, T. Inami and N. Sakai, *Phys. Rev.* **D29** (1984) 1488;
M. Drees and K. Hagiwara, *Phys. Rev.* **D42** (1990) 1709;
M. Drees, K. Hagiwara and A. Yamada, *Phys. Rev.* **D45** (1992) 1725.

[14] See E. Farhi and L. Susskind, *Phys. Rep.* **74** (1981) 277, and references therein.

[15] B. Holdom and J. Terning, *Phys. Lett.* **B247** (1990) 88;
M. Golden and L. Randall, *Nucl. Phys.* **B361** (1991) 3;
M. Peskin and T. Takeuchi, *Phys. Rev. Lett.* **65** (1990) 964;
W.J. Marciano and J.L. Rosner, *Phys. Rev. Lett.* **65** (1990) 2963;
G. Altarelli and R. Barbieri, *Phys. Lett.* **B253** (1991) 161.

[16] B. Holdom, *Phys. Lett.* **B150** (1985) 301;
T. Akiba and T. Yanagida, *Phys. Lett.* **B169** (1986) 432;
T. Appelquist, D. Karabali and L.C.R. Wijewardhana, *Phys. Rev. Lett.* **57** (1986) 957; *Phys. Rev.* **D35** (1987) 2605;
K. Yamawaki, M. Bando and K. Matsumoto, *Phys. Rev. Lett.* **56** (1986) 1335; *Phys. Lett.* **B178** (1986) 308.

[17] CDF Collaboration, *Phys. Rev.* **D45** (1992) 3921.

[18] D.V. Volkov and V.P. Akulov, *Phys. Lett.* **46B** (1973) 109;
J. Wess and B. Zumino, *Nucl. Phys.* **B70** (1974) 39.

[19] M. Veltman, *Acta Phys. Pol.* **B12** (1981) 437;
L. Maiani, *Proc. Summer School of Gil-sur-Yvette* (Paris, 1980) p. 3.

[20] H. Sugawara, talk presented at *the Symposium on the Electroweak Symmetry Breaking and Accelerator Projects*, in 47th Annual Meeting of the Physical Society of Japan, March, 1992.

[21] H. Georgi and S. Glashow, *Phys. Rev. Lett.* **32** (1974) 438.

[22] H. Georgi, H.R. Quinn and S. Weinberg, *Phys. Rev. Lett.* **33** (1974) 451.

[23] A.J. Buras, J. Ellis, M.K. Gaillard and D.V. Nanopoulos, *Nucl. Phys.* **B135** (1978) 66.

[24] S. Dimopoulos, S. Raby and F. Wilczek, *Phys. Rev.* **D24** (1981) 1681;
S. Dimopoulos and H. Georgi, *Nucl. Phys.* **B193** (1981) 150;
N. Sakai, *Z. Phys.* **C11** (1981) 153.

[25] Y. Okada, M. Yamaguchi and T. Yanagida, *Prog. Theor. Phys.* **85** (1991) 1, *Phys. Lett.* **B262** (1991) 54;
J. Ellis, G. Ridolfi and F. Zwirner, *Phys. Lett.* **B257** (1991) 83;
H.E. Haber and R. Hempfling, *Phys. Rev. Lett.* **66** (1991) 1815.

[26] T. Moroi and Y. Okada, Tohoku preprint, TU-405 (June 1992).

[27] K. Inoue, A. Kakuto, H. Komatsu and S. Takeshita, *Prog. Theor. Phys.* **68** (1982) 927;
L.E. Ibanez and G.G. Ross, *Phys. Lett.* **110B** (1982) 215;
K. Inoue, A. Kakuto and S. Takeshita, *Prog. Theor. Phys.* **71** (1984) 348;
L. Alvarez-Gaumé, J. Polchinski and M.B. Wise, *Nucl. Phys.* **B221** (1983) 495;
J. Ellis, J.S. Hagelin, D.V. Nanopoulos and K. Tamvakis, *Phys. Lett.* **125B** (1983) 275.

[28] K. Inoue, A. Kakuto, H. Komatsu and S. Takeshita, *Prog. Theor. Phys.* **67** (1982) 1889.

[29] N. Cabbibo, L. Maiani, G. Parisi and P. Petronzio, *Nucl. Phys.* **B158** (1979) 295.

[30] F. Abe et al., CDF collaboration, *Phys. Rev. Lett.* **64** (1990) 142.

[31] F. Merrit, talk presented at *ASPEN Winter Conference*, Aspen, 12th-19th January 1992.

[32] T. Kawamoto, talk presented at the JPS Meeting, 27th-30th March 1992.

[33] J. F. Gunion and Lynne. H. Orr, *UCD-91-15*, November, 1991.

[34] A. Yamada, *Mod. Phys. Lett.* **A7** (1992) 2877.

[35] A. Yamada, *Proceedings of the Third Workshop on Japan Linear Collider*, KEK, 1992, ed. by A. Miyamoto, *KEK Proceedings 92-13*, December, 1992.

[36] J. Alexander, *et al.*, *SLAC-PUB-4775*, January, 1989.

[37] K. Kawagoe, *Proceedings of the Third Workshop on Japan Linear Collider*, KEK, 1992, ed. by A. Miyamoto, *KEK Proceedings 92-13*, December, 1992.

[38] J. Kanzaki,*Proceedings of the Second Workshop on Japan Linear Collider*, KEK, 1990, ed. by S. Kawabata, *KEK Proceedings 91-10*, November, 1991.

[39] J. Kanzaki, talk presented at *the Workshop on Physics and Experiments with Linear Colliders*, Saariselkä, Finland, 1991; see also K. Fujii, *KEK Preprint 92-31*, May, 1992.

[40] S. Komamiya, *Phys. Rev.* **D38** (1988) 2158.

[41] P. Eerola and J. Sirkka, *CERN-PPE/92-76*, May, 1992.

[42] P. Janot, *LAL 91-61*, November, 1991.

[43] R. Barbieri and G. Giudice, *Nucl. Phys.* **B296** (1988) 75;
T. Kon and M. Jimbo, *Proceedings of the First Workshop on Japan Linear Collider*, KEK, 1989, ed. by S. Kawabata, *KEK Report* 90-2, April, 1990, p.280;
K. Inoue, M. Kawasaki, M. Yamaguchi, and T. Yanagida, *Phys. Rev.* **D45** (1992) 328.

[44] K. Hikasa, "JLC Supersymmetry Manual", in preparation.

[45] T. Tsukamoto, *KEK Preprint 92-34*, May, 1992.

[46] K. Fujii, *KEK Preprint 92-6*, April, 1992;
Y. Sumino, *UT 612*, May, 1992;
K. Fujii, *KEK Preprint 92-159.*

[47] P. Igo-Kemenes, private communication.

[48] M. Petradza, a talk presented at *Workshop on Physics and Experiments with Linear Colliders*, Saariselkä, Finland, Sep. 9-14, 1991.

[49] The calculations are based on the program provided by Z. Hioki.

[50] A. Miyamoto, talk presented at *the Workshop on Physics and Experiments with Linear Colliders*, Saariselkä, Finland, 1991.

[51] M. Peskin and T. Takeuchi, *Phys. Rev.* **D46** (1992) 381.

[52] K. Hagiwara, *KEK TH-320*, February, 1992

[53] A. De Rújula, M. B. Gavela, P. Hernandez and E. Massó, *CERN-TH-6272-91*, October, 1991.

[54] See for example; E. Yehudai, *SLAC-383*, August, 1991; S. Y. Choi and F. Schrempp, *DESY 91-155*, December, 1991; E. N. Argyres, *et al.*, *Phys. Lett.* **B259** (1991) 195.

[55] G. L. Kane, J. Vidal, and C.- P. Yuan, *Phys. Rev.* **D39** (1989) 2617.

[56] R.H.Siemann, *et al.*, *Proceedings of Summer Study:Snowmass '88, High Energy Physics in the 1990's*, Snowmass, Colorad, June 27-July 15, 1988.

[57] See section 4.1

[58] W.B.Atwood, *et al.*, *Phys. Lett.* **B216** (1989) 227;
T.Omori, *et al.*, *Proccedings of the Second Workshop on Japan Linear Collider*, KEK, Tsukuba, November 6-8, 1990;
Y.Kurihara, *et al.*, *Proccedings of Summer Study on High Energy Physics:SNOWMASS 1990*, Snowmass, July, 1990.

[59] Electron source of 95% polarization is not yet available.

However R/D efforts for high polarization show significant progress. We assume 95%-polarized source will be ready in near future.
Y.Kuriharam, *et al.*, *Nucl. Instr. and Meth.* **A313** (1992) 393;
H.Aoyagi, *et al.*, *Phys. Lett.* **A167** (1992) 415;
T.Maruyama, *et al.*, *PLAC-PUB-5731*, February, 1992.

[60] K.Abe, *et al.*, *KEK Report 90-23*, (1991)

[61] K. Hikasa, *KEK preprint 91-214*, *KEK-TH-319*, 1992.

[62] H. Tanaka, *Comp. Phys. Comm.* **58** (1990) 153;
H. Tanaka, T. Kaneko, Y. Shimizu, *Comp. Phys. Comm.* **64** (1991) 149.

[63] S. Willenbrok and G. Valencia, *Phys. Lett.* **B245** (1990) 341;
D. A. Dicus and W. W. Repko, *Phys. Rev.* **D42** (1990) 3660.

[64] Y. Kurihara, R. Najima, *KEK preprint 92-79*, August, 1992.

[65] T. Barklow, a talk presented at *Workshop on Physics and Experiments with Linear Colliders*, Saariselkä, Finland, Sep. 9-14, 1991.

[66] SDC Collaboration, "Technical Design Report", *SSCL-SR-1215*, April, 1992.

[67] J. Okada, M. Yamaguchi and T. Yanagida, *Phys. Lett.* bf B262 (1991) 54.